Published for SISSA by Springer

Received: *January 11, 2024*
Accepted: *April 15, 2024*
Published: *May 10, 2024*

Measurement of the total and differential cross-sections of $t\bar{t}W$ production in pp collisions at $\sqrt{s} = 13$ TeV with the ATLAS detector



The ATLAS collaboration

E-mail: atlas.publications@cern.ch

Abstract: Measurements of inclusive and differential production cross-sections of a top-quark-top-antiquark pair in association with a W boson ($t\bar{t}W$) are presented. They are performed by targeting final states with two same-sign or three isolated leptons (electrons or muons) and are based on $\sqrt{s} = 13$ TeV proton-proton collision data with an integrated luminosity of 140 fb^{-1}, recorded from 2015 to 2018 with the ATLAS detector at the Large Hadron Collider. The inclusive $t\bar{t}W$ production cross-section is measured to be 880 ± 80 fb, compared to a reference theoretical prediction of 745 ± 50 (scale) ± 13 (2-loop approx.) ± 19 (PDF, α_s) fb. Differential cross-section measurements characterise this process in detail for the first time. Several particle-level observables are compared with a variety of theoretical predictions, which generally agree well with the normalised differential cross-section results. Additionally, the relative charge asymmetry of $t\bar{t}W^+$ and $t\bar{t}W^-$ is measured inclusively to be $A_C^{rel} = 0.33 \pm 0.05$, in very good agreement with the theoretical prediction of 0.322 ± 0.003 (scale) ± 0.007 (PDF), as well as differentially.

Keywords: Hadron-Hadron Scattering, Top Physics

ArXiv ePrint: 2401.05299

Open Access, Copyright CERN,
for the benefit of the ATLAS Collaboration.
Article funded by SCOAP^3.

https://doi.org/10.1007/JHEP05(2024)131

Corrected publication 2025

Contents

1 Introduction **1**

2 ATLAS detector **4**

3 Data and simulated event samples **5**

4 Event reconstruction and object identification **8**

5 Analysis strategy **12**
5.1 Fiducial-volume definition 14

6 Background estimation **15**
6.1 Irreducible backgrounds 16
6.2 Reducible backgrounds 18

7 Systematic uncertainties **20**
7.1 Instrumental uncertainties 20
7.2 MC modelling uncertainties 21
7.3 Non-prompt-lepton background modelling uncertainties 22

8 Results **23**
8.1 Inclusive cross-section measurement 23
8.2 Differential cross-section measurement 32

9 Conclusion **46**

The ATLAS collaboration **56**

JHEP05(2024)131

1 Introduction

Two of the primary goals of the Large Hadron Collider (LHC) physics programme are to look for signs of new physics beyond the Standard Model (SM) and to determine the nature of electroweak (EWK) symmetry breaking. Despite thorough scrutiny, no significant deviation from the SM has been observed at the LHC. This strongly motivates further testing of the SM by measuring rare processes more precisely, examining final states where only a few SM processes contribute, and probing the Higgs boson in more detail. The study of associated production of a top-antitop quark pair and a W boson, $t\bar{t}W$, is strongly connected to each of these goals. With one of the heaviest SM final states accessible at the LHC, and a correspondingly small production cross-section, this process was first observed in Run 1 [1, 2] but a precise inclusive measurement and the first differential measurements became possible only with the full Run 2 dataset.

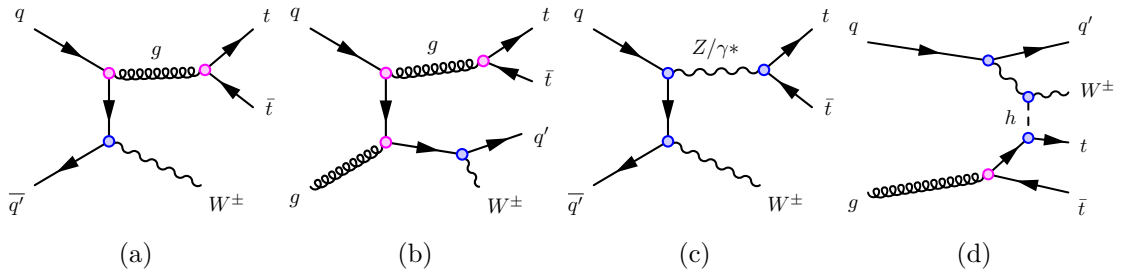


Figure 1. Illustrative Feynman diagrams for the dominant production modes of $t\bar{t}W$: (a) the LO contribution ($\alpha\alpha_s^2$), (b) a real emission diagram from the NLO QCD contribution ($\alpha\alpha_s^3$), (c) the tree-level EWK contribution (α^3), and (d) a representative diagram of the combined NLO QCD and EWK contributions ($\alpha^3\alpha_s$). The pink circles correspond to QCD couplings and the blue circles correspond to EWK couplings.

Beyond the inherent interest in measuring such a rare process more precisely, better understanding of $t\bar{t}W$ production is also important because it is a key background in many searches and other measurements at the LHC. It is one of the few SM processes that is an irreducible source of same-sign dilepton pairs. The rarity of these final states is exploited in many searches for new physics in extensions of the SM [3–5] where $t\bar{t}W$ is a major background. Moreover, $t\bar{t}W$ production is the dominant background in many measurements of other rare processes, such as $t\bar{t}H$ and $t\bar{t}t\bar{t}$ production, that are important when probing the top-quark Yukawa coupling and EWK symmetry breaking. The precision, accuracy and understanding of $t\bar{t}W$ modelling is one of the main limitations on the sensitivity of these measurements.

Further motivation for precise measurements of $t\bar{t}W$ production comes from tensions between the data and SM predictions observed in previous LHC measurements. Early measurements of $t\bar{t}W$ production by the ATLAS and CMS Collaborations at $\sqrt{s} = 8\,\text{TeV}$ [1, 2] were in agreement with the SM, but are less precise. More recent direct measurements of $t\bar{t}W$ production at $\sqrt{s} = 13\,\text{TeV}$ [6–9], and indirect measurements of $t\bar{t}W$ in analyses targeting $t\bar{t}H$ [10] and $t\bar{t}t\bar{t}$ [11, 12] production, have consistently observed $t\bar{t}W$ yields larger than the SM predictions.

Although $t\bar{t}W$ production superficially appears to be a simple process, and one governed by well-known SM couplings, the quark-antiquark initial state at leading order (LO) in the strong coupling constant leads to a rich array of phenomena. In particular, the process features charge-asymmetric production (of $t\bar{t}W^+$ and $t\bar{t}W^-$) from the parton distribution functions and unusually complex higher-order quantum chromodynamics (QCD) and EWK corrections. One consequence of the complex EWK corrections is the additional production mechanisms that they enable, such as tW-scattering [13]. This arises through EWK $t\bar{t}W$+jet production, which has embedded within it an effective $tW \to tW$ vertex that is interesting to understand in the SM but can also be probed for sensitivity to physics beyond the SM, for example in the context of effective field theory operators [14]. Figure 1 shows the dominant production modes for the $t\bar{t}W$ process, including additional QCD and EWK corrections. Therefore, measurements of $t\bar{t}W$ production are key in validating and improving the challenging theoretical predictions of this process, which has attracted much recent interest from the theoretical community, as described in section 3.

JHEP05(2024)131

NNLO [15]		FxFx [27]	
Order	σ [fb]	Order	σ [fb]
LO QCD: $\alpha_s^2\alpha$	$420\ ^{+106}_{-79}$		
NLO QCD: $+\alpha_s^3\alpha$	$622\ ^{+79}_{-72}$	$t\bar{t}W$+0,1,2j@NLO	$691\ ^{+66}_{-74}$
NNLO QCD: $+\alpha_s^4\alpha$	$711\ ^{+35}_{-46} \pm 14$		
NLO EWK: $+\alpha_s\alpha^3 + \alpha_s^2\alpha^2 + \alpha^4$	$745 \pm 50 \pm 13$	$+\alpha_s\alpha^3$	$739\ ^{+75}_{-81}$
		$+\alpha_s^2\alpha^2 + \alpha^4$	$722\ ^{+70}_{-78}$

Table 1. Summary of theoretical predictions with NNLO precision in the strong coupling [15] and using FxFx NLO multijet merging [27], both including NLO EWK corrections. The first uncertainty is due to variations of the chosen renormalisation and factorisation scales. Where there is a second contribution to the uncertainty, this corresponds to the approximation used in the 2-loop calculation. Uncertainties due to the choice of PDF and α_s are omitted.

A theoretical prediction at next-to-next-to-leading order (NNLO) in QCD, including next-to-leading order (NLO) EWK corrections, from ref. [15] of $\sigma(t\bar{t}W) = 745 \pm 50$ (scale) $\pm$ 13 (2-loop approx.) $\pm$ 19 (PDF, α_s) fb, is used as a reference cross-section. It supersedes previous calculations, refs. [16–28].

The different contributions to the total $t\bar{t}W$ cross-section are shown in table 1. Considering only QCD corrections, the predicted cross-section is $\sigma(t\bar{t}W)^{\text{QCD}} = 711\ ^{+35}_{-46}$ (scale) $\pm$ 14 (2-loop approx.) fb, while NLO EWK corrections give a total positive contribution of 4.9% [15]. Virtual EWK corrections are negative and 2.4% of the $\sigma(t\bar{t}W)^{\text{QCD}}$ value, and the remaining EWK contribution (including tW-scattering, as shown in figure 1(d)) gives a 6.9% positive correction to the $\sigma(t\bar{t}W)^{\text{QCD}}$ calculation [27]. The NLO multileg-merged FxFx prediction from ref. [27] captures a significant fraction of the NNLO QCD contributions to the cross-section.

This paper presents measurements of inclusive and differential cross-sections of $t\bar{t}W$ production at $\sqrt{s} = 13$ TeV, including measurements of the $t\bar{t}W$ relative charge asymmetry. This is the first measurement of differential cross-sections of $t\bar{t}W$ production at the LHC. The measurements are performed by analysing final states with two same-sign electric-charge leptons (2ℓSS) and three leptons (3ℓ), where ℓ denotes electrons or muons. The rest of the paper is structured as follows. Section 2 describes the ATLAS detector, section 3 provides an overview of the data and simulated samples used in the measurements, section 4 details the object reconstruction and selection and section 5 defines the analysis strategy. Section 6 provides a description of the strategy used to estimate non-prompt-lepton backgrounds. An overview of the systematic uncertainties is given in section 7. The results are presented in section 8 and conclusions are given in section 9.

JHEP05(2024)131

2 ATLAS detector

The ATLAS detector [29] at the LHC covers nearly the entire solid angle around the collision point.[1] It consists of an inner tracking detector surrounded by a thin superconducting solenoid, electromagnetic and hadron calorimeters, and a muon spectrometer incorporating three large superconducting air-core toroidal magnets.

The inner-detector system (ID) is immersed in a 2 T axial magnetic field and provides charged-particle tracking in the range $|\eta| < 2.5$. The high-granularity silicon pixel detector covers the vertex region and typically provides four measurements per track, the first hit normally being in the insertable B-layer installed before Run 2 [30, 31]. It is followed by the silicon microstrip tracker, which usually provides eight measurements per track. These silicon detectors are complemented by the transition radiation tracker (TRT), which enables radially extended track reconstruction up to $|\eta| = 2.0$. The TRT also provides electron identification information based on the fraction of hits (typically 30 in total) above a higher energy-deposit threshold corresponding to transition radiation.

The calorimeter system covers the pseudorapidity range $|\eta| < 4.9$. Within the region $|\eta| < 3.2$, electromagnetic calorimetry is provided by barrel and endcap high-granularity lead/liquid-argon (LAr) calorimeters, with an additional thin LAr presampler covering $|\eta| < 1.8$ to correct for energy loss in material upstream of the calorimeters. Hadron calorimetry is provided by the steel/scintillator-tile calorimeter, segmented into three barrel structures within $|\eta| < 1.7$, and two copper/LAr hadron endcap calorimeters. The solid angle coverage is completed with forward copper/LAr and tungsten/LAr calorimeter modules optimised for electromagnetic and hadronic energy measurements respectively.

The muon spectrometer (MS) comprises separate trigger and high-precision tracking chambers measuring the deflection of muons in a magnetic field generated by the superconducting air-core toroidal magnets. The field integral of the toroids ranges between 2.0 and 6.0 T m across most of the detector. Three layers of precision chambers, each consisting of layers of monitored drift tubes, cover the region $|\eta| < 2.7$, complemented by cathode-strip chambers in the forward region, where the background is highest. The muon trigger system covers the range $|\eta| < 2.4$ with resistive-plate chambers in the barrel, and thin-gap chambers in the endcap regions.

Interesting events are selected by the first-level trigger system implemented in custom hardware, followed by selections made by algorithms implemented in software in the high-level trigger [32]. The first-level trigger accepts events from the 40 MHz bunch crossings at a rate below 100 kHz, which the high-level trigger reduces in order to record events to disk at about 1 kHz.

An extensive software suite [33] is used in data simulation, in the reconstruction and analysis of real and simulated data, in detector operations, and in the trigger and data acquisition systems of the experiment.

[1] ATLAS uses a right-handed coordinate system with its origin at the nominal interaction point (IP) in the centre of the detector and the z-axis along the beam pipe. The x-axis points from the IP to the centre of the LHC ring, and the y-axis points upwards. Cylindrical coordinates (r, ϕ) are used in the transverse plane, ϕ being the azimuthal angle around the z-axis. The pseudorapidity is defined in terms of the polar angle θ as $\eta = -\ln\tan(\theta/2)$. Angular distance is measured in units of $\Delta R \equiv \sqrt{(\Delta\eta)^2 + (\Delta\phi)^2}$.

JHEP05(2024)131

3 Data and simulated event samples

This analysis uses proton-proton (pp) collision data recorded with the ATLAS detector from 2015 to 2018 at a centre-of-mass energy of $\sqrt{s} = 13\,\text{TeV}$. The LHC conditions required to achieve high instantaneous luminosity lead to additional collisions in the same and neighbouring proton bunch crossings (in-time and out-of-time pile-up). During the data-taking period considered, the number of collisions per bunch crossing ranged from about 8 to 70, with an average of 34. After the application of data-quality requirements [34], the data sample corresponds to an integrated luminosity of 140 fb^{-1}.

Theoretical predictions of the $t\bar{t}W$ process with higher-order corrections in the QCD and EWK couplings (α_s and α) are very challenging. At LO in α_s there are complications because $t\bar{t}W$ is a $q\bar{q}$-initiated process. The radiation of the W boson from one of the initial-state quarks polarises the incoming quark in the associated $t\bar{t}$ production, so it is important to correctly account for spin correlations [35]. Initial calculations of $t\bar{t}W$ production at NLO in QCD at fixed order [36] and later matched to a parton shower [37, 38] were also augmented with NLO EWK corrections (of order $\alpha^2\alpha_s^2$) [39] to provide the higher-order cross-sections used across the LHC programme for a number of years [16]. Full NLO calculations including fixed-order corrections matched to the parton shower (PS) in the POWHEG BOX framework and accounting for LO spin-correlations of the decay products were provided in ref. [24]. There has also been significant theoretical progress in calculating more complex and precise predictions. Higher-order QCD corrections including $t\bar{t}W$ production with additional partons (of order $\alpha\alpha_s^3$) open gluon-initiated production modes that contribute significantly to the total cross-section. Recent studies show that these contributions also have large NLO corrections, which require NLO-merged calculations for such effects to be included properly [27]. Furthermore, beyond the traditionally "leading" NLO EWK corrections (of order $\alpha^2\alpha_s^2$) there are even larger contributions from traditionally "sub-leading" NLO corrections (of order $\alpha^3\alpha_s$) [13, 17, 24] because of the presence of tW scattering contributions embedded in the $t\bar{t}Wj$ process. Calculations at NLO in QCD accounting for next-to-next-to-leading-logarithm (NNLL) effects are also available [18] and so are recent predictions at NLO+NNLL in QCD, also with NLO EWK corrections [19, 20]. The NNLL corrections can be as large as 7% of the NLO QCD cross-section, depending on the calculation and the functional form chosen for the scales. Full off-shell calculations at NLO in QCD [21–23] have also become available, and more recently the NLO EWK corrections were incorporated [25] into these calculations, along with the development of procedures to apply the off-shell corrections to NLO+PS simulations [26].

Most recently, a NNLO calculation in ref. [15] gives the state-of-the-art prediction for the inclusive $t\bar{t}W$ cross-section. This calculation is exact except for the finite part of the two-loop virtual corrections, which is computed using two different approaches with a corresponding uncertainty. The NNLO QCD result is combined with complete NLO EWK corrections.

Samples of simulated events were produced using Monte Carlo (MC) techniques to model the different SM processes. In particular, the estimation of the $t\bar{t}W$ signal and several backgrounds is based upon these simulations. More details of the event generation are given in the following paragraphs and are summarised in table 2, with the samples in black, or in parentheses and in grey, indicating those used as the nominal configurations, or to estimate the systematic uncertainties, respectively. Several data-driven corrections are applied to the estimated backgrounds and detailed in section 6.

JHEP05(2024)131

After generating events for each sample's process of interest, the detector response was modelled by either a full simulation of the ATLAS detector based on GEANT4 [40, 41] or a fast simulation (ATLFAST 2) relying on parameterised showers in the calorimeter [42, 43]. The latter was only used for the modelling of some rare background processes, such as $tHjb$ and WtH, and the modelling of the $t\bar{t}Z$ and $t\bar{t}H$ processes with alternative generators (see section 7). Additional simulated pp collisions, generated with PYTHIA 8.186 [44] using parameter values from the A3 tune [45], were overlaid to model the effects of both in-time and out-of-time pile-up. The pile-up distribution was reweighted to reflect the number of additional interactions observed in data. All simulated events are processed using the same reconstruction algorithms and analysis chain as the data. Corrections are applied so that the object reconstruction and identification efficiencies, energy scales and energy resolutions in simulation match those determined from data, with uncertainties described in section 7.1.

Several generators were studied for the simulation of $t\bar{t}W$ production, and multiple samples were generated to model this process. The events in the nominal $t\bar{t}W$ sample were simulated using the SHERPA 2.2.10 [46, 47] generator with the NNPDF3.0NNLO PDF set [48]. The matrix element (ME) was calculated for up to one additional parton at NLO and up to two partons at LO using COMIX [49] and OPENLOOPS [50–52], and merged with the SHERPA parton shower [53] using the MEPS@NLO prescription [54] with a merging scale of 30 GeV. The renormalisation and factorisation scales are chosen to be $\mu_{\mathrm{r}} = \mu_{\mathrm{f}} = H_{\mathrm{T}}/2$, where H_{T} is defined as the scalar sum of the transverse masses $\sqrt{p_{\mathrm{T}}^2 + m^2}$ of all final-state particles with transverse momentum p_{T} and invariant mass m. Top quarks were decayed at LO using the Sherpa particle decay program to preserve spin correlations. In addition to this nominal prediction at NLO in the strong coupling, higher-order corrections related to EWK contributions were also included in two ways. First, event-by-event correction factors were applied; these provide virtual NLO EWK corrections of order $\alpha^2\alpha_{\mathrm{s}}^2$ derived using the formalism described in ref. [55] along with LO corrections of order α^3, reducing the cross-section by 3.9% relative to NLO QCD. Both were implemented using the prescription described in refs. [46, 56]. Second, the real emission contributions of the sub-leading EWK corrections at order $\alpha^3\alpha_{\mathrm{s}}$ [17] were accounted for via the addition of an independent SHERPA 2.2.10 sample produced at LO in QCD. The combination of contributions from NLO QCD and NLO EWK effects taken from this SHERPA configuration closely follows the strategy described in ref. [27] and results in a total cross-section of $\sigma(t\bar{t}W) = 614.7\,\mathrm{fb}$.

In this measurement of $t\bar{t}W$ production cross-sections, the signal process is defined to include the combined QCD and EWK corrections, as described for the nominal SHERPA sample. The measured differential cross-sections are compared with theoretical predictions obtained from various generators, including the nominal SHERPA one. For one of the alternative predictions, the MADGRAPH5_AMC@NLO 2.9.3 program [57] generated $t\bar{t}W$ events with up to one additional parton in the final state at NLO accuracy in the strong coupling, using the NNPDF3.1NNLO [58] PDF set. The showering and subsequent hadronisation was performed using PYTHIA 8.245 with the A14 tune [59], and the NNPDF2.3LO [48] PDF set with $\alpha_{\mathrm{s}} = 0.130$. The decays of bottom and charm hadrons were performed by EVTGEN 1.6.0 [60]. The different jet multiplicities were merged using the FxFx NLO matrix-element and parton-shower merging prescription [61] with a merging scale of 30 GeV. This prediction uses a

JHEP05(2024)131

different merging scale and differs significantly from that in ref. [27], which is also based on the FxFx prescription. The top quarks were decayed at LO using the MadSpin [62, 63] particle decay program to preserve spin correlations. Several other predictions were made inclusively at NLO in α_s to investigate the effect of different additional-jet modelling. These come from (i) the MadGraph5_aMC@NLO 2.3.3 generator, which used the same scale choice and PDF set as the nominal Sherpa sample and was interfaced to Pythia 8.210 in combination with the A14 tune, (ii) the Powheg Box [24, 64–68] generator interfaced to Pythia 8, and (iii) the Powheg Box generator interfaced to Herwig 7 [69, 70]. The top quarks were decayed at LO withing the Powheg Box program to preserve spin correlations. A final prediction, used to assess the impact of off-shell contributions to $t\bar{t}W$ production, was calculated at fixed order and includes full NLO off-shell effects using the procedure outlined in ref. [23].

The production of $t\bar{t}H$ events was modelled using the Powheg Box v2 generator at NLO with the NNPDF3.0nlo PDF set. The events were interfaced to Pythia 8.230 using the A14 tune and the NNPDF2.3lo PDF set. The decays of bottom and charm hadrons were performed by EvtGen 1.6.0. The h_{damp} parameter[2] was set to $0.75 \times (m_t + m_{\bar{t}} + m_H) = 352.5\,\text{GeV}$. The cross-section was calculated at NLO QCD and NLO EWK accuracy using MadGraph5_aMC@NLO as reported in ref. [16]. The predicted value at $\sqrt{s} = 13\,\text{TeV}$ is $507^{+35}_{-50}\,\text{fb}$, where the uncertainties were estimated from the combined PDF+α_s uncertainties and variations of the renormalisation and factorisation scales.

Background events from $t\bar{t}Z/\gamma^*$ production were simulated using the MadGraph5_aMC@NLO 2.8.1 generator at NLO in α_s with the NNPDF3.0nlo PDF set. The functional form of the renormalisation and factorisation scales (μ_r, μ_f) was set to the default scale $0.5 \times \sum_i \sqrt{m_i^2 + p_{\text{T},i}^2}$, where the sum runs over all the particles generated from the matrix element calculation. Top quarks were decayed at LO using MadSpin [62, 63] to preserve all spin correlations. The showering and subsequent hadronisation was performed using Pythia 8.244 with the A14 tune, and the NNPDF2.3lo PDF set with $\alpha_s = 0.130$. The decays of bottom and charm hadrons were performed by EvtGen 1.7.0. The $t\bar{t}Z/\gamma^*(\to \ell^+\ell^-)$ prediction was normalised to the calculation at NLO QCD and NLO EWK accuracy reported in ref. [16] for an on-shell Z boson, scaled to the leptonic contributions including off-shell $\gamma^* \to \ell^+\ell^-$ contributions with a correction estimated at one-loop level in α_s. The resulting $t\bar{t}\ell^+\ell^-$ cross-section, with $m(\ell^+\ell^-) > 1$ GeV, is $162 \pm 21\,\text{fb}$. A dedicated $t\bar{t}$ sample including rare $t \to Wb\gamma^*(\to \ell^+\ell^-)$ radiative decays, i.e. $t\bar{t} \to W^+bW^-\bar{b}\ell^+\ell^-$, was generated using a LO ME and requiring $m(\ell^+\ell^-) > 1\,\text{GeV}$. In this sample the photon can be radiated from the top quark, the W boson, or the b-quark. The $t\bar{t}Z/\gamma^*$ and $t\bar{t} \to W^+bW^-\bar{b}\ell^+\ell^-$ samples were combined and together form the "$t\bar{t}Z/\gamma^*$" sample. The contribution from internal photon conversions ($\gamma^* \to \ell^+\ell^-$) with $m(\ell^+\ell^-) < 1\,\text{GeV}$ was modelled with QED multiphoton radiation via the parton shower in an inclusive $t\bar{t}$ sample. Care was taken to avoid both double-counting of contributions and uncovered regions of phase space when combining the different simulated event samples. The LO cross-section for the $t\bar{t} \to W^+bW^-\bar{b}\ell^+\ell^-$ sample was scaled to match the higher-order cross-section used for $t\bar{t}$ production in the phase space they overlap, and was assigned a 50% normalisation uncertainty.

[2]The h_{damp} parameter is a resummation damping factor and one of the parameters that controls the matching of Powheg matrix elements to the parton shower and thus effectively regulates the high-p_{T} radiation against which the hard-process system recoils.

JHEP05(2024)131

The production of $t\bar{t}$ and single-top-quark events was modelled using the Powheg Box v2 [64–67, 71–73] generator at NLO with the NNPDF3.0nlo PDF set. The events were interfaced to Pythia 8.230 to model the parton shower, hadronisation, and underlying event, using the A14 tune and the NNPDF2.3lo set of PDFs. The decays of bottom and charm hadrons were performed by EvtGen 1.6.0. The $t\bar{t}$ process was modelled with the h_{damp} parameter set to $1.5\,m_t$ [74]. The production of a top quark in association with a W boson (tW) was modelled using the five-flavour scheme. The diagram removal scheme [75] was used to remove interference and overlap with $t\bar{t}$ production. Single-top s- and t-channel production was modelled using the Powheg Box v2 [72, 73] generator at NLO in QCD using the five- and four-flavour schemes, respectively, and the corresponding NNPDF3.0nlo set of PDFs. The $t\bar{t}$ sample was normalised to the cross-section prediction at NNLO in QCD including the resummation of NNLL soft-gluon terms calculated using Top++ 2.0 [76–82]. This cross-section is $\sigma(t\bar{t})_{\text{NNLO+NNLL}} = 832 \pm 51\,\text{pb}$. The single-top-quark tW-channel inclusive cross-section was corrected to the theory prediction calculated at approximate NNLO in QCD with NNLL soft-gluon corrections [83, 84]: $\sigma(t, tW)_{\text{aNNLO+NNLL}} = 71.7 \pm 3.8$ pb. The single-top-quark s- and t-channel inclusive cross-sections are corrected to theory predictions calculated at NLO in QCD [85, 86]: $\sigma(t, s\text{-chan})_{\text{NLO}} = 6.35^{+0.23}_{-0.20}$ pb and $\sigma(t, t\text{-chan})_{\text{NLO}} = 216.97^{+9.46}_{-8.18}$ pb.

Diboson events with fully leptonic decays (yielding between zero and four charged leptons) were generated by Sherpa 2.2.2 with up to one additional parton at NLO and three additional partons at LO. Sherpa 2.2.1 was used for diboson semileptonic decays at the same accuracy. The EWK $VVjj$ ($V = W, Z$) process was simulated for fully leptonic decays with one additional parton at LO using Sherpa 2.2.2. Events of vector boson production in association with additional jets, V+jets, were generated using Sherpa 2.2.1 with two additional partons at NLO and four additional partons at LO. The EWK $VVjj$ ($V = W, Z$) process was simulated for fully leptonic decays with one additional parton at LO using Sherpa 2.2.2.

Rare background contributions (tZ, $t\bar{t}t\bar{t}$, $ttWW$, WtZ, triboson, $tt\bar{t}$, $tHjb$ and WtH) were normalised using their NLO theoretical cross-sections. The production of four top quarks, $t\bar{t}t\bar{t}$, was normalised to the theoretical prediction of $\sigma(t\bar{t}t\bar{t}) = 13.37\,\text{fb}$ in ref. [87], with an assumed 100% normalisation uncertainty based on the larger cross-section measured recently for this process by ATLAS [11]. A 30% uncertainty [88] was assumed for triboson production, while a 5% uncertainty was used for tZ production, and all other rare backgrounds were assigned a 50% normalisation uncertainty.

4 Event reconstruction and object identification

Interaction vertices from the pp collisions are reconstructed from at least two tracks with p_{T} larger than 500 MeV that are consistent with originating from the beam collision region in the x–y plane. If more than one primary vertex candidate is found in the event, the candidate for which the associated tracks form the largest sum of squared p_{T} is selected as the hard-scatter primary vertex [89].

Electron candidates are reconstructed from energy clusters in the electromagnetic calorimeter matched to a track in the ID [90]. They are required to satisfy $p_{\text{T}} > 10\,\text{GeV}$ and $|\eta_{\text{cluster}}| < 2.47$, excluding the transition region between the endcap and barrel calorimeters

JHEP05(2024)131

Process	Generator	ME order	Parton shower	PDF	Tune
$t\bar{t}W$	Sherpa 2.2.10	MEPS@NLO	Sherpa	NNPDF3.0nnlo	Sherpa default
	(MG5_aMC)	(FxFx NLO)	(Pythia 8)	(NNPDF3.0nnlo)	(A14)
	(Powheg)	(NLO)	(Pythia 8)	(NNPDF3.0nlo)	(A14)
	(Powheg)	(NLO)	(Herwig 7)	(NNPDF3.0nlo)	(H7-UE-MMHT)
$t\bar{t}W$ (EW)	Sherpa 2.2.10	LO	Sherpa	NNPDF3.0nnlo	Sherpa default
	(MG5_aMC)	(LO)	(Pythia 8)	(NNPDF3.0nlo)	(A14)
$t\bar{t}H$	Powheg Box	NLO	Pythia 8	NNPDF3.0nlo	A14
	(Powheg Box)	(NLO)	(Herwig 7.0.4)	(NNPDF3.0nlo)	(H7-UE-MMHT)
	(MG5_aMC)	(NLO)	(Pythia 8)	(NNPDF3.0nlo)	(A14)
$t\bar{t}\ell\ell$	MG5_aMC	NLO	Pythia 8	NNPDF3.0nlo	A14
	(MG5_aMC)	(NLO)	(Pythia 8)	(NNPDF3.0nlo)	(A14 Var3c)
	(MG5_aMC)	(NLO)	(Herwig 7)	(NNPDF3.0nlo)	(H7-UE-MMHT)
$t\bar{t} \to W^+bW^-\bar{b}\ell^+\ell^-$	MG5_aMC	LO	Pythia 8	NNPDF3.0lo	A14
$t\bar{t}t\bar{t}$	MG5_aMC	NLO	Pythia 8	NNPDF3.1nlo	A14
$t\bar{t}WW, WtZ, t\bar{t}t, tHjb, WtH$	MG5_aMC	LO	Pythia 8	NNPDF2.3lo	A14
tZ	MG5_aMC	LO	Pythia 8	NNPDF3.1nlo	A14
$t\bar{t}$	Powheg Box	NLO	Pythia 8	NNPDF3.0nlo	A14
	(Powheg Box)	(NLO)	(Herwig 7.1.3)	(NNPDF3.0nlo)	(H7-UE-MMHT)
Single top (t-, Wt-, s-channel)	Powheg Box	NLO	Pythia 8	NNPDF3.0nlo	A14
VV, $qqVV$, VVV	Sherpa 2.2.2	MEPS@NLO	Sherpa	NNPDF3.0nnlo	Sherpa default
$Z \to \ell^+\ell^-$	Sherpa 2.2.1	MEPS@NLO	Sherpa	NNPDF3.0nlo	Sherpa default
$Z \to \ell^+\ell^-\gamma(\to e^+e^-)$	Powheg Box	NLO	Pythia 8	CTEQ6L1nlo	A14
$Z \to \ell^+\ell^-\gamma^*(\to e^+e^-)$	Powheg Box	NLO	Pythia 8	CTEQ6L1nlo	A14

Table 2. The configurations used to generate events from signal and background processes. The samples used to estimate the systematic uncertainties are indicated in parentheses and in grey.

$(1.37 < |\eta_{\text{cluster}}| < 1.52)$. "Loose" and "tight" electron identification working points are used, based on a likelihood discriminant employing calorimeter, tracking and combined variables that provide separation between electrons and jets.

Muon candidates are reconstructed by performing a combined fit of the track information from the ID and MS [91]. The resulting muon candidates are re-fitted using the complete track information from both detector systems. They are required to satisfy $p_{\text{T}} > 10$ GeV and $|\eta| < 2.5$. "Loose" and "medium" muon identification working points are used.

Electron (muon) candidates are matched to the primary vertex by requiring that the significance of their transverse impact parameter, d_0,[3] satisfies $|d_0/\sigma(d_0)| < 5\,(3)$, where $\sigma(d_0)$ is the measured uncertainty in d_0, and by requiring that their longitudinal impact parameter, z_0,[4] satisfies $|z_0 \sin\theta| < 0.5$ mm.

[3]The transverse impact parameter, d_0, is defined in the x–y plane as the distance of closest approach of the track to the beamline.

[4]The longitudinal impact parameter, z_0, is defined as the distance in z between the primary vertex and the point on the track used to evaluate d_0.

JHEP05(2024)131

To further suppress leptons from heavy-flavour hadron decays, misidentified jets, or photon conversions (collectively referred to as "non-prompt leptons"), lepton candidates are also required to be isolated in the tracker and in the calorimeter. The track-based lepton isolation criterion is based on the quantity $I_R = \sum p_{\mathrm{T}}^{\mathrm{trk}}$, where the scalar sum includes all tracks (excluding the lepton candidate itself) within a cone of size $\Delta R < R_{\mathrm{cut}}$ around the direction of the lepton. The value of R_{cut} is the smaller of r_{min} and 10 GeV/p_{T}^{ℓ}, where r_{min} is set to 0.2 (0.3) for electron (muon) candidates and p_{T}^{ℓ} is the lepton's p_{T}. All lepton candidates must satisfy $I_R/p_{\mathrm{T}}^{\ell} < 0.15$. They are also required to satisfy a calorimeter-based isolation criterion: the sum of the transverse energy within a cone of size $\Delta R = 0.2$ around the lepton, after subtracting contributions from pile-up and the energy deposit of the lepton itself, is required to be less than 20% (30%) of the electron's (muon's) p_{T}^{ℓ}.

These selection criteria largely suppress the contribution from non-prompt leptons. However, several channels considered in this measurement have additional suppression requirements targeting the main types of non-prompt leptons. Non-prompt leptons from hadron decays that contain bottom- or charm-quarks (referred to as "heavy-flavour (HF) non-prompt leptons") are further rejected using a boosted decision tree (BDT) discriminant, referred to as the non-prompt-lepton BDT [92], based on isolation and lifetime information about a track-jet that matches the selected electron or muon (referred to as a "light lepton"). Three working points (WPs) based on the non-prompt-lepton BDT are used: *Tight*, *VeryTight*, and *Tight-not-VeryTight*. The *Tight* WP allows prompt muons (barrel/endcap electrons) satisfying the calorimeter- and track-based isolation criteria to be selected with an efficiency that is about 60% (60%/70%) for $p_{\mathrm{T}} \sim 20$ GeV and reaches a plateau of 95% (95%/90%) for $p_{\mathrm{T}} \sim 40$ (40/65) GeV. The prompt-lepton efficiency of the *VeryTight* WP for muons (barrel/endcap electrons) that satisfy the calorimeter- and track-based isolation criteria is about 55% (55%/60%) for $p_{\mathrm{T}} \sim 20$ GeV and reaches a plateau of 90% (85%/83%) for $p_{\mathrm{T}} \sim 40$ (40/65) GeV. The corresponding rejection factor[5] for muons (electrons) from the decay of b-hadrons ranges from 33 to 50 (20 to 50) for the *Tight* WP, and from 50 to 100 (33 to 66) for the *VeryTight* WP, depending on p_{T} and η, after resolving ambiguities between overlapping reconstructed objects. The *Tight-not-VeryTight* WP allows the selection of non-prompt leptons and is part of the event selection for control regions enriched in HF non-prompt-lepton background, as described in section 6.

In order to further suppress electrons with incorrect charge assignment, a BDT discriminant based on calorimeter and tracking quantities [93] is used. An efficiency of approximately 96% in the barrel region and 81% in the endcaps is obtained, with rejection factors of 19 in the barrel region and 40 in the endcaps. The electron candidates are separated into three classes: "material conversion", "internal conversion", and "non-conversion" electron candidates. Most electrons arising from material conversions, i.e. from photon conversions in the detector material, are rejected by the standard electron identification selection, but additional requirements are imposed to remove residual material-conversion candidates. These candidates have a reconstructed displaced vertex with radius $r > 20$ mm that includes the track associated with the electron.[6] The invariant mass of the associated track and the

[5]The rejection factor is defined as the reciprocal of the efficiency.

[6]The beampipe and insertable B-layer inner radii are 23.5 mm and 33 mm, respectively.

JHEP05(2024)131

	Electron				Muon			
Lepton definition	L	M	M_{ex}	T	L	M	M_{ex}	T
Identification	Loose	Tight			Loose	Medium		
Transverse impact parameter significance $\lvert d_0\rvert/\sigma_{d_0}$	< 5				< 3			
Longitudinal impact parameter z_0	$\lvert z_0 \sin\theta\rvert < 0.5$ mm							
Isolation	Yes				Yes			
Non-prompt lepton WP	No	*Tight*	*Tight-not-VeryTight*	*VeryTight*	No	*Tight*	*Tight-not-VeryTight*	*VeryTight*
Electron charge-misassignment veto	No	Yes			–			
Electron conversion candidate veto	No	Yes (except e^*)			–			

Table 3. Description of the loose inclusive (L), medium inclusive (M), medium exclusive (M_{ex}), and tight (T) lepton definitions. The electron e^* is required to fulfil, in addition to the corresponding lepton definition requirements, those corresponding to an internal or material conversion candidate.

closest (in $\Delta\eta$) opposite-charge track reconstructed in the silicon detector, calculated at the conversion vertex, is required to be < 100 MeV. Internal conversion candidates, which correspond to the internal photon conversions (see section 3), must fail the requirements for material conversions, and the di-track invariant mass, calculated here at the primary vertex, is also required to be < 100 MeV.

The various lepton working points used in this analysis are summarised in table 3. After the initial categorisation based on "loose" leptons (corresponding to L), the best lepton working point to further optimise the event selection is chosen; it depends on the main background processes and available amount of data in each category. The various choices for the signal and control regions are described in section 5.

The constituents for jet reconstruction are identified by combining measurements from both the ID and the calorimeter using a particle flow (PFlow) algorithm [94]. Jet candidates are reconstructed from these PFlow objects using the anti-k_t algorithm [95, 96] with a radius parameter of $R = 0.4$. They are calibrated using simulation with corrections obtained by using in situ techniques in data [97]. Only jet candidates with $p_{\text{T}} > 25$ GeV and within $|\eta| < 2.5$ are selected. In order to reduce the effect of pile-up, each jet with $p_{\text{T}} < 60$ GeV and $|\eta| < 2.4$ must satisfy the "Tight" working point of the Jet Vertex Tagger (JVT) [98] criteria used to identify jets that originate from the primary vertex. A set of quality criteria is also applied to reject events containing at least one jet arising from non-collision sources or detector noise [99].

Jets containing b-hadrons are identified (b-tagged) via an algorithm [100] that uses a deep-learning neural network based on the distinctive features of b-hadron decays, primarily the impact parameters of tracks and the displaced vertices reconstructed in the ID. Additional input to this network is provided by discriminating variables constructed by a recurrent neutral network [101], which exploits the spatial and kinematic correlations between tracks originating from the same b-hadron. A multivariate b-tagging discriminant value is calculated for each jet. In this measurement, a jet is considered b-tagged if it passes the working point corresponding to 85%, 77%, 70%, or 60% average expected efficiency to tag a b-quark jet,

JHEP05(2024)131

with a light-jet[7] rejection factor of about 40 to 2500, and a charm-jet (c-jet) rejection factor of about 3 to 40, as determined for jets with $p_{\mathrm{T}} > 20$ GeV and $|\eta| < 2.5$ in simulated $t\bar{t}$ events. The notation $b^{85\%}$, $b^{77\%}$, $b^{70\%}$, and $b^{60\%}$ is used to denote a b-tagged jet (b-jet) that passed the corresponding working point. Correction factors derived from dedicated calibration samples enriched in b-jets, c-tagged jets, or light-tagged jets, are applied to the simulated event samples [102–104].

Ambiguities between independently reconstructed electrons, muons and jets can arise. A sequential "overlap removal" procedure is performed to resolve these ambiguities and thus avoid double counting of candidates. This procedure is applied to leptons satisfying the L criteria. If two electrons are separated by $\Delta R < 0.1$, only the one with the higher p_{T} is kept. If an electron and a muon overlap within $\Delta R < 0.1$, the muon is removed if it is reconstructed only from an ID track and calorimeter energy deposits consistent with a minimum-ionising particle (i.e. if it is "calo-tagged"), otherwise the electron is removed. If an electron and a selected jet are found within $\Delta R < 0.2$, the jet is removed if it is not a $b^{70\%}$ jet[8] or if it has $p_{\mathrm{T}} > 200$ GeV. Muons ghost-associated [105] with an $R = 0.4$ jet must satisfy a jet-muon separation of $\Delta R < 0.4$. If the overlapping jet is not a $b^{70\%}$ jet and contains less than three tracks with $p_{\mathrm{T}} > 500$ MeV, the jet is removed, otherwise the muon is rejected. Thus, if the overlapping jet is a $b^{70\%}$ jet, the muon is rejected. For each lepton in the event a lepton-p_{T}-dependent variable-size cone of maximum size $\Delta R = 0.4$ is defined. If a selected jet, surviving all previous overlap criteria, is found in this cone, the lepton is rejected.

The missing transverse momentum $\vec{p}_{\mathrm{T}}^{\,\mathrm{miss}}$ (with magnitude $E_{\mathrm{T}}^{\mathrm{miss}}$) is defined as the negative vector sum of the p_{T} of all selected and calibrated objects in the event, including a term to account for the momenta of soft particles that are not associated with any of the selected objects [106]. This soft term is calculated from inner-detector tracks matched to the primary vertex, which makes it more resilient to contamination from pile-up interactions.

5 Analysis strategy

The events used in the analysis were selected with high efficiency using dilepton triggers [107, 108], based on electron and muon signatures. The dielectron triggers required two electrons that satisfied loose identification criteria with p_{T} thresholds that were raised as the luminosity increased during Run 2: 12 GeV in 2015, 17 GeV in 2016, and 24 GeV in 2017–2018. Dimuon triggers utilised asymmetric p_{T} thresholds for leading (sub-leading) muons: 18 (8) GeV in 2015 and 22 (8) GeV in 2016–2018. An electron+muon trigger required events to have an electron candidate satisfying loose identification with a 17 GeV threshold and a muon candidate passing a 14 GeV threshold for all data-taking periods.

Events selected by the trigger are required to satisfy basic preselection requirements. They must have at least one primary vertex candidate. Events are required to contain either two light leptons with the same electric charge or three light leptons, based on the loose lepton definition L introduced in section 4. This event categorisation into 2ℓSS and 3ℓ reduces

[7] 'Light jet' refers to a jet originating from the hadronisation of a light quark (u, d, s) or a gluon.

[8] For the overlap removal, a jet is considered b-tagged if it passes the 70% working point. However, the choice of b-tagging working point does not have a sizeable impact on the signal acceptance.

JHEP05(2024)131

the migration of events from 3ℓ $t\bar{t}W$ decays into the 2ℓ channel, which can occur, for example, due to improper identification of leptons (i.e. reconstruction inefficiencies).

The selected light leptons are required to match, with $\Delta R < 0.15$, the corresponding leptons reconstructed by the trigger and to have a p_{T} exceeding the trigger p_{T} threshold by 1 GeV or 2 GeV (depending on the lepton trigger, lepton multiplicity criteria, and data-taking conditions). The trigger requirement has an efficiency of about 82% for signal events with at least two light leptons satisfying the preselection requirements.

Once the events are separated into the 2ℓSS and 3ℓ channels, control regions (CRs) and signal regions (SRs) are defined by using different lepton and event requirements to enhance the fraction of certain backgrounds or the $t\bar{t}W$ signal, respectively, in those regions.

The signal regions are split into 2ℓSS and 3ℓ categories. The 3ℓ events are required to have the sum of charges of selected leptons (total lepton charge) to be exactly ± 1. Events are required to contain at least one $b^{60\%}$ jet, or at least two $b^{77\%}$ jets. If 3ℓ events contain pairs of opposite-sign charge and same-flavour (OS-SF) leptons, all such pairs must satisfy requirements on the dilepton system mass of $m^{\mathrm{SF}}_{\ell^+\ell^-} > 12$ GeV and $|m^{\mathrm{SF}}_{\ell^+\ell^-} - m_Z| > 10$ GeV. Additionally, 3ℓ events must satisfy $|m_{3\ell} - m_Z| > 10$ GeV. Leptons are ordered in p_{T} in the 2ℓSS regions. In the 3ℓ regions the lepton with opposite-sign charge is called the first lepton, followed by the two same-sign leptons. The p_{T} and identification requirements for each lepton in each category are optimised, accounting for the different likelihood of being non-prompt, and are summarised in table 4.

Events passing the 2ℓSS and 3ℓ signal region selections are separated into subcategories depending on whether the inclusive or differential $t\bar{t}W$ cross-sections are being measured, as shown in table 4. For the $t\bar{t}W$ differential measurements, two 2ℓSS and six 3ℓ signal categories, based on the total lepton charge of the event and on the number of OS-SF lepton pairs in the 3ℓ channel, are defined in section 8.2. The inclusive $t\bar{t}W$ measurement (see section 8.1) is improved by assigning the preselected events to subcategories based on the total lepton charge, the lepton flavour, and the jet and b-jet multiplicities (N_{jets} and $N_{b\text{-jets}}$, respectively), where $N_{b\text{-jets}}$ is defined to be 2 or more if the events contain at least two $b^{77\%}$ jets, or 1 if the events contain exactly one $b^{60\%}$ jet. As a result, the $t\bar{t}W$ inclusive measurement is performed in 48 2ℓSS and 8 3ℓ signal categories.

Various control regions are defined in order to fit the normalisation of the leading backgrounds. Two regions enriched in either diboson or $t\bar{t}Z$ events are defined by requiring one OS-SF lepton pair compatible with a Z boson, $|m^{\mathrm{SF}}_{\ell^+\ell^-} - m_Z| < 10$ GeV, but different jet multiplicities. These regions are labelled as 3ℓVV and 3ℓttZ for the diboson and $t\bar{t}Z$ CRs, respectively. Two control regions enriched in electron-from-photon conversions from $Z \to \mu^+\mu^-\gamma^{(*)} \to \mu^+\mu^- e^+ e^-$, where one of the electrons is not reconstructed, are defined, according to the identification of the electron as a material conversion or internal conversion candidate, and are labelled as 3ℓMatC and 3ℓIntC, respectively. Finally, six control regions enriched in HF non-prompt leptons are defined, making use of the exclusive lepton identification M_{ex} in order to be orthogonal to the signal regions. Events fulfilling the criteria TM_{ex}, $M_{\mathrm{ex}}T$, or $M_{\mathrm{ex}}M_{\mathrm{ex}}$ for the leading and sub-leading leptons in p_{T} are selected and further separated according to the sub-leading lepton flavour. Additionally, the transverse mass of the leading lepton, ℓ_0, and the missing transverse momentum, defined as $m_{\mathrm{T}}(\ell_0, E_{\mathrm{T}}^{\mathrm{miss}}) = \sqrt{2E_{\mathrm{T}}^{\mathrm{miss}} p_{\mathrm{T},\ell_0}(1 - \cos(\phi_{\mathrm{miss}} - \phi_{\ell_0}))}$,

JHEP05(2024)131

Signal region preselection	2ℓSS	3ℓ
Lepton definition	TT	LTT
Lepton p_{T} [GeV]	(20, 20)	(10, 20, 20)
$m^{\mathrm{SF}}_{\ell^+\ell^-}$ [GeV]	—	> 12
$\lvert m^{\mathrm{SF}}_{\ell^+\ell^-} - m_Z\rvert$ [GeV]	—	> 10
$\lvert m_{3\ell} - m_Z\rvert$ [GeV]	—	> 10
N_{jets}	≥ 2	
$N_{b\text{-jets}}$	$\geq 1\ b^{60\%}$ or $\geq 2\ b^{77\%}$	
	Inclusive cross-section measurement	
Lepton charge split	$(\ell^+\ell^+, \ell^-\ell^-)$	$(\ell^+\ell^-\ell^-, \ell^-\ell^+\ell^+)$
Lepton flavour split	($\mu\mu$, $e\mu$, μe, ee)	—
Jet multiplicity split	(3, 4, $\geq$5)	(2, $\geq$3)
b-jet multiplicity split	(1, $\geq$2)	
Total inclusive SRs	48	8
	Differential cross-section measurement	
Lepton charge split	$(\ell^+\ell^+, \ell^-\ell^-)$	$(\ell^+\ell^-\ell^-, \ell^-\ell^+\ell^+)$
Number of OS-SF pairs split	—	(0, 1, 2)
Total differential SRs	2	6

Table 4. Event selection summary in the signal regions. Leptons are ordered in p_{T} in the 2ℓSS regions. In the 3ℓ regions the lepton with opposite-sign charge is called the first lepton, followed by the two same-sign leptons. In the lepton selection, T and L stand for tight and loose lepton definitions (see table 3). In the b-jet multiplicity categorisation, $N_{b\text{-jets}}$ is defined to be 2 or more if the events contain at least two $b^{77\%}$ jets, or 1 if the events contain exactly one $b^{60\%}$ jet. For each of the 2ℓSS and 3ℓ signal regions in the inclusive and differential measurements, each categorisation split affects all regions above.

must be less than 250 GeV in the TM_{ex} and $M_{\mathrm{ex}}T$ regions, in order to reduce the $t\bar{t}W$ contribution in these CRs. The full definition of the kinematic selection applied to events in each control region is given in table 5.

5.1 Fiducial-volume definition

The particle-level fiducial volume closely follows the reconstruction-level selection to avoid the uncertainties in extrapolating to a more inclusive phase space. Table 6 summarises the object requirements, overlap removal and region selections applied to define the fiducial regions. The fiducial selections are the same for the inclusive and differential cross-section measurements, except in the 2ℓSS channel, where a higher jet multiplicity is required for the inclusive measurement. This is because at detector level the $N_{\mathrm{jets}} = 2$ bin does not add

JHEP05(2024)131

Control regions for:	Diboson	$t\bar{t}Z$	Conversions	HF non-prompt
Lepton requirement		3ℓ	$\mu\mu e^*$	2ℓSS
Lepton definition		(L, M, M)		(T, M_{ex}) | (M_{ex}, T) | $(M_{\text{ex}}, M_{\text{ex}})$
Lepton p_{T} [GeV]		(10, 20, 20)		(20, 20)
$m^{\text{SF}}_{\ell^+\ell^-}$ [GeV]		> 12	> 12	—
$\lvert m^{\text{SF}}_{\ell^+\ell^-} - m_Z\rvert$ [GeV]		< 10	> 10	—
$\lvert m_{3\ell} - m_Z\rvert$ [GeV]		> 10	< 10	—
$m_{\text{T}}(\ell_0, E_{\text{T}}^{\text{miss}})$ [GeV]		—		< 250 for TM_{ex} and $M_{\text{ex}}T$ pairs
N_{jets}	2 or 3	≥ 4	≥ 0	≥ 2
$N_{b\text{-jets}}$	1 $b^{60\%}$	≥ 1 $b^{60\%}$ or ≥ 2 $b^{77\%}$	0 $b^{77\%}$	1 $b^{77\%}$
Region split	—	—	internal / material	sub-leading $e/\mu \times (TM_{\text{ex}}, M_{\text{ex}}T, M_{\text{ex}}M_{\text{ex}})$
Region naming	3ℓVV	3ℓttZ	3ℓIntC / 3ℓMatC	$2\ell\text{tt(e)}_{TM_{\text{ex}}}$, $2\ell\text{tt(e)}_{M_{\text{ex}}T}$, $2\ell\text{tt(e)}_{M_{\text{ex}}M_{\text{ex}}}$ $2\ell\text{tt}(\mu)_{TM_{\text{ex}}}$, $2\ell\text{tt}(\mu)_{M_{\text{ex}}T}$, $2\ell\text{tt}(\mu)_{M_{\text{ex}}M_{\text{ex}}}$

Table 5. Event selection summary in the control regions. The lepton types L, M, M_{ex}, and T correspond to the loose inclusive, medium inclusive, medium exclusive, and tight lepton definitions, as described in table 3. The notation e^* is used to denote material conversion or internal conversion candidates, as described in section 4.

significant sensitivity to the inclusive cross-section measurement and is therefore omitted, and the fiducial selection matches the detector-level selection.

Particle-level objects in simulated events are defined using quasi-stable particles with a mean lifetime greater than 30 ps originating from pp collisions. They are selected after hadronisation but before the interaction of these particles with the detector components or consideration of pile-up effects. Electrons and muons are required not to have originated from a hadron in the MC generator's event record, either directly or through a τ-lepton decay, to ensure that they originated from one of the W boson decays. The leptons are modified ("dressed") by adding the four-momenta of all radiated photons within a cone of size $\Delta R = 0.1$, excluding photons from hadron decays, to take into account final-state photon radiation. Particle-level jets are reconstructed with the anti-k_t algorithm with a radius parameter of $R = 0.4$ applied to all quasi-stable particles except the neutrinos originating from W bosons and the selected electrons, muons and photons used in the definition of the charged leptons. If b-hadrons with $p_{\text{T}} > 5\,\text{GeV}$ are found in the MC event record, they are ghost-associated to jets. Any jets containing one or more of these b-hadrons are considered to originate from a b-quark. The particle-level missing transverse momentum is calculated from the vector sum of the transverse momenta of all neutrinos in the event record, excluding those originating from hadron decays.

6 Background estimation

The background processes passing the signal region selections are categorised into irreducible and reducible backgrounds. Irreducible backgrounds (section 6.1) have only prompt selected leptons, i.e. leptons produced in W/Z boson decays, leptonic τ-lepton decays, or internal conversions. Reducible backgrounds (section 6.2) have prompt leptons with misassigned charge or at least one non-prompt lepton.

JHEP05(2024)131

Objects	
Electrons	$p_{\mathrm{T}} \geq 10$ GeV and $\lvert\eta\rvert < 2.47$ (excluding the LAr transition region $1.37 < \lvert\eta\rvert < 1.52$)
Muons	$p_{\mathrm{T}} \geq 10$ GeV and $\lvert\eta\rvert < 2.5$
Jets	Anti-k_t $R = 0.4$ jets with $p_{\mathrm{T}} \geq 25$ GeV and $\lvert\eta\rvert < 2.5$
b-jets	Tagged if jet contains a ghost-associated b-hadron with $p_{\mathrm{T}} > 5$ GeV
$E_{\mathrm{T}}^{\mathrm{miss}}$	Vector sum of p_{T} for all neutrinos ($p_{\mathrm{T}}(\nu)$) in the event not from hadron decays
Overlap removal	
Electron-jet	If $\Delta R(e, \mathrm{jet}) < 0.2$ (excluding b-jets with $p_{\mathrm{T}} < 200$ GeV) remove jet
Jet-lepton	If $\Delta R(\ell, \mathrm{jet}) < \min(0.4, 0.04 + 10\,\mathrm{GeV}/p_{\mathrm{T},\ell})$ remove lepton
Selections	
2ℓSS	Exactly two leptons with the same charge
	Both leptons have $p_{\mathrm{T}} \geq 20$ GeV
	$N_{\mathrm{jets}} \geq 3$ ($N_{\mathrm{jets}} \geq 2$) with at least one b-jet for inclusive (differential) fit
	$m_{\ell\ell} > 12$ GeV for same-flavour pairs
3ℓ	Exactly three leptons with a total charge of ± 1
	Both leptons from the same-sign lepton pair are required to have $p_{\mathrm{T}} \geq 20$ GeV
	$N_{\mathrm{jets}} \geq 1$ with at least one b-jet
	$m_{\ell\ell} > 12$ GeV & $\lvert m_{\ell\ell} - m_Z\rvert > 10$ GeV (for OS-SF $\ell\ell$)
	$\lvert m_{\ell\ell\ell} - m_Z\rvert > 10$ GeV

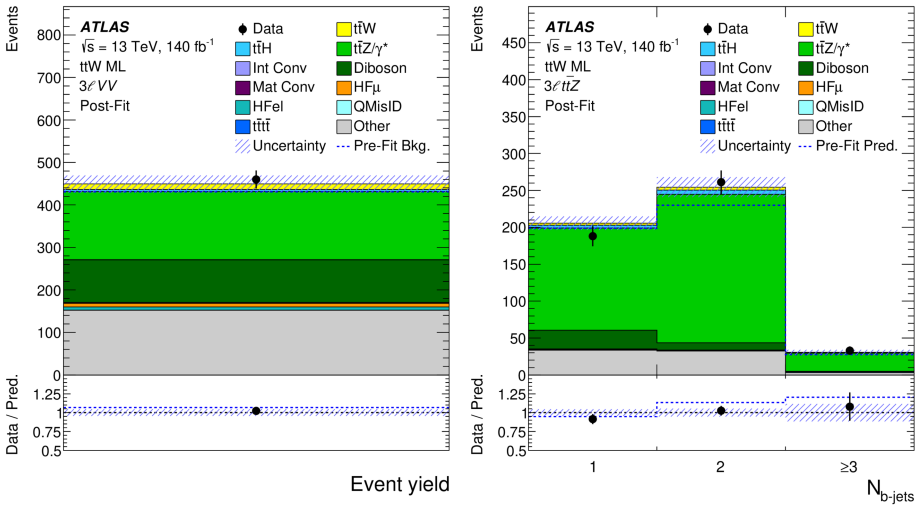
Table 6. Definition of objects and selections for fiducial regions.

All backgrounds with the exception of electrons with misassigned charge (denoted by QMisID) are estimated using the simulated event samples described in section 3. In some cases, the simulation is improved by applying additional corrections derived from data control samples before the statistical analysis. In particular, the event kinematics of the simulated $t\bar{t}$ and VV backgrounds require dedicated corrections to better describe the data. In addition, the yields of some simulated backgrounds, namely $t\bar{t}Z$, VV and non-prompt-lepton backgrounds, are adjusted via normalisation factors that are determined by performing a likelihood fit to data across all event categories in the signal and control regions defined in tables 4 and 5, as discussed in section 8.

6.1 Irreducible backgrounds

Background contributions with prompt leptons originate from a wide range of physics processes, with the relative importance of individual processes varying by channel. The main irreducible backgrounds originate from $t\bar{t}Z/\gamma^*$, VV (especially WZ), and $t\bar{t}H$ production, having final states and kinematic properties inherently similar to the $t\bar{t}W$ signal. Smaller contributions originate from the following rare processes: tZ, tW, tWZ, $t\bar{t}WW$, VVV, $t\bar{t}t\bar{t}$, and $t\bar{t}t$ production. Backgrounds with prompt leptons are estimated from simulation using the samples described in section 3.

JHEP05(2024)131



(a) (b)

Figure 2. Comparison between data and the signal-plus-background prediction for (a) the total yield in the 3ℓVV CR and (b) the distribution of the b-jet multiplicity in the 3ℓttZ CR after the VV jet multiplicity correction. The signal and background contributions after the likelihood fit to data ("Post-Fit") under the signal-plus-background hypothesis are shown as filled histograms. The total signal-plus-background prediction before the likelihood fit to data ("Pre-Fit Bkg.") is shown as a dashed blue histogram in the upper panel. The ratio of the data to the total prediction ("Pred.") is shown in the lower panel, separately for the post-fit prediction (black points) and pre-fit background (dashed blue line). The combined statistical and systematic uncertainty in the prediction is indicated by the blue hatched band. The "Other" background contribution is dominated by tZ and WtZ production.

6.1.1 VV and $t\bar{t}Z/\gamma^*$ backgrounds

The VV simulated event sample does not model the jet multiplicity spectrum in data well. Therefore, a data-driven correction is derived from an inclusive trilepton diboson-enriched region with zero $b^{85\%}$ jets. The events are required to have three leptons passing the (L, M, M) selection. The N_{jets}-dependent correction factors are derived using a fit to the ratio of $N_{\text{data}} - N_{\text{MC,non-}VV}$ to $N_{\text{MC},VV}$ as a function of N_{jets}. The corrections reach about 35% for $N_{\text{jets}} = 6$.

The 3ℓVV and 3ℓttZ CRs are used in the likelihood fit to data to improve the predicted background contributions from the VV and $t\bar{t}Z/\gamma^*$ processes, respectively. The numbers of jets and b-jets provide good discrimination between these two processes. Events in the 3ℓVV CR are required to have 2 or 3 jets, whereas events in the 3ℓttZ CR must have ≥ 4 jets. Additionally, the number of b-jets is fitted in the 3ℓttZ CR. The measured normalisation factors are $\lambda_{VV} = 0.87 \pm 0.33$ and $\lambda_{t\bar{t}Z} = 1.16 \pm 0.15$. The normalisation factor for $t\bar{t}Z$ controls the dominant contribution from $t\bar{t}Z$ in association with light-quark- and gluon-initiated jets. The $t\bar{t}Z$ contribution from events produced in association with heavy-quark-initiated jets is normalised to the theoretical cross-section and assigned a larger uncertainty as described in section 7.2.

Figures 2(a) and 2(b) show the total yield and b-jet multiplicity distribution in the 3ℓVV and 3ℓttZ CRs, respectively, before and after the likelihood fit described in section 8.1.

JHEP05(2024)131

6.1.2 Other irreducible backgrounds

The rate of background events from internal conversions (denoted as "Int Conv") with $m(e^+e^-) < 1$ GeV is estimated using two dedicated CRs: 3ℓIntC and 3ℓMatC. The main contributions to these background events originate from $t\bar{t}\gamma^*$ with $m(e^+e^-) < 1\,\text{GeV}$ and $Z \to \ell^+\ell^-\gamma^*(\to e^+e^-)$. The total yield in each category is used in the likelihood fit to determine the normalisation factor $\lambda_e^{\text{IntC}} = 1.07 \pm 0.24$, where the uncertainty is mainly statistical.

6.2 Reducible backgrounds

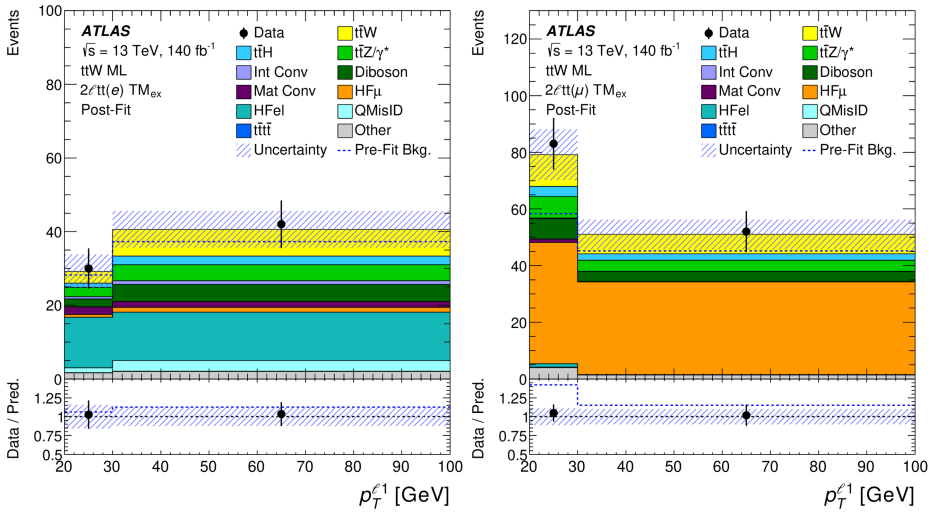
6.2.1 Non-prompt leptons

Non-prompt leptons originate from material conversions, heavy-flavour hadron decays, or the improper reconstruction of other particles, with a composition strongly depending on the lepton quality requirements and varying across event categories. These backgrounds are in general small in all 2ℓ and 3ℓ SRs and are estimated from simulation, with the normalisation determined by the likelihood fit. The main contribution to the non-prompt-lepton background is from $t\bar{t}$ production, followed by much smaller contributions from V+jets and single-top-quark processes. The non-prompt leptons in the simulated event samples are labelled according to whether they originate from HF or light-flavour (LF) hadron decays, or from a material conversion candidate. The HF category includes leptons from bottom and charm decays. The LF category is negligible in this analysis, and thus the non-prompt leptons from hadronic decays are dominated by HF non-prompt leptons.

Two corrections are applied to the $t\bar{t}$ and overall non-prompt-lepton background simulations before the fit. First, the $t\bar{t}$ + $\geq$1 b-jet contribution is multiplied by a factor of 1.3 as previously measured by ATLAS [109]. Second, the shape of the b-jet multiplicity distribution in the non-prompt-lepton background simulation is corrected to match data in an orthogonal 2ℓSS validation region enriched in non-prompt leptons, where one of the leptons must pass a looser non-prompt-lepton BDT score but not pass the M lepton WP.

Several of the event categories introduced in section 5 were designed to be enriched in specific processes and are used to derive normalisation factors to improve the modelling in the simulation. The 3ℓMatC CR is enriched in material conversions (denoted as "Mat Conv") and only the total event yield is used. There are six 2ℓ CRs enriched in contributions from HF non-prompt leptons in $t\bar{t}$ events, i.e. $2\ell\text{tt(e)}_{TM_{\text{ex}}}$, $2\ell\text{tt(e)}_{M_{\text{ex}}T}$, $2\ell\text{tt(e)}_{M_{\text{ex}}M_{\text{ex}}}$, $2\ell\text{tt}(\mu)_{TM_{\text{ex}}}$, $2\ell\text{tt}(\mu)_{M_{\text{ex}}T}$, and $2\ell\text{tt}(\mu)_{M_{\text{ex}}M_{\text{ex}}}$. In these CRs, the distribution of the transverse momentum $p_{\text{T}}^{\ell 1}$ of the sub-leading lepton is used. Requiring at least one M_{ex} lepton in these CR events provides separation from the processes with prompt leptons, especially $t\bar{t}W$, and thus optimises the sensitivity to the HF non-prompt electron and muon contributions. The $t\bar{t}W$ signal contribution in these control regions is at most 11% of the total expected yield. Normalisation factors for three non-prompt-lepton background contributions are estimated from the simultaneous likelihood fit to data. The normalisation factor for HF non-prompt leptons is estimated separately for electrons and muons, and is denoted by λ_e^{had} and λ_μ^{had} respectively. An additional normalisation factor λ_e^{MatC} is determined for the background from material conversions. The measured normalisation factors are $\lambda_e^{\text{had}} = 0.83 \pm 0.31$, $\lambda_\mu^{\text{had}} = 1.01 \pm 0.21$, and $\lambda_e^{\text{MatC}} = 1.15 \pm 0.31$, where the uncertainties are mainly statistical.

JHEP05(2024)131



(a) (b)

Figure 3. Comparison between data and the signal-plus-background prediction for the distribution of the transverse momentum of the sub-leading lepton ($p_{\mathrm{T}}^{\ell 1}$) in (a) the $2\ell\mathrm{tt(e)}_{TM_{\mathrm{ex}}}$ CR and (b) the $2\ell\mathrm{tt}(\mu)_{TM_{\mathrm{ex}}}$ CR. The signal and background contributions after the likelihood fit to data ("Post-Fit") under the signal-plus-background hypothesis are shown as filled histograms. The total signal-plus-background prediction before the likelihood fit to data ("Pre-Fit Bkg.") is shown as a dashed blue histogram in the upper panel. The ratio of the data to the total prediction ("Pred.") is shown in the lower panel, separately for the post-fit prediction (black points) and pre-fit background (dashed blue line). The combined statistical and systematic uncertainty in the prediction is indicated by the blue hatched band. The last bin in each figure contains the overflow.

Figures 3(a) and 3(b) display the $p_{\mathrm{T}}^{\ell 1}$ distribution in the $2\ell\mathrm{tt(e)}_{TM_{\mathrm{ex}}}$ and $2\ell\mathrm{tt}(\mu)_{TM_{\mathrm{ex}}}$ CRs after the likelihood fit to data. As shown in the figures, the purity of the HF non-prompt-lepton background is 43% and 61%, respectively, which was achieved when using the exclusive M_{ex} lepton working point.

6.2.2 Charge misassignment

Backgrounds due to leptons with an incorrectly assigned charge primarily affect the 2ℓ channel and arise mainly from $t\bar{t}$ production, with one electron either undergoing hard bremsstrahlung followed by an asymmetric conversion ($e^{\pm} \to e^{\pm}\gamma^{*} \to e^{\pm}e^{+}e^{-}$) or having mismeasured track curvature. The muon charge misassignment rate is negligible in the p_{T} range relevant to this analysis. The electron charge misassignment rate is measured in data by using samples of $Z \to e^{+}e^{-}$ events reconstructed as either same-charge pairs or opposite-charge pairs, with the non-Z background subtracted via a sideband method utilising events outside the Z boson mass window. The sideband region is defined by fitting a Gaussian function to the Z boson mass distribution and selecting events with $m(\ell\ell)$ more than one and less than four standard deviations from the fitted mean.

The charge misassignment rate is extracted from the ratio of the numbers of same-charge and opposite-charge events close to the Z-boson mass through a likelihood approach

JHEP05(2024)131

taking into account the possibility that both electron charges are misassigned. The rates are parameterised as a function of electron p_{T} and $|\eta|$, and vary from about 10^{-5} for low-p_{T} electrons ($17 \leq p_{\mathrm{T}} \leq 50$ GeV) with $|\eta| \leq 1.37$, to about 4×10^{-3} for high-p_{T} electrons ($p_{\mathrm{T}} \geq 100$ GeV) with $2 \leq |\eta| \leq 2.47$. To estimate the QMisID background in each of the corresponding event categories, the measured charge misassignment rate is applied to data events satisfying the requirements of the 2ℓ channels, except that the two leptons must have opposite charges.

7 Systematic uncertainties

Many sources of systematic uncertainty are considered for the cross-section measurements. These are grouped into three categories: instrumental uncertainties that affect physics object reconstruction; modelling uncertainties relevant for MC simulation-based estimations; and uncertainties affecting the estimation of misreconstructed-lepton backgrounds.

7.1 Instrumental uncertainties

Instrumental systematic uncertainties related to the trigger efficiency, lepton reconstruction and identification, jet calibration, b-tagging, and non-prompt-lepton BDT working point calibrations are considered in the analysis. Physics object reconstruction and calibration are provided together with a systematic uncertainty model for propagating the corresponding uncertainties to the analysis. The calibrations are applied either as an overall event reweighting, or scale factor, to correct the simulation to the data, or as a rescaling (smearing) of the object's energy or momentum scale (resolution) and come with associated uncertainties. The combined effect of these uncertainties is less than 10% in the inclusive measurement, but reaches approximately 18% in the higher jet-multiplicity bins of the differential measurement.

Uncertainties associated with the lepton selection arise from the trigger, reconstruction, identification and isolation efficiencies, and the lepton momentum scale and resolution [90, 91, 110, 111]. Uncertainties in the non-prompt-lepton BDT calibration are estimated through a $Z \to \ell\ell$ tag-and-probe method and cover uncertainties related to the $Z(\to \ell\ell)$+jets MC modelling, the template cut/shape, the $m_{\ell\ell}$ window, the tag-and-probe lepton selections, the multijet background, the non-prompt lepton background, the luminosity, the cross-sections of the considered processes, and the limited number of events in simulation and data. The combined effect of these uncertainties is approximately 2% in the inclusive measurement and typically less than 5% in the differential measurements.

Uncertainties associated with jet reconstruction and calibration arise from the jet energy scale (JES), the JVT requirement and the jet energy resolution (JER). The JES and its uncertainties are derived by combining information from test-beam data, collision data and simulation [97]. The JES and JER have 30 and 13 components, respectively, in the fit. The uncertainties in the JES, JER and JVT increase at lower jet p_{T}. The combined effect of these uncertainties is approximately 1.5% in the inclusive measurement, while in the differential measurements it is approximately 5% for intermediate jet multiplicities and rises to 12%–18% for low and high jet multiplicities.

The efficiency of the b-tagging algorithm is measured for each jet flavour using control samples in data and in simulation. From these measurements, correction factors are derived

JHEP05(2024)131

to correct the tagging rates in the simulation. For b-jets, the correction factors and their uncertainties are estimated from data using dileptonic $t\bar{t}$ events [100, 102]. For c-jets, they are derived from jets arising from W boson decays in $t\bar{t}$ events [103]. For light-flavour jets, the correction factors are derived from dijet events [104]. Uncertainties from sources affecting the b- and c-tagging efficiencies are evaluated as a function of jet p_{T}, including bin-to-bin correlations. The uncertainties in the efficiency for tagging light-flavour jets depend on the jet p_{T} and $|\eta|$. An additional uncertainty is assigned to account for the extrapolation of the b-tagging efficiency measurement from the p_{T} region used to determine the correction factors to regions with higher p_{T}. The combined effect of these uncertainties is approximately 0.2% in the inclusive measurement, whereas in the differential measurements, it is approximately 3% in the intermediate b-jet multiplicity bins and rises to 10%–18% for lower and higher b-jet multiplicities.

The uncertainty in the reweighting of the MC pile-up distribution to match the distribution in data is evaluated by varying the reweighting factors and has a very small impact on either the inclusive or differential results.

The uncertainty in the combined 2015–2018 integrated luminosity is 0.83% [112], obtained using the LUCID-2 detector [113] for the primary luminosity measurements, complemented by measurements using the inner detector and calorimeters.

7.2 MC modelling uncertainties

Systematic uncertainties in the $t\bar{t}W$ MC predictions due to missing higher-order QCD corrections in the modelling are estimated by doubling and halving the factorisation and renormalisation scales chosen for the nominal sample. To estimate the uncertainty due to ambiguities in the ME and PS algorithm and parameter choices, the nominal Sherpa prediction is compared with the prediction of the MadGraph5+Pythia 8 FxFx sample described in section 3. In addition, a dedicated parton shower model uncertainty is estimated as the relative difference between the Powheg+Pythia 8 and Powheg+Herwig 7 predictions and applied to the nominal $t\bar{t}W$ prediction. Uncertainties in the PDF modelling are included by varying the value of α_{s} and using different PDF sets. The $t\bar{t}W$ modelling uncertainty is one of the largest uncertainties in the analysis and leads to a combined impact (summing each contribution in quadrature) of 6% in the inclusive measurement and, depending on the bin, 10%–20% in the differential measurement.

The uncertainty in $t\bar{t}H$ modelling due to the initial-state radiation (ISR) is estimated using weights in the matrix element calculation and the parton shower. The factorisation and renormalisation scales are varied, and ISR α_{s} variations are taken from the A14 tune. Additionally, uncertainties in the ME (PS algorithm — parton shower, hadronisation and underlying-event modelling) are estimated by comparing the nominal Powheg+Pythia 8 MC simulation with MadGraph5+Pythia 8 (Powheg+Herwig 7).

Uncertainties due to missing higher orders in QCD are estimated for $t\bar{t}Z$ production by varying the nominal factorisation and renormalisation scales by factors of 0.5 and 2.0. Uncertainties in additional-jet modelling are estimated with ISR α_{s} variations taken from the A14 tune. Parton shower, hadronisation and underlying-event modelling uncertainties

JHEP05(2024)131

are estimated by comparing the nominal MadGraph5+Pythia 8 MC simulation with MadGraph5+Herwig 7.

Uncertainties in VV modelling due to missing higher orders in QCD are estimated by varying the nominal factorisation and renormalisation scales by factors of 0.5 and 2.0. In addition, systematic uncertainties associated with the data-driven N_{jets}-dependent correction factors applied to VV production are derived from the fit function parameter uncertainties.

Alternative $t\bar{t}$ MC samples are used for shower uncertainties in the HF non-prompt-lepton background estimate and for uncertainties in the extrapolation from the CRs to the SRs. For this, the Powheg+Herwig 7.1.3 and Sherpa 2.2.10 samples are used.

The uncertainties in higher-order cross-sections are taken into account by using the values given in section 3 for all background processes except those whose normalisation is measured in the fit. In the $t\bar{t}Z$ MC sample, the component containing additional heavy-quark-initiated jets is normalised to the theoretical prediction and assigned a 50% uncertainty.

7.3 Non-prompt-lepton background modelling uncertainties

For the estimation of non-prompt-lepton backgrounds from HF decays and conversions, the following uncertainties are taken into account.

Uncertainties are estimated for the modelling of the non-prompt-lepton BDT input variables, namely the muon's energy deposit in the calorimeter relative to the expected value ($E_{\text{cluster}}/E_{\text{expected}}$), the electron track p_{T} divided by the jet track p_{T}, and the secondary vertex's longitudinal significance, using tracks with $p_{\text{T}} > 500\,\text{MeV}$ for non-prompt muons. These uncertainties are included as variations that can affect the shape of distributions in each region, but not their normalisation.

Extrapolation uncertainties in the non-prompt-lepton background yields are derived to account for non-prompt-lepton rate differences between the *Tight-not-VeryTight* and *VeryTight* non-prompt-lepton BDT working points. These uncertainties are obtained by comparing the non-prompt-lepton efficiencies in the nominal $t\bar{t}$ simulation with those in an alternative $t\bar{t}$ simulation as a function of lepton p_{T} and separately for electrons and muons. A constant uncertainty of 20% is estimated for electrons and muons.

Uncertainties in the $t\bar{t}$ parton shower are assessed by using the Powheg+Herwig 7 $t\bar{t}$ MC simulation as a variation of the nominal Powheg+Pythia 8 prediction, separately for the electron and muon channels.

Uncertainties in the modelling of $t\bar{t}$ production in association with heavy-flavour jets are accounted for by assigning an uncorrelated 50% uncertainty to the $t\bar{t}+b$ and $t\bar{t}+c$ background processes.

Uncertainties in the electron conversion background extrapolation from Z-enriched to $t\bar{t}$-enriched regions are derived from the residual data/simulation mismodelling in dedicated 2ℓ validation regions with two tight same-sign leptons, requiring one of them to be a conversion candidate. Internal and material conversion extrapolation uncertainties of 50% and 10%, respectively, are applied.

A systematic uncertainty of 10%–60% is assigned to the background from electrons with misidentified charge. The uncertainty increases with electron p_{T} and decreases with $|\eta|$. The uncertainty is assessed by combining the uncertainties in the measurement of the charge

JHEP05(2024)131

misassignment rate, the changes in the rate when varying the m_Z window selection, and the different rates measured in data and $Z \to e^+e^-$ simulation.

8 Results

A maximum-likelihood fit to all bins in the SRs and the 10 CRs (see tables 4 and 5) is performed to simultaneously determine the background and the $t\bar{t}W$ signal yields that are most consistent with the data. In the six HF non-prompt electron and muon CRs ($2\ell\text{tt(e)}_{TM_{\text{ex}}}$, $2\ell\text{tt(e)}_{M_{\text{ex}}T}$, $2\ell\text{tt(e)}_{M_{\text{ex}}M_{\text{ex}}}$, $2\ell\text{tt}(\mu)_{TM_{\text{ex}}}$, $2\ell\text{tt}(\mu)_{M_{\text{ex}}T}$, $2\ell\text{tt}(\mu)_{M_{\text{ex}}M_{\text{ex}}}$), the sub-leading lepton's transverse momentum ($p_{\text{T}}^{\ell 1}$) distribution is used, whereas in the two conversion CRs (3ℓIntC, 3ℓMatC) and the 3ℓVV CR, the total event yield (i.e. a single bin) is used. In the 3ℓttZ CR, the b-jet multiplicity is fitted.

For the inclusive $t\bar{t}W$ cross-section measurement, the event yields in 56 SR bins (48 for 2ℓSS and 8 for 3ℓ) are fitted to data together with the CRs, and the results are shown in section 8.1. For the differential $t\bar{t}W$ cross-section measurement, various distributions in eight SRs (two 2ℓSS and six 3ℓ signal region categories) are fitted to data along with the same CRs used in the inclusive measurement. The corresponding results are shown in section 8.2.

8.1 Inclusive cross-section measurement

The $t\bar{t}W$ cross-section is measured inclusively and for the fiducial regions defined in section 5. The total event yields in the signal categories described in table 4 are fitted simultaneously with the control regions to data. The likelihood function $\mathcal{L}(\mu, \vec{\lambda}, \vec{\theta})$ is constructed as a product of Poisson probability terms over all bins considered in the measurement, and depends on the following: the signal-strength parameter, μ, defined as a multiplicative factor applied to the predicted yield for the $t\bar{t}W$ signal; $\vec{\lambda}$, the normalisation factors for several backgrounds (see section 6); and $\vec{\theta}$, a set of nuisance parameters (NP) encoding systematic uncertainties in the signal and background expectations [114]. Systematic uncertainties can impact the estimated signal and background rates, the migration of events between categories, and the shape of the fitted distributions; they are summarised in section 7. Both μ and $\vec{\lambda}$ are treated as free parameters in the likelihood fit. The NPs $\vec{\theta}$ allow variations of the expectations for signal and background according to the systematic uncertainties, subject to Gaussian constraints in the likelihood fit. Their fitted values represent the deviations from the nominal expectations that are needed to provide the best fit to the data. Statistical uncertainties in each bin due to the limited size of the simulated event samples are taken into account with dedicated parameters, using the Beeston-Barlow "lite" technique [115].

The observed and expected yields in the 10 CRs and the 56 SRs after the combined likelihood fit under the signal-plus-background hypothesis are compared in figures 4 and 5. The corresponding post-fit yields for the SRs and CRs are shown in tables 7, 8, and 9. There are no significant deviations from the predictions after the fit to data.

The best-fit value of the $t\bar{t}W$ cross-section, $\sigma(t\bar{t}W)$, is:

$$\sigma(t\bar{t}W) = 880 \pm 50\,(\text{stat.}) \pm 70\,(\text{syst.}) = 880 \pm 80\ \text{fb}.$$

It is compatible with the SM NNLO cross-section of $745 \pm 50\,(\text{scale}) \pm 13\,(\text{2-loop approx.}) \pm 19\,(\text{PDF}, \alpha_{\text{s}})$ fb from ref. [15] at the level of 1.4σ. It is also compatible with the SM cross-

JHEP05(2024)131

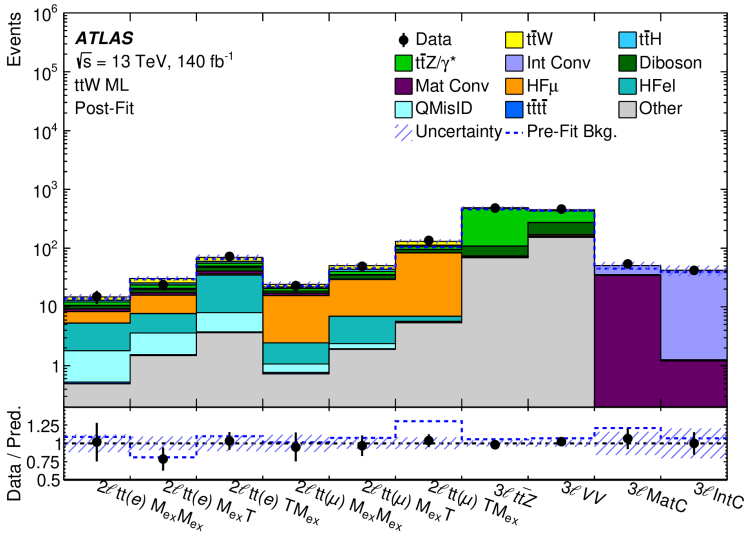


Figure 4. Comparison between data and the signal-plus-background prediction for the event yields in the ten control region categories. The signal and background contributions after the likelihood fit to data ("Post-Fit") under the signal-plus-background hypothesis are shown as filled histograms. The total signal-plus-background prediction before the likelihood fit to data ("Pre-Fit Bkg.") is shown as a dashed blue histogram in the upper panel. The ratio of the data to the total prediction ("Pred.") is shown in the lower panel, separately for the post-fit prediction (black points) and pre-fit background (dashed blue line). The combined statistical and systematic uncertainty in the prediction is indicated by the blue hatched band.

section of $722\,^{+70}_{-78}(\text{scale}) \pm 7\,(\text{PDF})$ fb from ref. [27] at the level of 1.5σ. The systematic uncertainty, 7.9%, is somewhat larger than the 5.8% reported by CMS in ref. [9]. However, the systematic uncertainty would decrease to 5.6% if uncertainties related to algorithmic choices in the $t\bar{t}W$ ME generator and PS, which are not considered in the CMS measurement, were removed. This modified version of the measurement does not include ISR/FSR and colour reconnection $t\bar{t}W$ uncertainties, which are considered in the CMS measurement and amount to 0.8% and 1%, respectively.

The fiducial $t\bar{t}W$ cross-section, $\sigma_{\text{fid}}(t\bar{t}W)$, based on the selection defined in section 5, is also measured. The fit to data is set up identically to the inclusive cross-section measurement but with modified systematic uncertainties to remove fiducial acceptance effects. The measured value is:

$$\sigma_{\text{fid}}(t\bar{t}W) = 20.9 \pm 1.1\,(\text{stat.}) \pm 1.9\,(\text{syst.}) = 20.9 \pm 2.2 \text{ fb}.$$

The relative uncertainty in the fiducial cross-section measurement is slightly larger than that of the inclusive measurement, which is contrary to what might usually be expected. This is due to significant differences in detector-level event reconstruction efficiency between the Sherpa and MadGraph5+Pythia 8 FxFx $t\bar{t}W$ generator models. There are also differences in fiducial acceptance between the two generators, but with opposite impact. Therefore, the two effects partially cancel out in the inclusive fit, but the efficiency difference shows its full effect in the fiducial fit.

JHEP05(2024)131

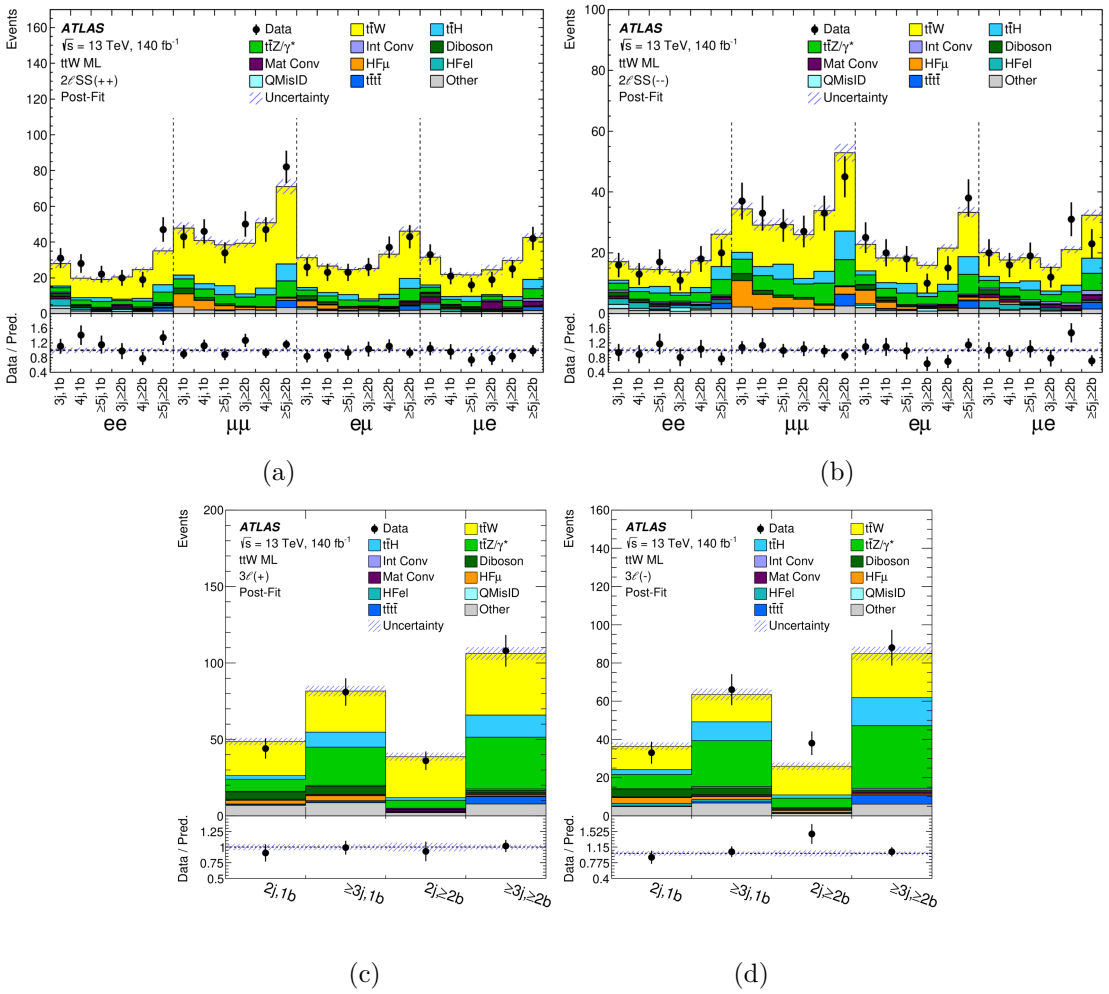


Figure 5. Comparison between data and the signal-plus-background prediction for the event yields in the (a) 2ℓSS++, (b) 2ℓSS−−, (c) $3\ell+$ and (d) $3\ell-$ signal region categories. The signal and background contributions after the likelihood fit to data ("Post-Fit") under the signal-plus-background hypothesis are shown as filled histograms. The ratio of the data to the total post-fit prediction ("Pred.") is shown in the lower panel. The combined statistical and systematic uncertainty in the prediction is indicated by the blue hatched band.

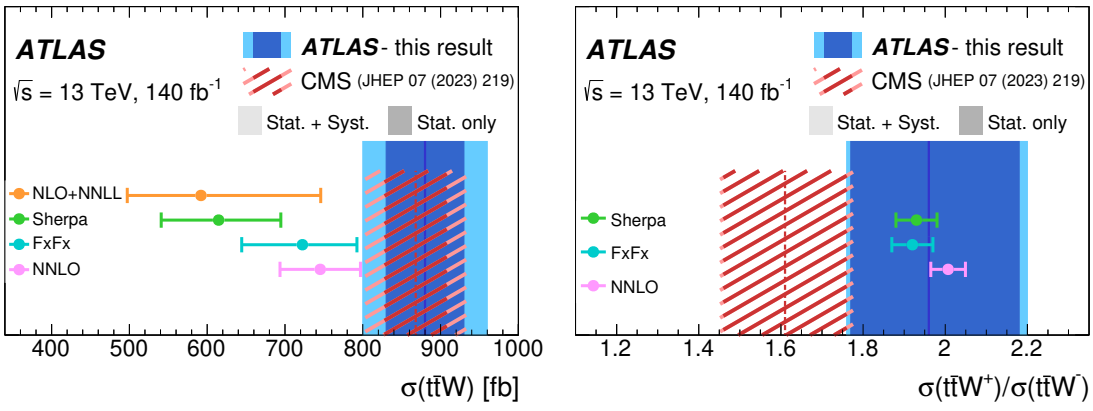
Figure 6(a) compares the measured $t\bar{t}W$ cross-section with theory predictions from Sherpa (as described in section 3), the MadGraph5+Pythia 8 FxFx prescription including EWK corrections from ref. [27], the NLO+NNLL calculation in ref. [20], and the NNLO calculation in ref. [15]. The measurement from CMS [9] is also shown. The measured inclusive cross-section is larger than the theoretical predictions, and is compatible with the measurement from CMS.

Additional measurements are performed using the same analysis model, but measuring the cross-sections of $\sigma(t\bar{t}W^+)$ and $\sigma(t\bar{t}W^-)$ simultaneously. Splitting the measurement by W boson charge is interesting because a strong charge asymmetry is expected due to the associated asymmetry in the valence quark PDF, and this feature is often used to separate $t\bar{t}W$ production from other processes with similar final states, such as $t\bar{t}H$ and $t\bar{t}t\bar{t}$ production.

JHEP05(2024)131

	$\ell^-\ell^-$ SR	$\ell^+\ell^+$ SR	$\ell^+\ell^-\ell^-$ SR	$\ell^-\ell^+\ell^+$ SR
$t\bar{t}W$	261 ± 18	468 ± 30	64 ± 6	115 ± 10
$t\bar{t}H$	66 ± 9	65 ± 9	29 ± 4	28 ± 4
$t\bar{t}Z/\gamma^*$	95 ± 9	100 ± 10	69 ± 8	71 ± 8
Int Conv	9 ± 5	9 ± 5	2.5 ± 1.4	2.5 ± 1.4
Diboson	16 ± 5	22 ± 7	9.1 ± 2.7	12 ± 4
Mat Conv	11.2 ± 3.3	19 ± 5	2.5 ± 0.8	3.9 ± 1.1
HF(μ)	35 ± 11	30 ± 10	6.1 ± 2.5	6.6 ± 2.6
HF(e)	14 ± 6	15 ± 6	2.9 ± 1.3	2.0 ± 0.8
QMisID	8.2 ± 2.7	8.2 ± 2.7	0.69 ± 0.15	0.66 ± 0.13
$t\bar{t}t\bar{t}$	12 ± 9	12 ± 9	5 ± 4	5 ± 4
Other	32 ± 5	42 ± 6	18.5 ± 3.1	25.0 ± 3.3
Total	559 ± 14	788 ± 23	209 ± 7	273 ± 9
Data	546	803	225	269

Table 7. Summary of observed and predicted yields in the four signal region categories. The background prediction is shown after the combined likelihood fit to data under the signal-plus-background hypothesis across all control region and signal region categories. The quoted uncertainties consider all statistical and systematic uncertainties after the fit to data. The uncertainty on the total yield can be smaller than the quadratic sum of uncertainties of the individual contributions due to the anti-correlations resulting from the likelihood fit.



(a) (b)

Figure 6. Comparison of (a) the measured inclusive $t\bar{t}W$ cross-section and (b) the $t\bar{t}W^+/t\bar{t}W^-$ cross-section ratio with theoretical predictions from Sherpa, the MadGraph5+Pythia 8 FxFx prescription including EWK corrections from ref. [27], the NLO+NNLL calculation from ref. [20], and the NNLO calculation from ref. [15], and also the measurement from CMS [9]. The theoretical uncertainty in $t\bar{t}W^+/t\bar{t}W^-$ is calculated assuming scale variations are fully correlated between $t\bar{t}W^+$ and $t\bar{t}W^-$.

JHEP05(2024)131

	$2\ell\mathbf{tt(e)}_{M_{\text{ex}}M_{\text{ex}}}$	$2\ell\mathbf{tt(e)}_{M_{\text{ex}}T}$	$2\ell\mathbf{tt(e)}_{TM_{\text{ex}}}$	$2\ell\mathbf{tt}(\mu)_{M_{\text{ex}}M_{\text{ex}}}$	$2\ell\mathbf{tt}(\mu)_{M_{\text{ex}}T}$	$2\ell\mathbf{tt}(\mu)_{TM_{\text{ex}}}$
$t\bar{t}W$	1.8 ± 0.5	5.1 ± 0.5	10.4 ± 1.4	2.4 ± 0.7	7.3 ± 1.2	17.9 ± 2.5
$t\bar{t}H$	0.79 ± 0.19	1.73 ± 0.32	3.5 ± 0.6	1.11 ± 0.21	2.8 ± 0.5	5.8 ± 1.0
$t\bar{t}Z/\gamma^*$	1.49 ± 0.19	3.2 ± 0.4	6.8 ± 0.7	2.07 ± 0.29	5.2 ± 0.6	11.4 ± 1.4
Int Conv	0.18 ± 0.12	0.9 ± 0.5	1.6 ± 0.9	0.11 ± 0.07	0.54 ± 0.32	0.27 ± 0.16
Diboson	1.2 ± 0.3	2.3 ± 0.6	6.8 ± 1.4	1.4 ± 0.4	5 ± 1	10.6 ± 2.2
Mat Conv	0.95 ± 0.31	1.5 ± 1.3	3.7 ± 1.7	1.5 ± 0.5	1.0 ± 0.4	1.3 ± 0.8
HF(μ)	3.0 ± 0.8	8.1 ± 1.6	1.9 ± 0.9	13.1 ± 2.5	22 ± 4	75 ± 11
HF(e)	3.5 ± 1.0	4.1 ± 1.2	27 ± 9	1.4 ± 0.5	4.5 ± 1.5	1.3 ± 0.9
QMisID	1.3 ± 0.8	2.0 ± 1.4	4.2 ± 2.1	0.31 ± 0.2	0.43 ± 0.35	0.21 ± 0.09
$t\bar{t}t\bar{t}$	0.033 ± 0.027	0.035 ± 0.029	0.07 ± 0.06	0.039 ± 0.032	0.07 ± 0.05	0.11 ± 0.09
Other	0.49 ± 0.07	1.49 ± 0.17	3.7 ± 0.4	0.72 ± 0.09	1.88 ± 0.17	5.3 ± 0.8
Total	14.6 ± 1.8	30.4 ± 2.8	69 ± 7	24.0 ± 2.8	50 ± 4	129 ± 11
Data	15	24	72	23	49	135

Table 8. Summary of observed and predicted yields in the 2ℓSS control region categories. The background prediction is shown after the combined likelihood fit to data under the signal-plus-background hypothesis across all control region and signal region categories. The quoted uncertainties consider all statistical and systematic uncertainties after the fit to data. The uncertainty on the total yield can be smaller than the quadratic sum of uncertainties of the individual contributions due to the anti-correlations resulting from the likelihood fit.

	$3\ell\mathbf{IntC}$	$3\ell\mathbf{MatC}$	$3\ell\mathbf{ttZ}$	$3\ell\mathbf{VV}$
$t\bar{t}W$	—	—	7.2 ± 0.8	13.0 ± 0.9
$t\bar{t}H$	—	—	10.0 ± 1.5	4.3 ± 0.6
$t\bar{t}Z/\gamma^*$	—	—	360 ± 40	160 ± 23
Int Conv	41 ± 9	15 ± 4	0.055 ± 0.032	0.41 ± 0.25
Diboson	0.035 ± 0.020	0.88 ± 0.20	35 ± 11	100 ± 28
Mat Conv	1.2 ± 0.9	34 ± 9	0.48 ± 0.30	2.1 ± 0.7
HF(μ)	—	—	1.19 ± 0.35	8.4 ± 2.7
HF(e)	—	—	0.40 ± 0.22	7.1 ± 2.4
QMisID	—	—	0.19 ± 0.13	0.8 ± 0.4
$t\bar{t}t\bar{t}$	—	—	1.7 ± 1.3	0.05 ± 0.04
Other	—	—	68 ± 19	151 ± 20
Total	42 ± 9	50 ± 8	487 ± 21	446 ± 20
Data	42	54	482	460

Table 9. Summary of observed and predicted yields in the 3ℓ control region categories. The background prediction is shown after the combined likelihood fit to data under the signal-plus-background hypothesis across all control region and signal region categories.

JHEP05(2024)131

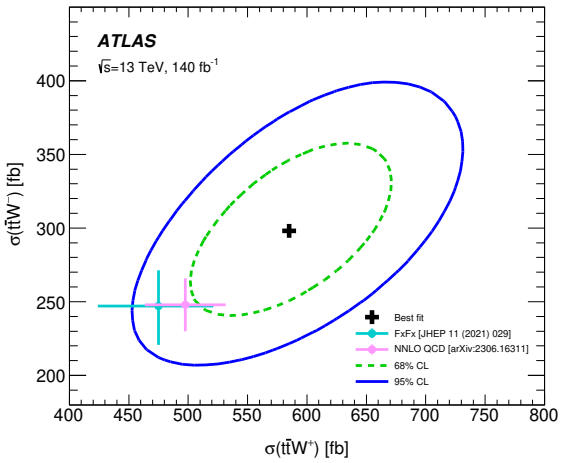


Figure 7. Two-dimensional likelihood scan of the $t\bar{t}W^+$ and $t\bar{t}W^-$ cross-sections. The black cross indicates the best-fit point and the green and lilac markers show the SM predictions from refs. [27] and [15], respectively. The blue dashed and solid lines correspond to the 68% and 95% confidence interval contours, respectively.

The following values were measured:

$$\begin{aligned}\sigma(t\bar{t}W^+) &= 583 \pm 34\,(\text{stat.}) \pm 47\,(\text{syst.}) = 583 \pm 58\ \text{fb},\\ \sigma(t\bar{t}W^-) &= 296 \pm 28\,(\text{stat.}) \pm 29\,(\text{syst.}) = 296 \pm 40\ \text{fb}.\end{aligned} \tag{8.1}$$

The ratio of the cross-sections is extracted with another fit configuration that depends on $\mu(R)$, defined as a multiplicative factor applied to the ratio $R(t\bar{t}W) = \sigma(t\bar{t}W^+)/\sigma(t\bar{t}W^-)$ evaluated using eq. (8.1). The resulting measurement of $R(t\bar{t}W)$ is:

$$R(t\bar{t}W) = 1.96 \pm 0.21\,(\text{stat.}) \pm 0.09\,(\text{syst.}) = 1.96 \pm 0.22.$$

Figure 6(b) compares the measured charge ratio with theoretical predictions and the measurement from CMS. The measured value is in good agreement with the theoretical prediction of $R(t\bar{t}W) = 2.007 \pm 2.1\%\,(\text{scale}) \pm 1.7\%$ (PDF) from ref. [15], as well as those of $R(t\bar{t}W) = 1.93 \pm 0.02\,(\text{scale}) \pm 0.04$ (PDF) from Sherpa (as described in section 3) and $R(t\bar{t}W) = 1.92 \pm 0.02\,(\text{scale}) \pm 0.04$ (PDF) from the MadGraph5+Pythia 8 FxFx prescription including EWK corrections from ref. [27]. This measurement yields a value higher than the one measured by CMS, but each measurement's uncertainty has a large statistical component.

Figure 7 shows a two-dimensional likelihood scan of the fitted values of $t\bar{t}W^+$ and $t\bar{t}W^-$ compared to the SM prediction. There is a 58% correlation between the $t\bar{t}W^+$ and $t\bar{t}W^-$ measurements.

The parameter of interest can also be defined to be the relative charge asymmetry, $A_{\text{C}}^{\text{rel}}$, defined as:

$$A_{\text{C}}^{\text{rel}} = \frac{\sigma(t\bar{t}W^+) - \sigma(t\bar{t}W^-)}{\sigma(t\bar{t}W^+) + \sigma(t\bar{t}W^-)}.$$

JHEP05(2024)131

The measured value resulting from the best fit to data is:

$$A_{\mathrm{C}}^{\mathrm{rel}} = 0.33 \pm 0.05\,(\mathrm{stat.}) \pm 0.02\,(\mathrm{syst.}) = 0.33 \pm 0.05.$$

This value is in good agreement with the theoretical prediction of $0.322 \pm 0.003\,(\mathrm{scale}) \pm 0.007\,(\mathrm{PDF})$ from Sherpa.

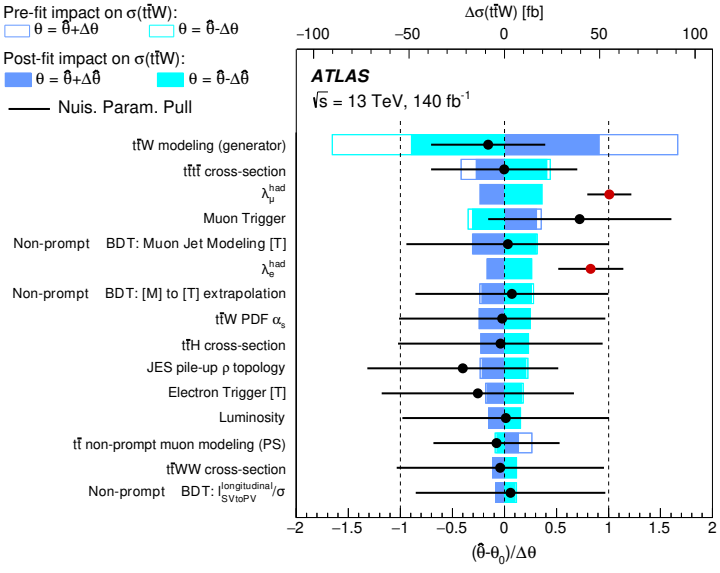
The contributions from the different sources of uncertainty affecting the measured cross-section are shown grouped by categories in table 10, and with the breakdown for each individual nuisance parameter in figure 8. The most important systematic uncertainties arising from theoretical predictions are in the modelling of the $t\bar{t}W$ signal, followed by the uncertainty in the prompt-lepton background normalisation, where the theoretical uncertainties in the $t\bar{t}H$ and $t\bar{t}t\bar{t}$ production normalisations are dominant. The leading instrumental systematic uncertainties originate from the b-tagging efficiency and the non-prompt-lepton BDT's prompt-lepton efficiency.

JHEP05(2024)131

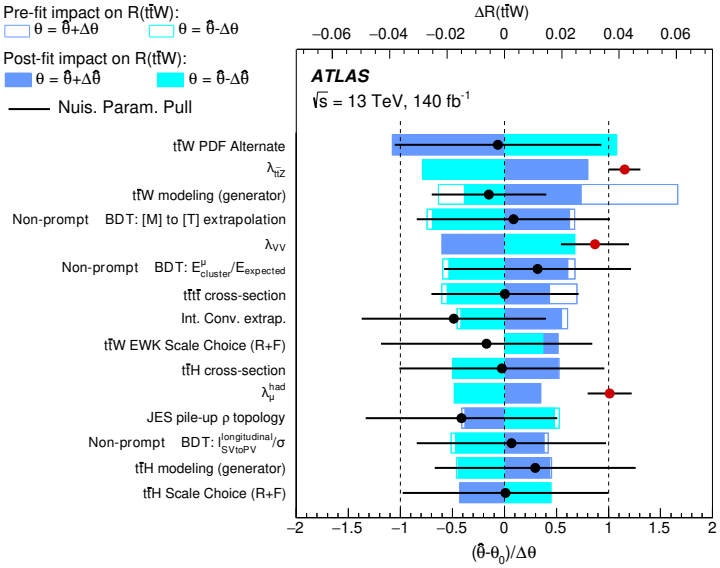
	$\frac{\Delta\sigma(t\bar{t}W)}{\sigma(t\bar{t}W)}$ [%]	$\frac{\Delta\sigma_{\mathbf{fid}}(t\bar{t}W)}{\sigma_{\mathbf{fid}}(t\bar{t}W)}$ [%]	$\frac{\Delta R(t\bar{t}W)}{R(t\bar{t}W)}$ [%]	$\frac{\Delta A_{\mathrm{C}}^{\mathrm{rel}}}{A_{\mathrm{C}}^{\mathrm{rel}}}$ [%]
$t\bar{t}W$ ME modelling	6.0	7.0	0.9	1.3
Prompt-lepton bkg. norm.	3.1	3.1	1.6	2.1
Lepton isolation BDT	2.3	2.3	0.7	1.0
Fakes/VV/$t\bar{t}Z$ norm. (free to vary)	2.3	2.5	1.7	2.4
Non-prompt-lepton bkg. modelling	2.0	2.0	2.4	3.2
Trigger	1.9	1.9	0.5	0.6
MC statistics	1.5	1.6	1.9	2.6
$t\bar{t}W$ PDF	1.5	1.5	2.1	2.8
Jet energy scale	1.3	1.4	1.2	1.7
Prompt-lepton bkg. modelling	1.3	1.3	1.2	1.7
Luminosity	0.9	0.9	0.1	<0.10
Charge Mis-ID	0.7	0.7	0.4	0.6
Jet energy resolution	0.5	0.5	0.6	0.9
Flavour tagging	0.4	0.5	0.5	0.6
$t\bar{t}W$ PS modelling	0.4	0.4	0.29	0.4
$t\bar{t}W$ scale	0.24	<0.10	0.29	0.29
Electron/photon reconstruction	0.21	0.22	0.11	0.13
Muon	0.15	0.17	<0.10	0.2
$E_{\mathrm{T}}^{\mathrm{miss}}$	<0.10	<0.10	0.15	0.21
Pile-up	<0.10	0.11	<0.10	<0.10
Total systematic uncertainty	8	9	5	7
Statistical uncertainty	5	5	10	14
Total	9	11	11	15

Table 10. The impact of the main sources of uncertainty on the measured quantities. The impact of each uncertainty on $\sigma(t\bar{t}W)$ is assessed by fixing the relevant fit parameters for a given uncertainty and re-fitting to data. The reduction in the total uncertainty in this modified fit gives the quoted impact. Different individual components used in the fit are combined into categories. The leading contributions to the prompt-lepton background normalisation uncertainty are the $t\bar{t}H$ and $t\bar{t}t\bar{t}$ normalisation uncertainties. In the fourth row, "Fakes" stands for non-prompt leptons.

JHEP05(2024)131



(a)



(b)

Figure 8. Ranking of the nuisance parameters and background normalisation factors included in the fit according to their impact on (a) the $t\bar{t}W$ cross-section, $\sigma(t\bar{t}W)$, and (b) $R(t\bar{t}W)$. In both (a) and (b), only the 15 nuisance parameters with the largest impacts are shown. The empty (solid) blue rectangles illustrate the pre-fit (post-fit) impacts on the parameter of interest, $\sigma(t\bar{t}W)$ in (a) and $R(t\bar{t}W)$ in (b), corresponding to the top axis. The pre-fit (post-fit) impact of each nuisance parameter, $\Delta\sigma(t\bar{t}W)$ in (a) and $\Delta R(t\bar{t}W)$ in (b), is calculated as the difference in the fitted value of (a) $\sigma(t\bar{t}W)$ or (b) $R(t\bar{t}W)$ between the nominal fit and the fit when fixing the corresponding nuisance parameter to $\hat{\boldsymbol{\theta}} \pm \boldsymbol{\Delta\theta}$ ($\hat{\boldsymbol{\theta}} \pm \boldsymbol{\Delta\hat{\theta}}$), where $\hat{\boldsymbol{\theta}}$ is the best-fit value of the nuisance parameter and $\boldsymbol{\Delta\theta}$ ($\boldsymbol{\Delta\hat{\theta}}$) is its pre-fit (post-fit) uncertainty. The black points show the pulls of the nuisance parameters relative to zero, $\boldsymbol{\theta}_0 = 0$. These pulls and their relative post-fit errors, $\boldsymbol{\Delta\hat{\theta}}/\boldsymbol{\Delta\theta}$, refer to the bottom axis. The background normalisation factors λ (red points) are pulled relative to one, $\boldsymbol{\theta}_0 = 1$. The fitted values and their post-fit errors refer to the bottom axis. The systematic uncertainties with "[T]" affect only the "tight" leptons.

JHEP05(2024)131

Variable	Definition
N_{jets}	Number of selected jets with $p_{\text{T}} > 25\,\text{GeV}$ and $\lvert\eta\rvert < 2.5$
$H_{\text{T}}^{\text{jet}}$	Scalar sum of the transverse momenta of selected jets with $p_{\text{T}} > 25\,\text{GeV}$ and $\lvert\eta\rvert < 2.5$
$H_{\text{T}}^{\text{lep}}$	Scalar sum of the transverse momenta of selected leptons
$\Delta R_{\ell b,\,\text{lead}}$	Angular separation between the leading lepton and the leading b-tagged jet
$\lvert\Delta\phi_{\ell\ell,\,\text{SS}}\rvert$	Absolute azimuthal separation between the two leptons of the same-sign pair
$\lvert\Delta\eta_{\ell\ell,\,\text{SS}}\rvert$	Absolute pseudorapidity separation between the two leptons of the same-sign pair

Table 11. Definition of observables measured.

8.2 Differential cross-section measurement

The differential $t\bar{t}W$ measurements were made as a function of six different observables. The chosen observables were selected because they have either an experimental motivation (e.g. variables where modelling discrepancies were observed before) or a theoretical motivation (e.g. variables that have significant distribution shape changes due to NLO corrections). The full set of measured observables is given in table 11.

A profile likelihood unfolding procedure [116] (PLU) is used to measure particle-level differential cross-sections for one observable at a time in the fiducial phase space defined in section 5. A likelihood model is built for a detector-level distribution by treating the contribution from each generator-level bin as a subcomponent of the detector-level signal. The likelihood takes the following form:

$$\mathcal{L}(\sigma, \vec{\theta}, \vec{\lambda}) = \prod_i P\left(N_i | L_{\text{int}} \sum_j \mathcal{R}_{ij}(\vec{\theta})\sigma_j(\vec{\theta}) + B_i(\vec{\theta}, \vec{\lambda})\right) \times \prod_k G(\theta_k) \times \prod_l R(\sigma_l, \tau_l),$$

where P and G are probability density functions of the Poisson and Gaussian distributions, respectively. The index i indicates the detector-level bin, j indicates the particle-level bin index and k the systematic uncertainty index. The variable N_i is the number of observed data events in detector-level bin i, L_{int} is the integrated luminosity, $\mathcal{R}_{ij}$ is the (i, j) bin of the response matrix, σ_j is the unfolded cross-section in particle-level bin j, and B_i is the number of background events in detector-level bin i, which depends on both $\vec{\lambda}$, the ratios of the measured background yields to the predicted values, and $\vec{\theta}$, the systematic-uncertainty nuisance parameters. The regularisation term, R, is controlled via the τ_l parameter that determines the level of regularisation used in the unfolding of generator-level bin l, where $l = 2, \ldots, N_{\text{bins}} - 1$. In practice, the value of σ_j is extracted by fitting for the number of events in particle-level bin j in each fiducial region, given by $N_j = L_{\text{int}}\sigma_j$ with $\sigma_j = \mu_j\sigma_j^{\text{MC}}$, and it is the signal strengths μ_j that vary in the fit. For a given observable and fiducial region, the value of τ_l is common to all l bins and is shown in table 12.

The response matrix is defined as:

$$\mathcal{R}_{ij} = \frac{1}{\alpha_i}\epsilon_j\mathcal{M}_{ij}.$$

JHEP05(2024)131

Observable	2ℓSS++	$3\ell+$	2ℓSS−−	$3\ell-$
N_{jets}	0.7	0.3	0.4	0.2
$H_{\text{T}}^{\text{jet}}$	0.6	0.3	0.4	0.2
$H_{\text{T}}^{\text{lep}}$	0.5	0.1	0.2	0.1
$\Delta R_{\ell b,\,\text{lead}}$	0.3	0.2	0.3	0.3
$\lvert\Delta\phi_{\ell\ell,\,\text{SS}}\rvert$	0.1	0	0	0
$\lvert\Delta\eta_{\ell\ell,\,\text{SS}}\rvert$	0.1	0.1	0.1	0

Table 12. Choice of regularisation parameter τ used for each observable and region.

The migration matrix, $\mathcal{M}_{ij}$, which quantifies the bin-to-bin migrations of events owing to resolution effects when going from particle level to detector level, is defined as:

$$\mathcal{M}_{ij} = \frac{N_{ij}^{\text{det.}\cap\text{fid.}}}{N_{j}^{\text{det.}\cap\text{fid.}}}.$$

The superscript det. ∩ fid. indicates events that pass both the detector-level event selection and the fiducial selection. The numerator $N_{ij}^{\text{det.}\cap\text{fid.}}$ is the expected number of detector-level events in detector-level bin i and particle-level bin j, while the denominator $N_{j}^{\text{det.}\cap\text{fid.}}$ is the expected number of detector-level events in particle-level bin j summed over all detector-level bins.

The migration matrix is then corrected with acceptance factors, α_i, which define the fraction of events that satisfy the detector-level selection and originate from configurations outside the particle-level fiducial selection:

$$\alpha_i = \frac{N_{i}^{\text{det.}\cap\text{fid.}}}{N_{i}^{\text{det.}}}.$$

Finally, efficiency corrections, ϵ_j, are applied to account for events that satisfy the fiducial phase-space selection criteria but are not reconstructed in the detector:

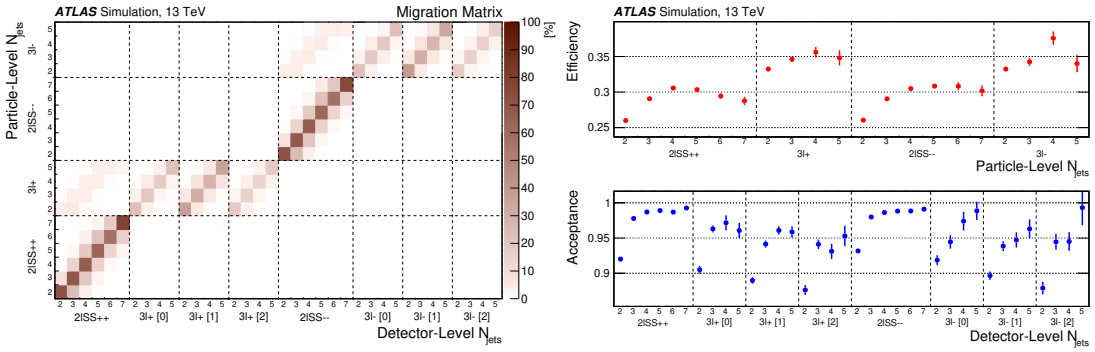
$$\epsilon_j = \frac{N_{j}^{\text{det.}\cap\text{fid.}}}{N_{j}^{\text{fid.}}}.$$

Here, $N_i^{\text{det.}}$ ($N_j^{\text{fid.}}$) represents the expected number of events in the i^{th} (j^{th}) bin of the detector-level (fiducial particle-level) histogram and $N_i^{\text{det.}\cap\text{fid.}}$ is the expected number of detector-level events in detector-level bin i summed over all particle-level bins.

Systematic uncertainties, evaluated at detector level, impact the unfolded cross-section measurements through modifications of the response matrix.

The binning scheme is optimised for each observable, except N_{jets}, so that at least 60% of the total number of events in a given particle-level bin are in the diagonal element of the migration matrix and there is low statistical uncertainty for the yields in a given reconstruction-level bin (i.e. taking into account the signal and background MC samples). The statistical uncertainty is required to be below 10% (16%) for high-purity (low-purity) regions to obtain similar bin granularity.

JHEP05(2024)131



(a) (b)

Figure 9. The (a) normalised migration matrix and (b) efficiency/acceptance corrections for N_{jets} calculated in SHERPA 2.2.10 with EWK corrections. The 3ℓ regions are split according to the number of OS-SF lepton pairs, shown in brackets. The highest jet-multiplicity bin in each subregion is inclusive.

Figure 9 shows the migration matrix, normalised to the total number of events in each truth bin, and the acceptance and efficiency corrections for N_{jets}. The 3ℓ regions are split according to the number of OS-SF lepton pairs. The fraction of events in the diagonal cells of the migration matrix shows the resolution of each observable. In the case of N_{jets}, the fractions along the diagonal are quite large, 60%–90%, for the 2ℓ regions, whereas for the 3ℓ regions the migrations between bins are split among their subregions in a roughly 1:2:1 ratio. The migrations between bins are generally smaller for the lepton-based observables, with angular variables showing the smallest migrations, and larger for the jet-based observables. The simultaneous unfolding of all fiducial regions shows a 10% migration of events from 3ℓ regions into 2ℓSS regions.

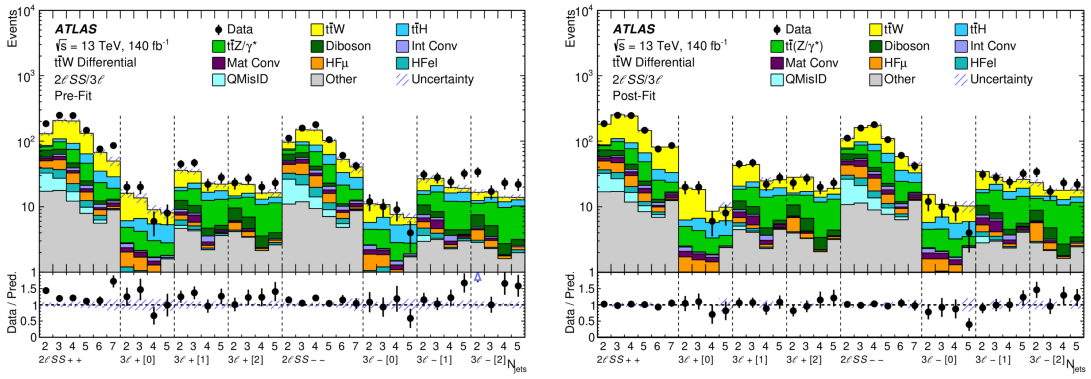
The detector-level distributions of N_{jets} are shown before and after the fit to data in figures 10(a) and 10(b) respectively. The 3ℓ regions are split according to the number of OS-SF lepton pairs, improving the discrimination between the signal $t\bar{t}W$ and the $t\bar{t}Z$ and VV background processes.

Tikhonov regularisation [117–120] in the PLU technique is implemented by an additional term, $R(\sigma_j, \tau_j)$, in the likelihood function that constrains the discrete second derivative of the generator-level bin normalisation factors to be close to zero. The regularisation strengths, τ_j, are fixed parameters that assume a common value across bins in each signal region and observable. The chosen τ_j values are optimised independently for each signal region and observable. The optimisation procedure is based on statistical bootstrapping to estimate the value of τ that minimises the global correlation coefficient ρ of the unfolded covariance matrix [121]. It is given by the following expression:

$$\rho = \left\langle \sqrt{1 - \left(V_{ii} V_{ii}^{-1}\right)^{-1}} \right\rangle_{i \in 1,\ldots,N_{\text{bins}}},$$

where V_{ij} is the covariance matrix of the bin normalisation factors. Pseudo-experiments are sampled from detector-level templates obtained from the background predictions and alternative $t\bar{t}W$ sample. Another optimisation procedure is studied, which selects the

JHEP05(2024)131



(a) (b)

Figure 10. Signal region datasets for the N_{jets} unfolding in (a) the pre-fit case and (b) the post-fit case. The 3ℓ regions are split according to the number of OS-SF lepton pairs, shown in brackets. The highest jet-multiplicity bin in each subregion is inclusive. The signal and background contributions before and after the likelihood fit to data under the signal-plus-background hypothesis are shown as filled histograms. The ratio of the data to the total pre-fit and post-fit predictions ("Pred.") is shown in the lower panel. The combined statistical and systematic uncertainty in the prediction is indicated by the blue hatched band. The blue triangles indicate points that are outside the vertical range of the figure.

maximum value of τ that does not increase the χ^2 between the unfolded observable's distribution and the alternative $t\bar{t}W$ generator-level template. The χ^2 is defined as:

$$\chi^2 = \sum_{i,j}^{n} \Delta\sigma_i C_{i,j}^{-1} \Delta\sigma_j,$$

where $\Delta\sigma_i$ is the difference between the unfolded data and the MC prediction and $C_{i,j}^{-1}$ is the inverse of the covariance matrix of the unfolded cross sections. The χ^2-based procedure yields larger values for τ than the ρ-based procedure. The ρ-based procedure is ultimately chosen because it is not sensitive to the choice of alternative $t\bar{t}W$ generator-level template, while the χ^2-based procedure will give a large bias when the shape of the observed data distribution differs from the nominal $t\bar{t}W$ prediction more than the alternative $t\bar{t}W$ prediction does.

Various closure and stress tests of the unfolding procedure are performed. Full closure is achieved in fits to an Asimov [122] dataset.[9] Additional validation tests are performed, for example by changing normalisations in certain regions or applying linear slopes in the particle-level distributions. In both cases, perfect retrieval of the injected particle-level distribution is observed, as expected from the PLU technique and the chosen regularisation technique. A stress test evaluating the bias in the unfolding procedure is performed by unfolding an Asimov dataset obtained using an alternative signal model. A similar stress test evaluating the sensitivity of the unfolding procedure to the limited number of simulated events is performed by splitting the nominal signal sample into two parts of equal size, where one part is used for the unfolding and the other is used to generate the Asimov dataset. Good closure is obtained in all cases. A comprehensive stress test is performed to characterise

[9]The Asimov dataset is an artificial data set defined so as to make estimators for all parameters equal to their true values.

JHEP05(2024)131

the level of bias as a function of τ by unfolding Asimov datasets generated by injecting quadratic shapes into the signal templates, either with an enhancement in the core of the distribution or in the upper tail. In the case where shapes have 200% enhancement, the median bias in any bin relative to its total uncertainty is between 1% and 30%. An additional data-driven test is performed to evaluate the bias in the unfolded observed data. Each observable is first unfolded with no regularisation to obtain a particle-level distribution for the data with no bias. The distributions are fitted with a second-order polynomial to capture the lowest-order shape that is removed by regularisation. These fits are used to generate smooth Asimov pseudo-data templates that are unfolded in fits with regularisation, but only including statistical uncertainties. The correct pseudo-data shapes are in general recovered well, with deviations that are typically very small relative to statistical uncertainties across all bins and observables, and with χ^2 p-values near 1.0 for the observables listed in table 11.

As expected, given the larger-than-predicted measured inclusive cross-section, the absolute differential cross-sections measured in data are larger than the theoretical predictions in most regions of phase space. To better understand normalisation and shape effects in the comparison of the measurements with predictions, the absolute and normalised cross-sections are shown for each of the measured observables. Several different representations of the differential cross-section measurements are shown for each observable. Firstly, the measured absolute differential cross-sections for combined lepton-charge regions, the measured normalised differential cross-sections for combined lepton-charge regions, and the differential $A_{\mathrm{C}}^{\mathrm{rel}}$ measurement are shown. Secondly, measurements of both the absolute and normalised cross-sections and the differential cross-sections are shown for each lepton-charge channel. Although the parameterisation of the yields in the different lepton-charge regions differs between the two cases, the underlying data are the same.

The results are shown in figures 11–16. The measurements are compared with the theoretical predictions previously described in section 3. Only the results in the 3ℓ channel are compared with a dedicated theoretical prediction based on the procedure outlined in ref. [23] that includes off-shell effects. This prediction is calculated at parton level and corrected to particle level by applying bin-by-bin scaling factors that account for non-perturbative effects, such as multiparton interactions and hadronisation.

The compatibility of the measured differential cross-section distributions and the predictions is assessed by calculating χ^2 values and probabilities, for the relevant number of degrees of freedom, properly taking into account uncertainty correlations. These values are shown in tables 13 and 14 for the normalised cross-sections in the 2ℓSS and 3ℓ regions respectively. They are shown for the normalised cross-sections rather than the absolute cross-sections in order to give a better indication of how well the theoretical predictions agree with the data, without having to take account of the known difference between the predicted and measured inclusive absolute cross-sections. The χ^2 p-values for compatibility of the absolute cross-section measurements and the Sherpa predictions are in the range of 6%–70%, and typically less than 10% in the 2ℓSS region. Tables 15 and 16 show the χ^2 values and p-values for compatibility of the predicted and measured $A_{\mathrm{C}}^{\mathrm{rel}}$ distributions in the 2ℓSS and 3ℓ regions respectively.

JHEP05(2024)131

Observable	NDF	Sherpa 2.2.10		MG5aMC+Py8 FxFx		MG5aMC+Py8 Incl.		Powheg+Py8		Powheg+H7	
		χ^2	p-value	χ^2	p-value	χ^2	p-value	χ^2	p-value	χ^2	p-value
N_{jets}	5	6.5	0.26	7.8	0.17	6.9	0.23	7.2	0.21	6.8	0.24
$H_{\text{T}}^{\text{jet}}$	5	2.0	0.85	2.3	0.81	1.9	0.86	2.5	0.78	2.7	0.75
$H_{\text{T}}^{\text{lep}}$	7	6.1	0.53	6.3	0.51	5.9	0.55	5.9	0.56	5.9	0.55
$\Delta R_{\ell b,\,\text{lead}}$	7	6.8	0.45	7.2	0.41	7.2	0.41	7.2	0.40	7.1	0.41
$\lvert\Delta\phi_{\ell\ell,\,\text{SS}}\rvert$	7	1.7	0.97	1.7	0.98	1.9	0.96	1.8	0.97	1.9	0.97
$\lvert\Delta\eta_{\ell\ell,\,\text{SS}}\rvert$	6	7.0	0.32	8.1	0.23	12.1	0.06	10.2	0.12	10.1	0.12

Table 13. χ^2 and p-values calculated for unfolded normalised cross-section distributions in the 2ℓSS region.

Observable	NDF	Sherpa 2.2.10		Off-Shell		MG5aMC+Py8 FxFx		MG5aMC+Py8 Incl.		Powheg+Py8		Powheg+H7	
		χ^2	p-value	χ^2	p-value	χ^2	p-value	χ^2	p-value	χ^2	p-value	χ^2	p-value
N_{jets}	3	0.4	0.95	-	-	0.3	0.96	0.5	0.92	1.0	0.81	1.1	0.77
$H_{\text{T}}^{\text{jet}}$	4	1.5	0.82	-	-	1.2	0.88	1.9	0.76	2.2	0.70	2.8	0.59
$H_{\text{T}}^{\text{lep}}$	5	1.6	0.90	2.7	0.75	1.9	0.86	2.2	0.81	2.1	0.84	1.9	0.86
$\Delta R_{\ell b,\,\text{lead}}$	5	9.1	0.10	8.5	0.13	9.3	0.10	8.9	0.11	8.8	0.12	8.8	0.12
$\lvert\Delta\phi_{\ell\ell,\,\text{SS}}\rvert$	5	4.5	0.48	4.5	0.48	4.5	0.48	4.3	0.51	4.4	0.49	4.3	0.50
$\lvert\Delta\eta_{\ell\ell,\,\text{SS}}\rvert$	5	6.0	0.31	5.6	0.35	5.8	0.32	5.5	0.36	5.4	0.37	5.6	0.35

Table 14. χ^2 and p-values calculated for unfolded normalised cross-section distributions in the 3ℓ region.

Observable	NDF	Sherpa 2.2.10		MG5aMC+Py8 FxFx		MG5aMC+Py8 Incl.		Powheg+P8		Powheg+H7	
		χ^2	p-value	χ^2	p-value	χ^2	p-value	χ^2	p-value	χ^2	p-value
N_{jets}	6	3.8	0.70	4.0	0.68	3.5	0.75	3.3	0.78	3.2	0.78
$H_{\text{T}}^{\text{jet}}$	6	2.7	0.84	3.0	0.81	1.8	0.93	1.7	0.95	1.6	0.95
$H_{\text{T}}^{\text{lep}}$	8	5.7	0.68	5.6	0.69	3.0	0.94	3.4	0.91	3.3	0.91
$\Delta R_{\ell b,\,\text{lead}}$	8	5.1	0.75	5.3	0.72	4.5	0.81	4.4	0.82	4.4	0.81
$\lvert\Delta\phi_{\ell\ell,\,\text{SS}}\rvert$	8	8.2	0.41	9.0	0.34	7.4	0.49	7.5	0.48	7.5	0.48
$\lvert\Delta\eta_{\ell\ell,\,\text{SS}}\rvert$	7	8.9	0.26	8.8	0.26	7.8	0.35	8.1	0.32	8.0	0.33

Table 15. χ^2 and p-values calculated for unfolded asymmetry distributions in the 2ℓSS region.

Observable	NDF	Sherpa 2.2.10		Off-Shell		MG5aMC+Py8 FxFx		MG5aMC+Py8 Incl.		Powheg+Py8		Powheg+H7	
		χ^2	p-value	χ^2	p-value	χ^2	p-value	χ^2	p-value	χ^2	p-value	χ^2	p-value
N_{jets}	4	4.3	0.37	-	-	4.7	0.32	4.5	0.34	4.8	0.31	4.6	0.33
$H_{\text{T}}^{\text{jet}}$	5	4.1	0.53	-	-	4.4	0.50	4.5	0.48	4.6	0.47	4.5	0.48
$H_{\text{T}}^{\text{lep}}$	6	3.6	0.73	3.6	0.73	3.6	0.73	3.7	0.72	3.6	0.73	3.6	0.73
$\Delta R_{\ell b,\,\text{lead}}$	6	3.3	0.77	3.3	0.77	3.9	0.69	4.1	0.66	3.9	0.69	3.9	0.69
$\lvert\Delta\phi_{\ell\ell,\,\text{SS}}\rvert$	6	7.2	0.30	7.2	0.30	7.7	0.26	7.6	0.27	7.8	0.26	7.6	0.27
$\lvert\Delta\eta_{\ell\ell,\,\text{SS}}\rvert$	6	4.9	0.56	5.1	0.53	5.4	0.50	5.4	0.49	5.3	0.50	5.1	0.53

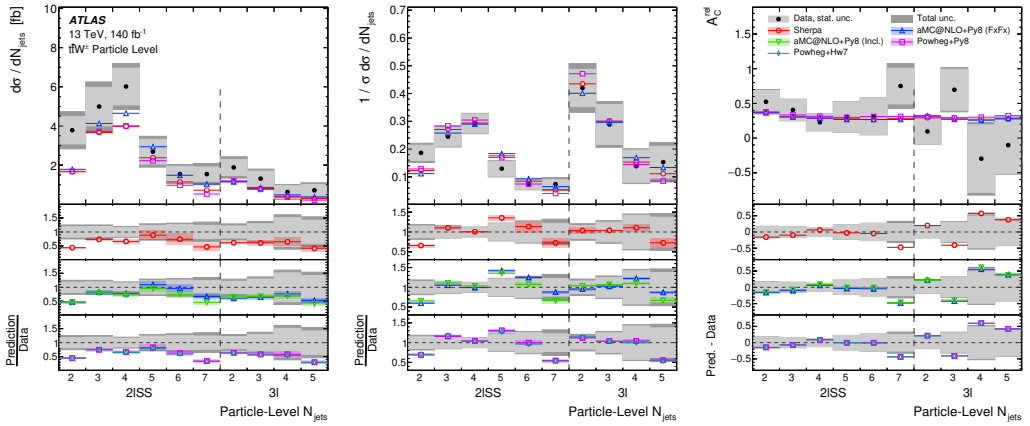
Table 16. χ^2 and p-values calculated for unfolded asymmetry distributions in the 3ℓ region.

JHEP05(2024)131

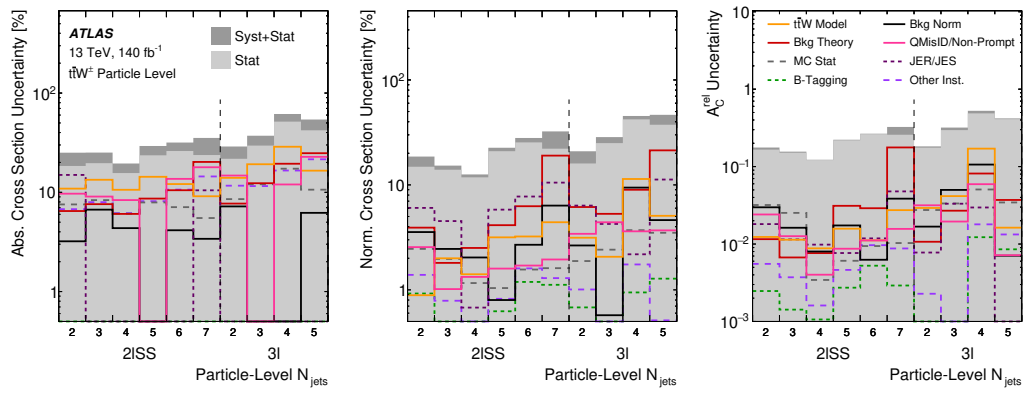
Figure 11(a) shows the measured absolute cross-section, normalised cross-section and $A_{\mathrm{C}}^{\mathrm{rel}}$ as a function of N_{jets}. The corresponding uncertainty breakdown is shown in figure 11(b). In most bins the largest uncertainties come from the limited amount of data; these dominate across all bins of the 3ℓ channel and at low and high jet multiplicities in the 2ℓSS channel. The dominant systematic uncertainty stems from the $t\bar{t}W$ model and is due to the difference between the unfolded results from different choices of $t\bar{t}W$ reference sample. At large jet multiplicities the theoretical uncertainty of the background model and non-prompt-lepton BDT are the largest. The total uncertainty in the normalised cross-section measurements is somewhat reduced; a major contribution to this is the smaller $t\bar{t}W$ model uncertainty after removing normalisation effects. The $A_{\mathrm{C}}^{\mathrm{rel}}$ measurement uncertainty is dominated by the statistical uncertainty across the range of jet multiplicities because many systematic uncertainties cancel each other out in the ratio. The absolute cross-section measured in data is higher than all the theoretical predictions, the largest discrepancy being at low jet multiplicities in the 2ℓSS channel. At high multiplicities the predictions with additional partons using NLO merging are in better agreement with the data than the NLO+PS prediction from Powheg, as expected, for both the 2ℓSS and 3ℓ channels. Taking the scale uncertainties into account, these are compatible with the data for jet multiplicities greater than four. Uncertainties due to the scales are approximately 10% for low jet multiplicities and increase to about 40% for higher multiplicities. The main $t\bar{t}W$ contribution to the 2ℓSS selection is the final state with two leptonically decaying W bosons, one from the decay of a top quark and one from the associated W boson. This gives rise to a final state with four partons from the hadronic decay of the remaining W boson and the b-quarks from the top quark decays. Therefore, the disagreement between theory and data at lower jet multiplicities is independent of the modelling of additional partons and is observed for both the NLO+PS generators and those with additional partons using NLO merging. The shape of the $A_{\mathrm{C}}^{\mathrm{rel}}$ distribution as a function of the number of jets shows some tension between data and the predictions. The measured asymmetry is larger at low and high jet multiplicities while being in agreement at intermediate numbers of four or five jets in the 2ℓSS channel. This is driven by a large mismodelling in the 2ℓSS++ region, while the 2ℓSS−− jet multiplicity distribution is in better agreement in both shape and overall cross-section. This can be seen in right panel of figure 11(c) for the normalised cross-section measurements, where, especially for the 2ℓSS channel, the agreement in shape is rather good for the predictions with additional partons using NLO merging.

Figure 12(a) shows the measured absolute cross-section, normalised cross-section and $A_{\mathrm{C}}^{\mathrm{rel}}$ as a function of $H_{\mathrm{T}}^{\mathrm{jet}}$. The corresponding uncertainty breakdowns are shown in figure 12(b). Again, the limited amount of data is the largest source of uncertainty across most bins of the measurement. The main systematic uncertainties come from the modelling of the $t\bar{t}W$ signal process, with an important additional contribution from the jet energy scale and resolution, particularly in the low $H_{\mathrm{T}}^{\mathrm{jet}}$ region. The absolute cross-section measurements indicate a slight improvement in modelling at high $H_{\mathrm{T}}^{\mathrm{jet}}$ from the predictions with additional partons using NLO merging, similarly to what was seen for N_{jets}. The normalised cross-section measurements, shown in the middle panel of figure 12(a), show that the modelling of the distribution's shape is generally very good in the 2ℓSS channel, while the predictions favour lower values than the data in the 3ℓ channel. The $A_{\mathrm{C}}^{\mathrm{rel}}$ distribution predictions are also in

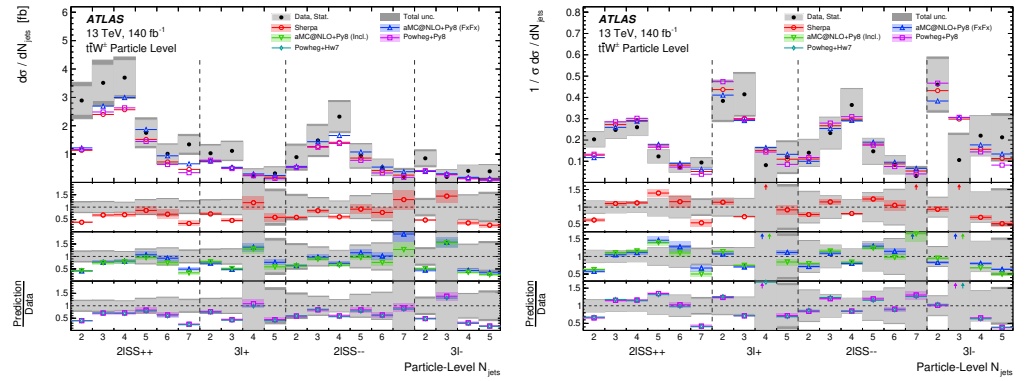
JHEP05(2024)131



(a)



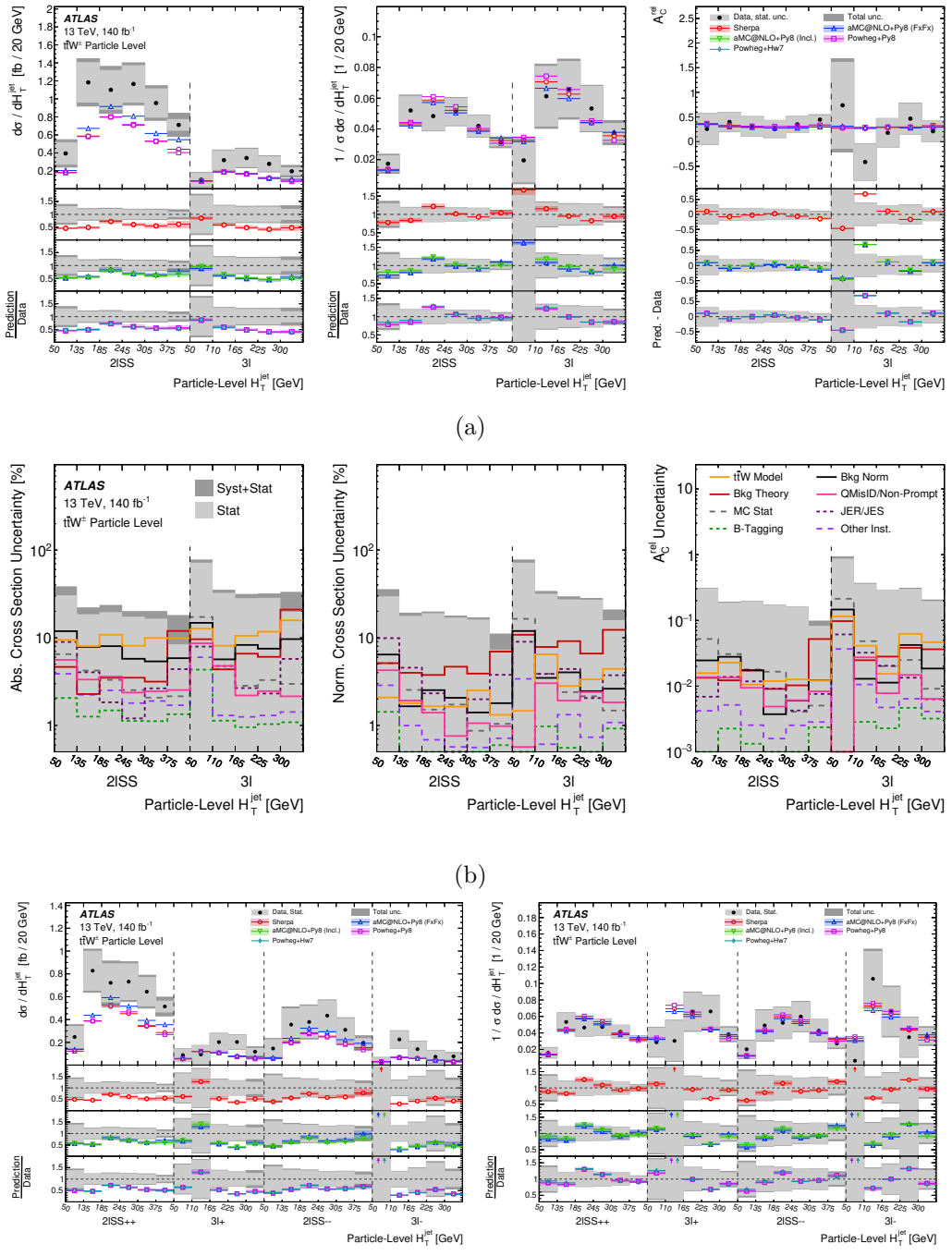
(b)



(c)

Figure 11. Unfolded distributions of (a) the lepton-charge-combined absolute cross-section, the normalised cross-section and A_C^{rel}, (b) the corresponding uncertainty breakdowns, and (c) unfolded distributions of the lepton-charge-split absolute and normalised cross-sections, as a function of jet multiplicity. The coloured markers overlaid upon the cross-section measurements show different theoretical predictions. The breakdown of statistical-only uncertainties is shown in light grey in the bottom panels, and combined statistical and systematic uncertainties are shown in dark grey. The dotted/dashed/full lines in (b) show the relative contributions of grouped sources of systematic uncertainty. The triangles indicate points that are outside the vertical range of the figure.

JHEP05(2024)131



(a)

(b)

(c)

Figure 12. Unfolded distributions of (a) the lepton-charge-combined absolute cross-section, the normalised cross-section and $A_{\mathrm{C}}^{\mathrm{rel}}$, (b) the corresponding uncertainty breakdowns, and (c) unfolded distributions of the lepton-charge-split absolute and normalised cross-sections, as a function of $H_{\mathrm{T}}^{\mathrm{jet}}$. The coloured markers overlaid upon the cross-section measurements show different theoretical predictions. The breakdown of statistical-only uncertainties is shown in light grey in the bottom panels, and combined statistical and systematic uncertainties are shown in dark grey. The dotted/dashed/full lines in (b) show the relative contributions of grouped sources of systematic uncertainty. The triangles indicate points that are outside the vertical range of the figure.

JHEP05(2024)131

agreement with data in the 2ℓSS region, but not in the 3ℓ region. This seems to be driven by a significant difference between data and predictions in the $3\ell+$ region, as shown in figure 12(c).

Figure 13(a) shows the measured absolute cross-section, normalised cross-section and $A_{\mathrm{C}}^{\mathrm{rel}}$ as a function of $H_{\mathrm{T}}^{\mathrm{lep}}$. The corresponding uncertainties are shown in figure 13(b). The dominant systematic uncertainty across the $H_{\mathrm{T}}^{\mathrm{lep}}$ range comes from the $t\bar{t}W$ model, with additional contributions from the background normalisation and lepton charge misidentification and non-prompt-lepton BDT at lower $H_{\mathrm{T}}^{\mathrm{lep}}$ values. This observable is less sensitive to the modelling of additional jet activity in the event, so the NLO+PS predictions and the predictions with additional partons using NLO merging give similar results. In the 3ℓ channel, the prediction including off-shell effects reports a slightly higher absolute cross-section than the predictions with additional partons using NLO merging and therefore has overall better agreement with the data. The "off-shell" p-value for the absolute cross-section distribution is 0.85 compared to a value of 0.61 for the Powheg+Pythia 8 prediction. All predictions are generally in good agreement with each other in the normalised cross-section results for $H_{\mathrm{T}}^{\mathrm{lep}}$. Although the predicted $H_{\mathrm{T}}^{\mathrm{lep}}$ distribution shape differs slightly from the data, this is not very significant. It is interesting to note that a significant decrease in the systematic uncertainty is observed, especially at intermediate values of $H_{\mathrm{T}}^{\mathrm{lep}}$, for the normalised cross-section measurement shown in figure 13(b). This is due to the large decrease in several key uncertainties, including uncertainties in the $t\bar{t}W$ model and background normalisation and theoretical uncertainties in the background modelling. The values of $A_{\mathrm{C}}^{\mathrm{rel}}$ in data tend to be lower than predicted in both the 2ℓSS and 3ℓ channels for lower values of $H_{\mathrm{T}}^{\mathrm{lep}}$, the origin of which can be seen in figure 13(c).

Figure 14(a) shows the measured absolute cross-section, normalised cross-section and $A_{\mathrm{C}}^{\mathrm{rel}}$ as a function of $\Delta R_{\ell b,\,\mathrm{lead}}$. A significant decrease in the systematic uncertainty is observed for the normalised cross-section measurement across the range of $\Delta R_{\ell b,\,\mathrm{lead}}$ values, as shown in figure 14(b). A mild discrepancy between data and predictions is observed at low $\Delta R_{\ell b,\,\mathrm{lead}}$ for $A_{\mathrm{C}}^{\mathrm{rel}}$ in the 2ℓSS channel. This is because at low $\Delta R_{\ell b,\,\mathrm{lead}}$ values in the 2ℓSS$--$ channel the cross-sections measured in data are lower than the predictions, as shown in figure 14(c), yielding the different $A_{\mathrm{C}}^{\mathrm{rel}}$ values.

Figure 15(a) shows the measured absolute cross-section, normalised cross-section and $A_{\mathrm{C}}^{\mathrm{rel}}$ as a function of $|\Delta\phi_{\ell\ell,\,\mathrm{SS}}|$. The normalised cross-section measurements show generally good agreement between data and the predictions in the overall shape of the distributions. However, there is some deviation between the data and the predictions for $A_{\mathrm{C}}^{\mathrm{rel}}$, which is expected to have a constant value across $|\Delta\phi_{\ell\ell,\,\mathrm{SS}}|$. The cross-section observed in data is larger than the predictions at low and high $|\Delta\phi_{\ell\ell,\,\mathrm{SS}}|$ in the 2ℓSS$++$ channel, whereas in the 2ℓSS$--$ channel the cross-section observed in data is larger than the predictions at intermediate values of $|\Delta\phi_{\ell\ell,\,\mathrm{SS}}|$. This can be seen in figure 15(c) and is reflected in the χ^2 p-value of 0.41 with respect to the Sherpa prediction in table 15.

Figure 16(a) shows the measured absolute cross-section, normalised cross-section and $A_{\mathrm{C}}^{\mathrm{rel}}$ as a function of $|\Delta\eta_{\ell\ell,\,\mathrm{SS}}|$. Discrepancies between the measurements in data and the theoretical predictions can be seen in the cross-section and the $A_{\mathrm{C}}^{\mathrm{rel}}$ distributions for both the 2ℓSS and 3ℓ channels. The data show higher values of the measured cross-section compared to the theoretical predictions at high and low $|\Delta\eta_{\ell\ell,\,\mathrm{SS}}|$ values in the 2ℓSS channel, for which the χ^2 p-value with respect to the Sherpa prediction for the normalised cross-section measurement

JHEP05(2024)131

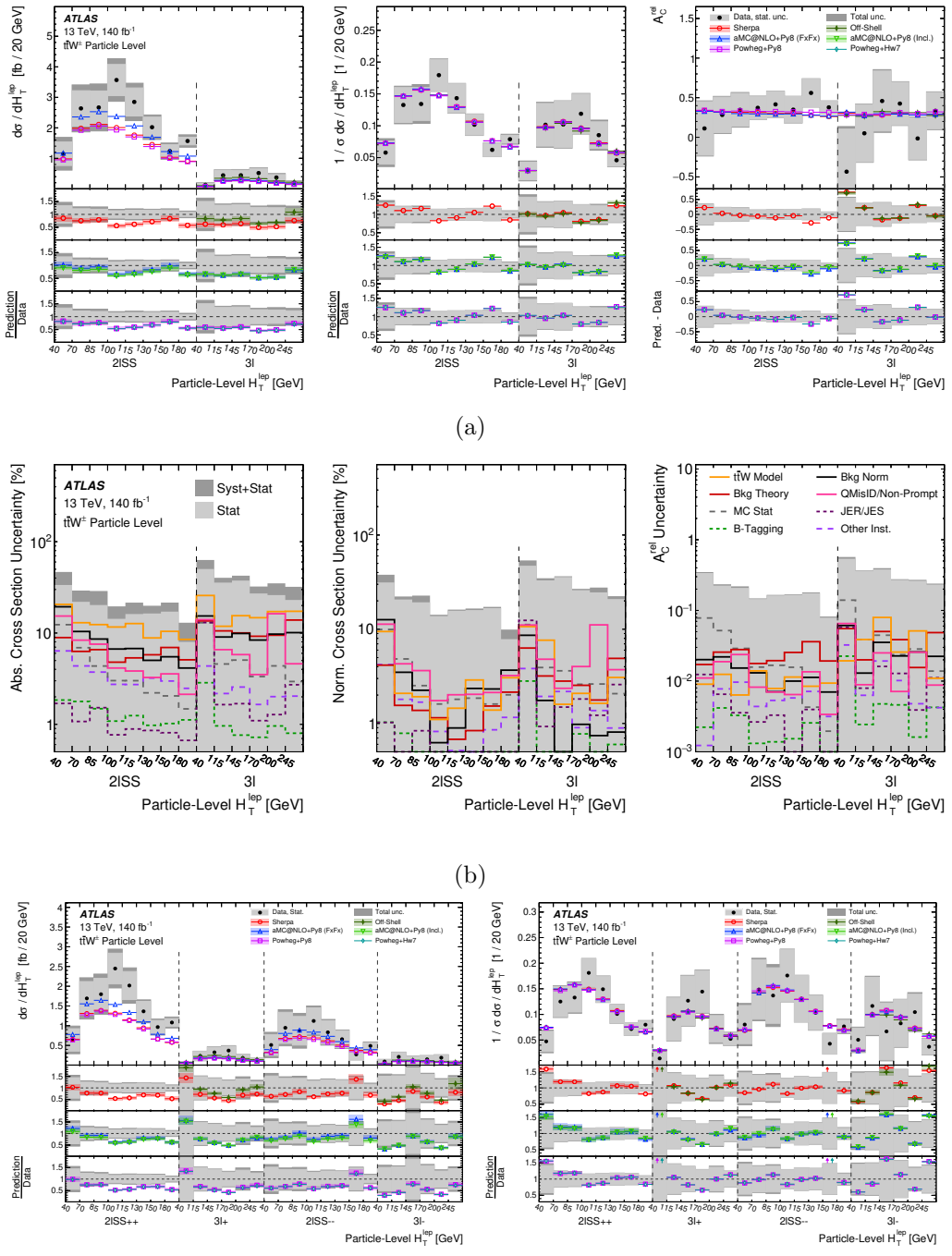
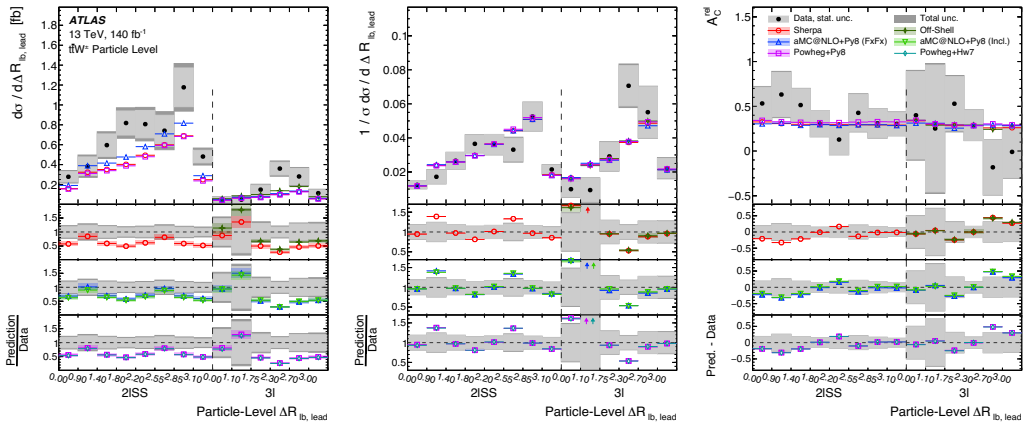
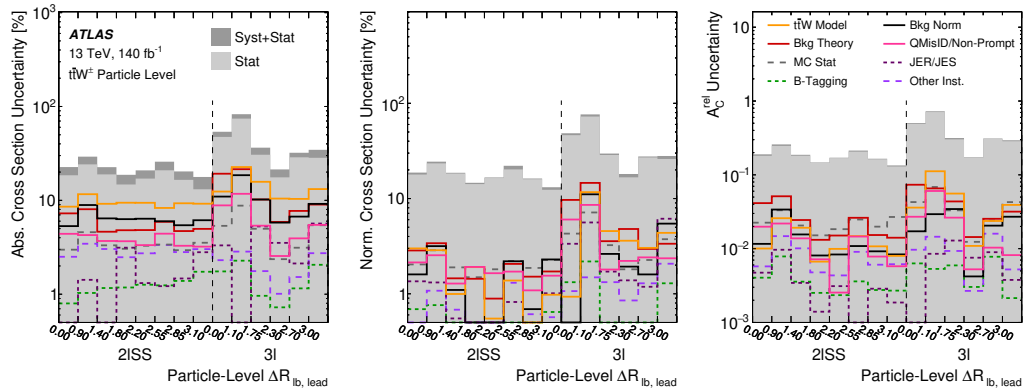


Figure 13. Unfolded distributions of (a) the lepton-charge-combined absolute cross-section, the normalised cross-section and $A_{\mathrm{C}}^{\mathrm{rel}}$, (b) the corresponding uncertainty breakdowns, and (c) unfolded distributions of the lepton-charge-split absolute and normalised cross-sections, as a function of $H_{\mathrm{T}}^{\mathrm{lep}}$. The coloured markers overlaid upon the cross-section measurements show different theoretical predictions. The breakdown of statistical-only uncertainties is shown in light grey in the bottom panels, and combined statistical and systematic uncertainties are shown in dark grey. The dotted/dashed/full lines in (b) show the relative contributions of grouped sources of systematic uncertainty. The triangles indicate points that are outside the vertical range of the figure.

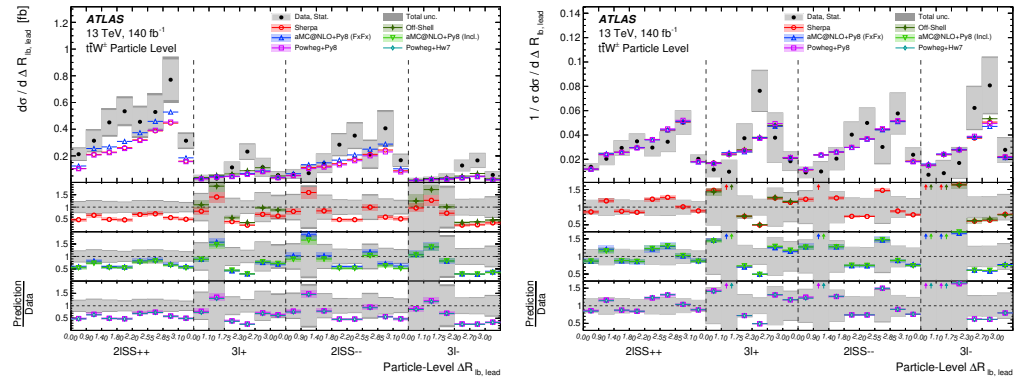
JHEP05(2024)131



(a)



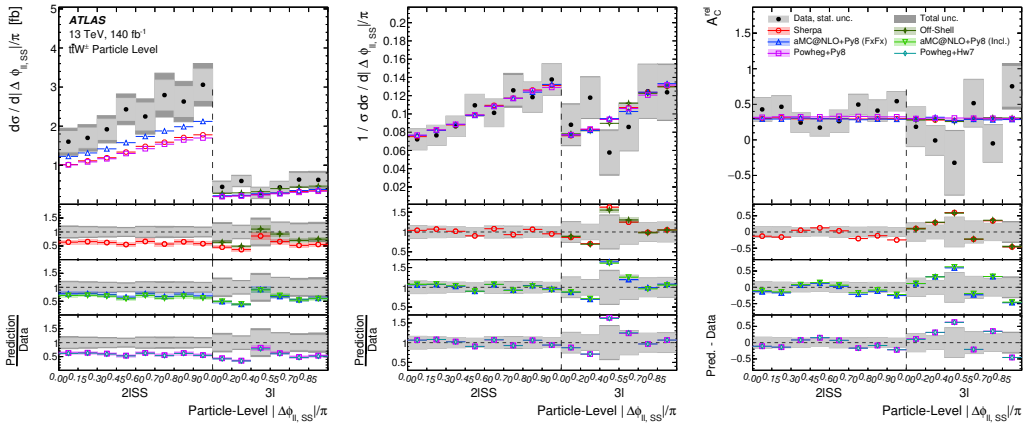
(b)



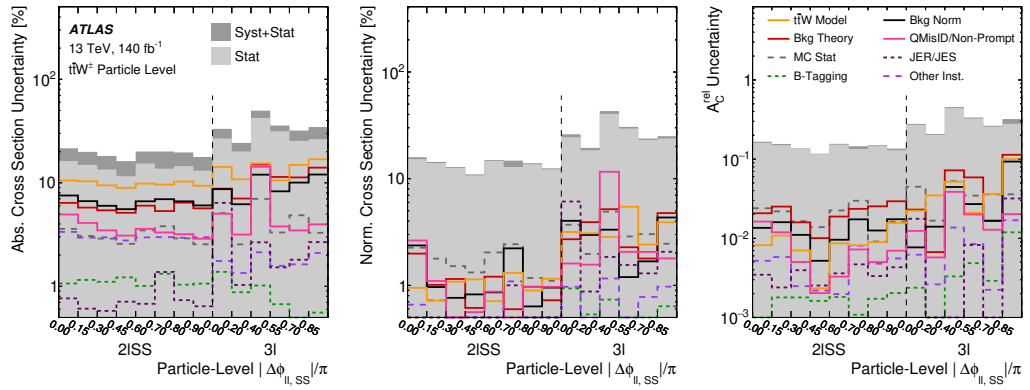
(c)

Figure 14. Unfolded distributions of (a) the lepton-charge-combined absolute cross-section, the normalised cross-section and $A_{\mathrm{C}}^{\mathrm{rel}}$, (b) the corresponding uncertainty breakdowns, and (c) unfolded distributions of the lepton-charge-split absolute and normalised cross-sections, as a function of $\Delta R_{\ell b,\,\mathrm{lead}}$. The coloured markers overlaid upon the cross-section measurements show different theoretical predictions. The breakdown of statistical-only uncertainties is shown in light grey in the bottom panels, and combined statistical and systematic uncertainties are shown in dark grey. The dotted/dashed/full lines in (b) show the relative contributions of grouped sources of systematic uncertainty. The triangles indicate points that are outside the vertical range of the figure.

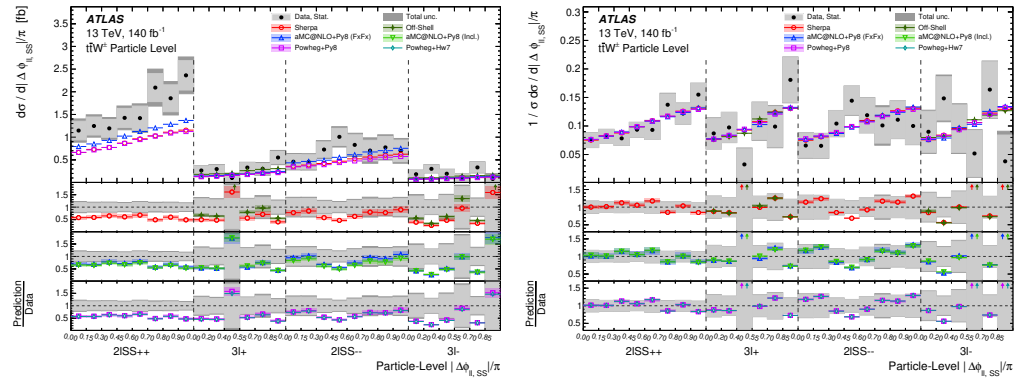
JHEP05(2024)131



(a)



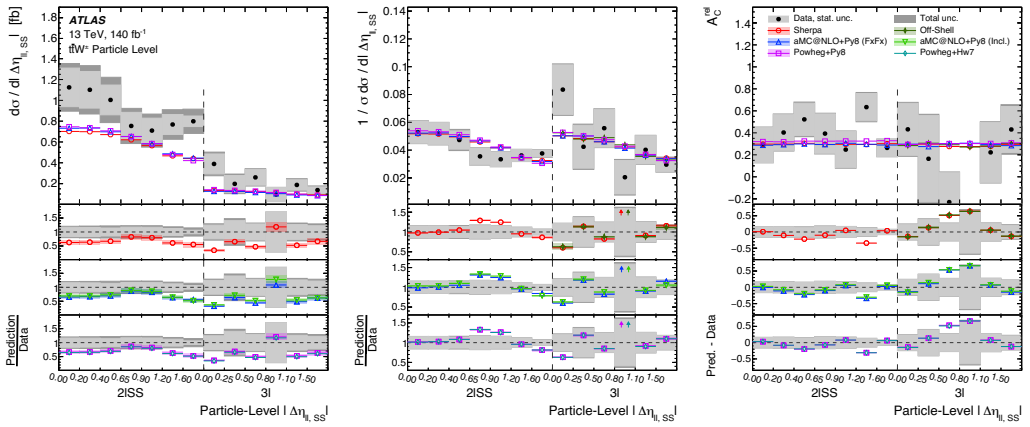
(b)



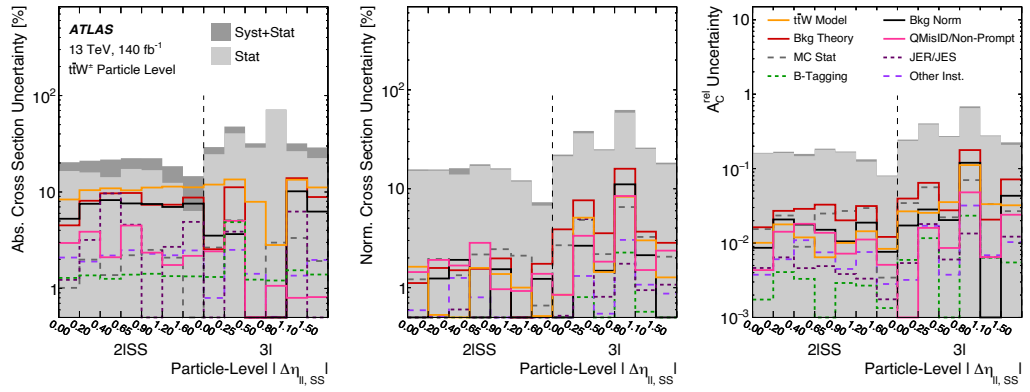
(c)

Figure 15. Unfolded distributions of (a) the lepton-charge-combined absolute cross-section, the normalised cross-section and $A_{\mathrm{C}}^{\mathrm{rel}}$, (b) the corresponding uncertainty breakdowns, and (c) unfolded distributions of the lepton-charge-split absolute and normalised cross-sections, as a function of $|\Delta\phi_{\ell\ell,\,\mathrm{SS}}|$. The coloured markers overlaid upon the cross-section measurements show different theoretical predictions. The breakdown of statistical-only uncertainties is shown in light grey in the bottom panels, and combined statistical and systematic uncertainties are shown in dark grey. The dotted/dashed/full lines in (b) show the relative contributions of grouped sources of systematic uncertainty. The triangles indicate points that are outside the vertical range of the figure.

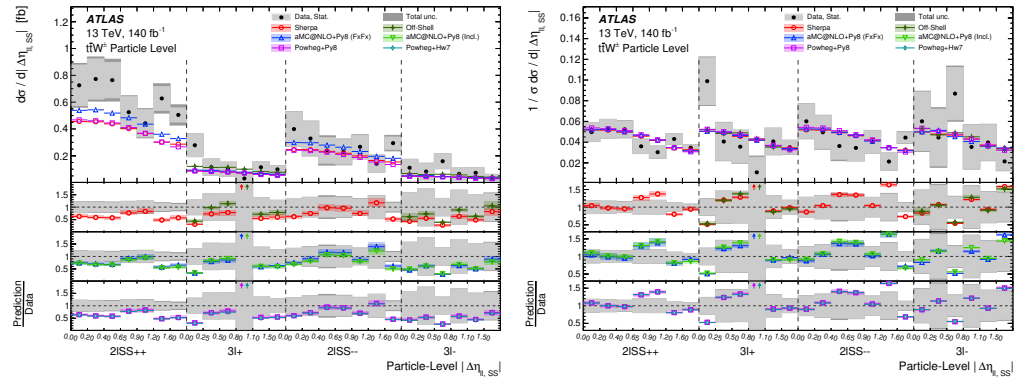
JHEP05(2024)131



(a)



(b)



(c)

Figure 16. Unfolded distributions of (a) the lepton-charge-combined absolute cross-section, the normalised cross-section and A_C^{rel}, (b) the corresponding uncertainty breakdowns, and (c) unfolded distributions of the lepton-charge-split absolute and normalised cross-sections, as a function of $|\Delta\eta_{\ell\ell,\mathrm{SS}}|$. The coloured markers overlaid upon the cross-section measurements show different theoretical predictions. The breakdown of statistical-only uncertainties is shown in light grey in the bottom panels, and combined statistical and systematic uncertainties are shown in dark grey. The dotted/dashed/full lines in (b) show the relative contributions of grouped sources of systematic uncertainty. The triangles indicate points that are outside the vertical range of the figure.

JHEP05(2024)131

is 0.32 as shown in table 13. The $A_{\mathrm{C}}^{\mathrm{rel}}$ measured in data is larger than the predictions for intermediate $|\Delta\eta_{\ell\ell,\mathrm{SS}}|$ values in the 2ℓSS channel, whereas the opposite is seen in the 3ℓ channel, where there are very different trends in data and predictions for the $3\ell+$ and $3\ell-$ channels, as shown in figure 16(c). However, these trends are not statistically significant.

In summary, all absolute cross-section measurements show a significant normalisation effect, as expected from the larger-than-predicted result of the inclusive cross-section measurement. Additionally, some observables show mild tension between data and prediction in parts of the normalised cross-section distributions. However, the observed χ^2 p-value for any single distribution does not indicate a significant disagreement between the data and theoretical predictions at the current accuracy of the measurements.

9 Conclusion

Measurements of both the inclusive and differential cross-sections for producing a top-quark-antiquark pair in association with a W boson ($t\bar{t}W$) are presented. The measurements are based on $\sqrt{s} = 13\,\mathrm{TeV}$ proton-proton collision data with an integrated luminosity of $140\,\mathrm{fb}^{-1}$, recorded from 2015 to 2018 with the ATLAS detector at the Large Hadron Collider. The signal regions are split into final states with two same-sign or three isolated leptons (electrons or muons), and are further split according to their total lepton charge. Additional background-enriched regions are used in the fit to improve the modelling of several leading backgrounds. The inclusive $t\bar{t}W$ production cross-section is found to be $880 \pm 80\,\mathrm{fb}$, which is consistent with the previous measurement from CMS and other analyses probing similar $t\bar{t}W$-enriched regions. Improved theoretical calculations have led to increases in the predicted cross-section through the corrections for missing higher-order QCD and EWK effects. Some tension between the predictions and the data remains. The measurement and the SM NNLO theoretical prediction of $745 \pm 50\,(\mathrm{scale}) \pm 13\,(\text{2-loop approx.}) \pm 19\,(\mathrm{PDF},\,\alpha_{\mathrm{s}})\,\mathrm{fb}$ are compatible at the level of 1.4σ. The ratio of cross-sections from different charges of the associated W boson is measured to be $R(t\bar{t}W) = 1.96 \pm 0.22$ and the relative charge asymmetry is measured to be $A_{\mathrm{C}}^{\mathrm{rel}} = 0.33 \pm 0.05$, both are dominated by statistical uncertainties, but agree with theoretical predictions.

Differential absolute and normalised cross-section measurements are performed for several particle-level observables. The compatibility between data and predictions for the overall normalisation of the absolute cross-section measurements is consistent with the inclusive measurement result. The latest off-shell fixed-order predictions do not address this observed tension, concluding that the latter does not originate from the additional single-resonant and non-resonant contributions that this calculation includes on top of the double-resonant contribution contained in the predictions matched to parton showers.

The compatibility of the data with theoretical predictions from different MC generators is tested; for the normalised cross-section measurements, compatibility is demonstrated by χ^2 p-values above 0.3 for the Sherpa predictions for almost all observables.

Acknowledgments

We thank CERN for the very successful operation of the LHC and its injectors, as well as the support staff at CERN and at our institutions worldwide without whom ATLAS could not be operated efficiently.

JHEP05(2024)131

The crucial computing support from all WLCG partners is acknowledged gratefully, in particular from CERN, the ATLAS Tier-1 facilities at TRIUMF/SFU (Canada), NDGF (Denmark, Norway, Sweden), CC-IN2P3 (France), KIT/GridKA (Germany), INFN-CNAF (Italy), NL-T1 (Netherlands), PIC (Spain), RAL (U.K.) and BNL (U.S.A.), the Tier-2 facilities worldwide and large non-WLCG resource providers. Major contributors of computing resources are listed in ref. [123].

We gratefully acknowledge the support of ANPCyT, Argentina; YerPhI, Armenia; ARC, Australia; BMWFW and FWF, Austria; ANAS, Azerbaijan; CNPq and FAPESP, Brazil; NSERC, NRC and CFI, Canada; CERN; ANID, Chile; CAS, MOST and NSFC, China; Minciencias, Colombia; MEYS CR, Czech Republic; DNRF and DNSRC, Denmark; IN2P3-CNRS and CEA-DRF/IRFU, France; SRNSFG, Georgia; BMBF, HGF and MPG, Germany; GSRI, Greece; RGC and Hong Kong SAR, China; ISF and Benoziyo Center, Israel; INFN, Italy; MEXT and JSPS, Japan; CNRST, Morocco; NWO, Netherlands; RCN, Norway; MEiN, Poland; FCT, Portugal; MNE/IFA, Romania; MESTD, Serbia; MSSR, Slovakia; ARRS and MIZŠ, Slovenia; DSI/NRF, South Africa; MICINN, Spain; SRC and Wallenberg Foundation, Sweden; SERI, SNSF and Cantons of Bern and Geneva, Switzerland; MOST, Taipei; TENMAK, Türkiye; STFC, United Kingdom; DOE and NSF, United States of America.

Individual groups and members have received support from BCKDF, CANARIE, CRC and DRAC, Canada; PRIMUS 21/SCI/017 and UNCE SCI/013, Czech Republic; COST, ERC, ERDF, Horizon 2020, ICSC-NextGenerationEU and Marie Skłodowska-Curie Actions, European Union; Investissements d'Avenir Labex, Investissements d'Avenir Idex and ANR, France; DFG and AvH Foundation, Germany; Herakleitos, Thales and Aristeia programmes co-financed by EU-ESF and the Greek NSRF, Greece; BSF-NSF and MINERVA, Israel; Norwegian Financial Mechanism 2014-2021, Norway; NCN and NAWA, Poland; La Caixa Banking Foundation, CERCA Programme Generalitat de Catalunya and PROMETEO and GenT Programmes Generalitat Valenciana, Spain; Göran Gustafssons Stiftelse, Sweden; The Royal Society and Leverhulme Trust, United Kingdom.

In addition, individual members wish to acknowledge support from Chile: Agencia Nacional de Investigación y Desarrollo (FONDECYT 1190886, FONDECYT 1210400); China: National Natural Science Foundation of China (NSFC - 12175119, NSFC 12275265); EU: H2020 European Research Council (H2020-MSCA-IF-2020: HPOFHIC - 10103); European Union: European Research Council (ERC - 948254), Horizon 2020 Framework Programme (MUCCA - CHIST-ERA-19-XAI-00), Italian Center for High Performance Computing, Big Data and Quantum Computing (ICSC, NextGenerationEU), Marie Sklodowska-Curie Actions (EU H2020 MSC IF GRANT NO 101033496); France: Agence Nationale de la Recherche (ANR-20-CE31-0013, ANR-21-CE31-0022), Investissements d'Avenir Idex (ANR-11-LABX-0012), Investissements d'Avenir Labex (ANR-11-LABX-0012); Germany: Baden-Württemberg Stiftung (BW Stiftung-Postdoc Eliteprogramme), Deutsche Forschungsgemeinschaft (DFG - CR 312/5-1); Italy: Istituto Nazionale di Fisica Nucleare (FELLINI G.A. n. 754496, ICSC, NextGenerationEU); Japan: Japan Society for the Promotion of Science (JSPS KAKENHI 22H01227, JSPS KAKENHI JP21H05085, JSPS KAKENHI JP22H04944); Netherlands: Netherlands Organisation for Scientific Research (NWO Veni 2020 - VI.Veni.202.179); Norway: Research Council of Norway (RCN-314472); Poland: Polish National Agency for Academic

JHEP05(2024)131

Exchange (PPN/PPO/2020/1/00002/U/00001), Polish National Science Centre (NCN 2021/42/E/ST2/00350, NCN UMO-2019/34/E/ST2/00393, UMO-2020/37/B/ST2/01043, UMO-2021/40/C/ST2/00187); Slovenia: Slovenian Research Agency (ARIS grant J1-3010); Spain: BBVA Foundation (LEO22-1-603), Generalitat Valenciana (Artemisa, FEDER, IDIFEDER/2018/048), La Caixa Banking Foundation (LCF/BQ/PI20/11760025), Ministry of Science and Innovation (RYC2019-028510-I, RYC2020-030254-I), PROMETEO and GenT Programmes Generalitat Valenciana (CIDEGENT/2019/023, CIDEGENT/2019/027); Sweden: Swedish Research Council (VR 2022-03845), Knut and Alice Wallenberg Foundation (KAW 2017.0100, KAW 2018.0157, KAW 2019.0447); Switzerland: Swiss National Science Foundation (SNSF - PCEFP2_194658); United Kingdom: Leverhulme Trust (Leverhulme Trust RPG-2020-004); United States of America: Neubauer Family Foundation.

Open Access. This article is distributed under the terms of the Creative Commons Attribution License (CC-BY4.0), which permits any use, distribution and reproduction in any medium, provided the original author(s) and source are credited.

References

[1] ATLAS collaboration, *Measurement of the $t\bar{t}W$ and $t\bar{t}Z$ production cross sections in pp collisions at $\sqrt{s} = 8$ TeV with the ATLAS detector*, *JHEP* **11** (2015) 172 [arXiv:1509.05276] [INSPIRE].

[2] CMS collaboration, *Observation of top quark pairs produced in association with a vector boson in pp collisions at $\sqrt{s} = 8$ TeV*, *JHEP* **01** (2016) 096 [arXiv:1510.01131] [INSPIRE].

[3] ATLAS collaboration, *Search for new phenomena in events with same-charge leptons and b-jets in pp collisions at $\sqrt{s} = 13$ TeV with the ATLAS detector*, *JHEP* **12** (2018) 039 [arXiv:1807.11883] [INSPIRE].

[4] ATLAS collaboration, *Search for squarks and gluinos in final states with same-sign leptons and jets using 139 fb^{-1} of data collected with the ATLAS detector*, *JHEP* **06** (2020) 046 [arXiv:1909.08457] [INSPIRE].

[5] CMS collaboration, *Search for physics beyond the standard model in events with jets and two same-sign or at least three charged leptons in proton-proton collisions at $\sqrt{s} = 13$ TeV*, *Eur. Phys. J. C* **80** (2020) 752 [arXiv:2001.10086] [INSPIRE].

[6] ATLAS collaboration, *Measurement of the $t\bar{t}Z$ and $t\bar{t}W$ production cross sections in multilepton final states using 3.2 fb^{-1} of pp collisions at $\sqrt{s} = 13$ TeV with the ATLAS detector*, *Eur. Phys. J. C* **77** (2017) 40 [arXiv:1609.01599] [INSPIRE].

[7] ATLAS collaboration, *Measurement of the $t\bar{t}Z$ and $t\bar{t}W$ cross sections in proton-proton collisions at $\sqrt{s} = 13$ TeV with the ATLAS detector*, *Phys. Rev. D* **99** (2019) 072009 [arXiv:1901.03584] [INSPIRE].

[8] CMS collaboration, *Measurement of the cross section for top quark pair production in association with a W or Z boson in proton-proton collisions at $\sqrt{s} = 13$ TeV*, *JHEP* **08** (2018) 011 [arXiv:1711.02547] [INSPIRE].

[9] CMS collaboration, *Measurement of the cross section of top quark-antiquark pair production in association with a W boson in proton-proton collisions at $\sqrt{s} = 13$ TeV*, *JHEP* **07** (2023) 219 [arXiv:2208.06485] [INSPIRE].

JHEP05(2024)131

[10] CMS collaboration, *Measurement of the Higgs boson production rate in association with top quarks in final states with electrons, muons, and hadronically decaying tau leptons at* $\sqrt{s} = 13$ *TeV*, *Eur. Phys. J. C* **81** (2021) 378 [arXiv:2011.03652] [INSPIRE].

[11] ATLAS collaboration, *Observation of four-top-quark production in the multilepton final state with the ATLAS detector*, *Eur. Phys. J. C* **83** (2023) 496 [*Erratum ibid.* **84** (2024) 156] [arXiv:2303.15061] [INSPIRE].

[12] CMS collaboration, *Observation of four top quark production in proton-proton collisions at* $\sqrt{s} = 13$ *TeV*, *Phys. Lett. B* **847** (2023) 138290 [arXiv:2305.13439] [INSPIRE].

[13] J.A. Dror, M. Farina, E. Salvioni and J. Serra, *Strong tW scattering at the LHC*, *JHEP* **01** (2016) 071 [arXiv:1511.03674] [INSPIRE].

[14] F. Maltoni, L. Mantani and K. Mimasu, *Top-quark electroweak interactions at high energy*, *JHEP* **10** (2019) 004 [arXiv:1904.05637] [INSPIRE].

[15] L. Buonocore et al., *Precise predictions for the associated production of a W boson with a top-antitop quark pair at the LHC*, *Phys. Rev. Lett.* **131** (2023) 231901 [arXiv:2306.16311] [INSPIRE].

[16] LHC Higgs Cross Section Working Group collaboration, *Handbook of LHC Higgs cross sections: 4. Deciphering the nature of the Higgs sector*, arXiv:1610.07922 [DOI:10.23731/CYRM-2017-002] [INSPIRE].

[17] R. Frederix, D. Pagani and M. Zaro, *Large NLO corrections in* $t\bar{t}W^{\pm}$ *and* $t\bar{t}t\bar{t}$ *hadroproduction from supposedly subleading EW contributions*, *JHEP* **02** (2018) 031 [arXiv:1711.02116] [INSPIRE].

[18] A. Kulesza et al., *Associated production of a top quark pair with a heavy electroweak gauge boson at NLO+NNLL accuracy*, *Eur. Phys. J. C* **79** (2019) 249 [arXiv:1812.08622] [INSPIRE].

[19] A. Broggio et al., *Top-quark pair hadroproduction in association with a heavy boson at NLO+NNLL including EW corrections*, *JHEP* **08** (2019) 039 [arXiv:1907.04343] [INSPIRE].

[20] A. Kulesza et al., *Associated top quark pair production with a heavy boson: differential cross sections at NLO+NNLL accuracy*, *Eur. Phys. J. C* **80** (2020) 428 [arXiv:2001.03031] [INSPIRE].

[21] G. Bevilacqua et al., *The simplest of them all:* $t\bar{t}W^{\pm}$ *at NLO accuracy in QCD*, *JHEP* **08** (2020) 043 [arXiv:2005.09427] [INSPIRE].

[22] A. Denner and G. Pelliccioli, *NLO QCD corrections to off-shell* $t\bar{t}W^{\pm}$ *production at the LHC*, *JHEP* **11** (2020) 069 [arXiv:2007.12089] [INSPIRE].

[23] G. Bevilacqua et al., *NLO QCD corrections to off-shell* $t\bar{t}W^{\pm}$ *production at the LHC: correlations and asymmetries*, *Eur. Phys. J. C* **81** (2021) 675 [arXiv:2012.01363] [INSPIRE].

[24] F. Febres Cordero, M. Kraus and L. Reina, *Top-quark pair production in association with a* $W^{\pm}$ *gauge boson in the POWHEG-BOX*, *Phys. Rev. D* **103** (2021) 094014 [arXiv:2101.11808] [INSPIRE].

[25] A. Denner and G. Pelliccioli, *Combined NLO EW and QCD corrections to off-shell* $t\bar{t}W$ *production at the LHC*, *Eur. Phys. J. C* **81** (2021) 354 [arXiv:2102.03246] [INSPIRE].

[26] G. Bevilacqua et al., *Modeling uncertainties of* $t\bar{t}W^{\pm}$ *multilepton signatures*, *Phys. Rev. D* **105** (2022) 014018 [arXiv:2109.15181] [INSPIRE].

[27] R. Frederix and I. Tsinikos, *On improving NLO merging for* $t\bar{t}W$ *production*, *JHEP* **11** (2021) 029 [arXiv:2108.07826] [INSPIRE].

JHEP05(2024)131

[28] L. Ferencz et al., *Study of $t\bar{t}b\bar{b}$ and $t\bar{t}W$ background modelling for $t\bar{t}H$ analyses*, arXiv:2301.11670 [INSPIRE].

[29] ATLAS collaboration, *The ATLAS experiment at the CERN Large Hadron Collider*, 2008 *JINST* **3** S08003 [INSPIRE].

[30] ATLAS collaboration, *ATLAS Insertable B-Layer technical design report*, CERN-LHCC-2010-013, CERN, Geneva, Switzerland (2010).

[31] ATLAS IBL collaboration, *Production and integration of the ATLAS Insertable B-Layer*, 2018 *JINST* **13** T05008 [arXiv:1803.00844] [INSPIRE].

[32] ATLAS collaboration, *Performance of the ATLAS trigger system in* 2015, *Eur. Phys. J. C* **77** (2017) 317 [arXiv:1611.09661] [INSPIRE].

[33] ATLAS collaboration, *The ATLAS collaboration software and firmware*, ATL-SOFT-PUB-2021-001, CERN, Geneva, Switzerland (2021).

[34] ATLAS collaboration, *ATLAS data quality operations and performance for* 2015–2018 *data-taking*, 2020 *JINST* **15** P04003 [arXiv:1911.04632] [INSPIRE].

[35] F. Maltoni, M.L. Mangano, I. Tsinikos and M. Zaro, *Top-quark charge asymmetry and polarization in $t\bar{t}W^{\pm}$ production at the LHC*, *Phys. Lett. B* **736** (2014) 252 [arXiv:1406.3262] [INSPIRE].

[36] J.M. Campbell and R.K. Ellis, *$t\bar{t}W^{\pm}$ production and decay at NLO*, *JHEP* **07** (2012) 052 [arXiv:1204.5678] [INSPIRE].

[37] M.V. Garzelli, A. Kardos, C.G. Papadopoulos and Z. Trocsanyi, *$t\bar{t}W^{\pm}$ and $t\bar{t}Z$ hadroproduction at NLO accuracy in QCD with parton shower and hadronization effects*, *JHEP* **11** (2012) 056 [arXiv:1208.2665] [INSPIRE].

[38] F. Maltoni, D. Pagani and I. Tsinikos, *Associated production of a top-quark pair with vector bosons at NLO in QCD: impact on $t\bar{t}H$ searches at the LHC*, *JHEP* **02** (2016) 113 [arXiv:1507.05640] [INSPIRE].

[39] S. Frixione et al., *Electroweak and QCD corrections to top-pair hadroproduction in association with heavy bosons*, *JHEP* **06** (2015) 184 [arXiv:1504.03446] [INSPIRE].

[40] ATLAS collaboration, *The ATLAS simulation infrastructure*, *Eur. Phys. J. C* **70** (2010) 823 [arXiv:1005.4568] [INSPIRE].

[41] GEANT4 collaboration, *GEANT4 — a simulation toolkit*, *Nucl. Instrum. Meth. A* **506** (2003) 250 [INSPIRE].

[42] C. ATLAS et al., *The simulation principle and performance of the ATLAS fast calorimeter simulation FastCaloSim*, ATL-PHYS-PUB-2010-013, CERN, Geneva, Switzerland (2010).

[43] ATLAS collaboration, *The new fast calorimeter simulation in ATLAS*, ATL-SOFT-PUB-2018-002, CERN, Geneva, Switzerland (2018).

[44] T. Sjostrand, S. Mrenna and P.Z. Skands, *A brief introduction to PYTHIA* 8.1, *Comput. Phys. Commun.* **178** (2008) 852 [arXiv:0710.3820] [INSPIRE].

[45] ATLAS collaboration, *Further ATLAS tunes of PYTHIA*6 *and PYTHIA*8, ATL-PHYS-PUB-2011-014, CERN, Geneva, Switzerland (2011).

[46] SHERPA collaboration, *Event generation with SHERPA* 2.2, *SciPost Phys.* **7** (2019) 034 [arXiv:1905.09127] [INSPIRE].

JHEP05(2024)131

[47] T. Gleisberg et al., *Event generation with SHERPA 1.1*, *JHEP* **02** (2009) 007 [arXiv:0811.4622] [INSPIRE].

[48] NNPDF collaboration, *Parton distributions for the LHC run II*, *JHEP* **04** (2015) 040 [arXiv:1410.8849] [INSPIRE].

[49] T. Gleisberg and S. Hoeche, *Comix, a new matrix element generator*, *JHEP* **12** (2008) 039 [arXiv:0808.3674] [INSPIRE].

[50] F. Cascioli, P. Maierhofer and S. Pozzorini, *Scattering amplitudes with OpenLoops*, *Phys. Rev. Lett.* **108** (2012) 111601 [arXiv:1111.5206] [INSPIRE].

[51] A. Denner, S. Dittmaier and L. Hofer, *Collier: a fortran-based Complex One-Loop LIbrary in Extended Regularizations*, *Comput. Phys. Commun.* **212** (2017) 220 [arXiv:1604.06792] [INSPIRE].

[52] F. Buccioni et al., *OpenLoops 2*, *Eur. Phys. J. C* **79** (2019) 866 [arXiv:1907.13071] [INSPIRE].

[53] S. Schumann and F. Krauss, *A parton shower algorithm based on Catani-Seymour dipole factorisation*, *JHEP* **03** (2008) 038 [arXiv:0709.1027] [INSPIRE].

[54] S. Hoeche, F. Krauss, M. Schonherr and F. Siegert, *QCD matrix elements + parton showers: the NLO case*, *JHEP* **04** (2013) 027 [arXiv:1207.5030] [INSPIRE].

[55] S. Kallweit et al., *NLO QCD+EW predictions for V + jets including off-shell vector-boson decays and multijet merging*, *JHEP* **04** (2016) 021 [arXiv:1511.08692] [INSPIRE].

[56] C. Gütschow, J.M. Lindert and M. Schönherr, *Multi-jet merged top-pair production including electroweak corrections*, *Eur. Phys. J. C* **78** (2018) 317 [arXiv:1803.00950] [INSPIRE].

[57] J. Alwall et al., *The automated computation of tree-level and next-to-leading order differential cross sections, and their matching to parton shower simulations*, *JHEP* **07** (2014) 079 [arXiv:1405.0301] [INSPIRE].

[58] NNPDF collaboration, *Parton distributions from high-precision collider data*, *Eur. Phys. J. C* **77** (2017) 663 [arXiv:1706.00428] [INSPIRE].

[59] ATLAS collaboration, *ATLAS PYTHIA8 tunes to 7 TeV data*, ATL-PHYS-PUB-2014-021, CERN, Geneva, Switzerland (2014).

[60] D.J. Lange, *The EvtGen particle decay simulation package*, *Nucl. Instrum. Meth. A* **462** (2001) 152 [INSPIRE].

[61] R. Frederix and S. Frixione, *Merging meets matching in MC@NLO*, *JHEP* **12** (2012) 061 [arXiv:1209.6215] [INSPIRE].

[62] S. Frixione, E. Laenen, P. Motylinski and B.R. Webber, *Angular correlations of lepton pairs from vector boson and top quark decays in Monte Carlo simulations*, *JHEP* **04** (2007) 081 [hep-ph/0702198] [INSPIRE].

[63] P. Artoisenet, R. Frederix, O. Mattelaer and R. Rietkerk, *Automatic spin-entangled decays of heavy resonances in Monte Carlo simulations*, *JHEP* **03** (2013) 015 [arXiv:1212.3460] [INSPIRE].

[64] S. Frixione, P. Nason and G. Ridolfi, *A positive-weight next-to-leading-order Monte Carlo for heavy flavour hadroproduction*, *JHEP* **09** (2007) 126 [arXiv:0707.3088] [INSPIRE].

[65] P. Nason, *A new method for combining NLO QCD with shower Monte Carlo algorithms*, *JHEP* **11** (2004) 040 [hep-ph/0409146] [INSPIRE].

JHEP05(2024)131

[66] S. Frixione, P. Nason and C. Oleari, *Matching NLO QCD computations with parton shower simulations: the POWHEG method*, *JHEP* **11** (2007) 070 [arXiv:0709.2092] [INSPIRE].

[67] S. Alioli, P. Nason, C. Oleari and E. Re, *A general framework for implementing NLO calculations in shower Monte Carlo programs: the POWHEG BOX*, *JHEP* **06** (2010) 043 [arXiv:1002.2581] [INSPIRE].

[68] H.B. Hartanto, B. Jager, L. Reina and D. Wackeroth, *Higgs boson production in association with top quarks in the POWHEG BOX*, *Phys. Rev. D* **91** (2015) 094003 [arXiv:1501.04498] [INSPIRE].

[69] M. Bahr et al., *Herwig++ physics and manual*, *Eur. Phys. J. C* **58** (2008) 639 [arXiv:0803.0883] [INSPIRE].

[70] J. Bellm et al., *Herwig* 7.0/*Herwig++* 3.0 *release note*, *Eur. Phys. J. C* **76** (2016) 196 [arXiv:1512.01178] [INSPIRE].

[71] E. Re, *Single-top Wt-channel production matched with parton showers using the POWHEG method*, *Eur. Phys. J. C* **71** (2011) 1547 [arXiv:1009.2450] [INSPIRE].

[72] R. Frederix, E. Re and P. Torrielli, *Single-top t-channel hadroproduction in the four-flavour scheme with POWHEG and aMC@NLO*, *JHEP* **09** (2012) 130 [arXiv:1207.5391] [INSPIRE].

[73] S. Alioli, P. Nason, C. Oleari and E. Re, *NLO single-top production matched with shower in POWHEG: s- and t-channel contributions*, *JHEP* **09** (2009) 111 [*Erratum ibid.* **02** (2010) 011] [arXiv:0907.4076] [INSPIRE].

[74] ATLAS collaboration, *Studies on top-quark Monte Carlo modelling for Top*2016, ATL-PHYS-PUB-2016-020, CERN, Geneva, Switzerland (2016).

[75] S. Frixione et al., *Single-top hadroproduction in association with a W boson*, *JHEP* **07** (2008) 029 [arXiv:0805.3067] [INSPIRE].

[76] M. Beneke, P. Falgari, S. Klein and C. Schwinn, *Hadronic top-quark pair production with NNLL threshold resummation*, *Nucl. Phys. B* **855** (2012) 695 [arXiv:1109.1536] [INSPIRE].

[77] M. Cacciari et al., *Top-pair production at hadron colliders with next-to-next-to-leading logarithmic soft-gluon resummation*, *Phys. Lett. B* **710** (2012) 612 [arXiv:1111.5869] [INSPIRE].

[78] P. Bärnreuther, M. Czakon and A. Mitov, *Percent level precision physics at the Tevatron: first genuine NNLO QCD corrections to* $q\bar{q} \to t\bar{t} + X$, *Phys. Rev. Lett.* **109** (2012) 132001 [arXiv:1204.5201] [INSPIRE].

[79] M. Czakon and A. Mitov, *NNLO corrections to top-pair production at hadron colliders: the all-fermionic scattering channels*, *JHEP* **12** (2012) 054 [arXiv:1207.0236] [INSPIRE].

[80] M. Czakon and A. Mitov, *NNLO corrections to top pair production at hadron colliders: the quark-gluon reaction*, *JHEP* **01** (2013) 080 [arXiv:1210.6832] [INSPIRE].

[81] M. Czakon, P. Fiedler and A. Mitov, *Total top-quark pair-production cross section at hadron colliders through* $O(\alpha_S^4)$, *Phys. Rev. Lett.* **110** (2013) 252004 [arXiv:1303.6254] [INSPIRE].

[82] M. Czakon and A. Mitov, *Top++: a program for the calculation of the top-pair cross-section at hadron colliders*, *Comput. Phys. Commun.* **185** (2014) 2930 [arXiv:1112.5675] [INSPIRE].

[83] N. Kidonakis, *Two-loop soft anomalous dimensions for single top quark associated production with a* W^- *or* H^-, *Phys. Rev. D* **82** (2010) 054018 [arXiv:1005.4451] [INSPIRE].

JHEP05(2024)131

[84] N. Kidonakis, *Top quark production*, in the proceedings of the *Helmholtz International Summer School on Physics of Heavy Quarks and Hadrons*, (2014) [DOI:10.3204/DESY-PROC-2013-03/Kidonakis] [arXiv:1311.0283] [INSPIRE].

[85] M. Aliev et al., *HATHOR: HAdronic Top and Heavy quarks crOss section calculatoR*, *Comput. Phys. Commun.* **182** (2011) 1034 [arXiv:1007.1327] [INSPIRE].

[86] P. Kant et al., *HatHor for single top-quark production: updated predictions and uncertainty estimates for single top-quark production in hadronic collisions*, *Comput. Phys. Commun.* **191** (2015) 74 [arXiv:1406.4403] [INSPIRE].

[87] M. van Beekveld, A. Kulesza and L.M. Valero, *Threshold resummation for the production of four top quarks at the LHC*, *Phys. Rev. Lett.* **131** (2023) 211901 [arXiv:2212.03259] [INSPIRE].

[88] ATLAS collaboration, *Measurements of WH and ZH production in the $H \to b\bar{b}$ decay channel in pp collisions at* 13 *TeV with the ATLAS detector*, *Eur. Phys. J. C* **81** (2021) 178 [arXiv:2007.02873] [INSPIRE].

[89] ATLAS collaboration, *Vertex reconstruction performance of the ATLAS detector at $\sqrt{s} = 13$ TeV*, ATL-PHYS-PUB-2015-026, CERN, Geneva, Switzerland (2015).

[90] ATLAS collaboration, *Electron and photon performance measurements with the ATLAS detector using the* 2015–2017 *LHC proton-proton collision data*, 2019 *JINST* **14** P12006 [arXiv:1908.00005] [INSPIRE].

[91] ATLAS collaboration, *Muon reconstruction and identification efficiency in ATLAS using the full run* 2 *pp collision data set at $\sqrt{s} = 13$ TeV*, *Eur. Phys. J. C* **81** (2021) 578 [arXiv:2012.00578] [INSPIRE].

[92] ATLAS collaboration, *Evidence for the associated production of the Higgs boson and a top quark pair with the ATLAS detector*, *Phys. Rev. D* **97** (2018) 072003 [arXiv:1712.08891] [INSPIRE].

[93] ATLAS collaboration, *Electron reconstruction and identification in the ATLAS experiment using the* 2015 *and* 2016 *LHC proton-proton collision data at $\sqrt{s} = 13$ TeV*, *Eur. Phys. J. C* **79** (2019) 639 [arXiv:1902.04655] [INSPIRE].

[94] ATLAS collaboration, *Jet reconstruction and performance using particle flow with the ATLAS detector*, *Eur. Phys. J. C* **77** (2017) 466 [arXiv:1703.10485] [INSPIRE].

[95] M. Cacciari, G.P. Salam and G. Soyez, *The anti-k_t jet clustering algorithm*, *JHEP* **04** (2008) 063 [arXiv:0802.1189] [INSPIRE].

[96] M. Cacciari, G.P. Salam and G. Soyez, *FastJet user manual*, *Eur. Phys. J. C* **72** (2012) 1896 [arXiv:1111.6097] [INSPIRE].

[97] ATLAS collaboration, *Jet energy scale and resolution measured in proton-proton collisions at $\sqrt{s} = 13$ TeV with the ATLAS detector*, *Eur. Phys. J. C* **81** (2021) 689 [arXiv:2007.02645] [INSPIRE].

[98] ATLAS collaboration, *Performance of pile-up mitigation techniques for jets in pp collisions at $\sqrt{s} = 8$ TeV using the ATLAS detector*, *Eur. Phys. J. C* **76** (2016) 581 [arXiv:1510.03823] [INSPIRE].

[99] ATLAS collaboration, *Selection of jets produced in* 13 *TeV proton-proton collisions with the ATLAS detector*, ATLAS-CONF-2015-029, CERN, Geneva, Switzerland (2015).

[100] ATLAS collaboration, *ATLAS flavour-tagging algorithms for the LHC run* 2 *pp collision dataset*, *Eur. Phys. J. C* **83** (2023) 681 [arXiv:2211.16345] [INSPIRE].

JHEP05(2024)131

[101] ATLAS collaboration, *Identification of jets containing b-hadrons with recurrent neural networks at the ATLAS experiment*, ATL-PHYS-PUB-2017-003, CERN, Geneva, Switzerland (2017).

[102] ATLAS collaboration, *ATLAS b-jet identification performance and efficiency measurement with $t\bar{t}$ events in pp collisions at $\sqrt{s} = 13$ TeV*, *Eur. Phys. J. C* **79** (2019) 970 [arXiv:1907.05120] [INSPIRE].

[103] ATLAS collaboration, *Measurement of the c-jet mistagging efficiency in $t\bar{t}$ events using pp collision data at $\sqrt{s} = 13$ TeV collected with the ATLAS detector*, *Eur. Phys. J. C* **82** (2022) 95 [arXiv:2109.10627] [INSPIRE].

[104] ATLAS collaboration, *Calibration of the light-flavour jet mistagging efficiency of the b-tagging algorithms with Z+jets events using 139 fb^{-1} of ATLAS proton-proton collision data at $\sqrt{s} = 13$ TeV*, *Eur. Phys. J. C* **83** (2023) 728 [arXiv:2301.06319] [INSPIRE].

[105] M. Cacciari, G.P. Salam and G. Soyez, *The catchment area of jets*, *JHEP* **04** (2008) 005 [arXiv:0802.1188] [INSPIRE].

[106] ATLAS collaboration, *Performance of missing transverse momentum reconstruction with the ATLAS detector using proton-proton collisions at $\sqrt{s} = 13$ TeV*, *Eur. Phys. J. C* **78** (2018) 903 [arXiv:1802.08168] [INSPIRE].

[107] ATLAS collaboration, *Performance of the ATLAS muon triggers in run* 2, 2020 *JINST* **15** P09015 [arXiv:2004.13447] [INSPIRE].

[108] ATLAS collaboration, *Performance of electron and photon triggers in ATLAS during LHC run* 2, *Eur. Phys. J. C* **80** (2020) 47 [arXiv:1909.00761] [INSPIRE].

[109] ATLAS collaboration, *Measurement of Higgs boson decay into b-quarks in associated production with a top-quark pair in pp collisions at $\sqrt{s} = 13$ TeV with the ATLAS detector*, *JHEP* **06** (2022) 097 [arXiv:2111.06712] [INSPIRE].

[110] ATLAS collaboration, *Muon reconstruction performance of the ATLAS detector in proton-proton collision data at $\sqrt{s} = 13$ TeV*, *Eur. Phys. J. C* **76** (2016) 292 [arXiv:1603.05598] [INSPIRE].

[111] ATLAS collaboration, *Studies of the muon momentum calibration and performance of the ATLAS detector with pp collisions at $\sqrt{s} = 13$ TeV*, *Eur. Phys. J. C* **83** (2023) 686 [arXiv:2212.07338] [INSPIRE].

[112] ATLAS collaboration, *Luminosity determination in pp collisions at $\sqrt{s} = 13$ TeV using the ATLAS detector at the LHC*, *Eur. Phys. J. C* **83** (2023) 982 [arXiv:2212.09379] [INSPIRE].

[113] G. Avoni et al., *The new LUCID-2 detector for luminosity measurement and monitoring in ATLAS*, 2018 *JINST* **13** P07017 [INSPIRE].

[114] ROOT collaboration, *HistFactory: a tool for creating statistical models for use with RooFit and RooStats*, CERN-OPEN-2012-016, New York U., New York, NY, U.S.A. (2012) [DOI:10.17181/CERN-OPEN-2012-016].

[115] R.J. Barlow and C. Beeston, *Fitting using finite Monte Carlo samples*, *Comput. Phys. Commun.* **77** (1993) 219 [INSPIRE].

[116] V. Blobel, *An unfolding method for high-energy physics experiments*, in the proceedings of the *Conference on Advanced Statistical Techniques in Particle Physics*, (2002) [hep-ex/0208022] [INSPIRE].

[117] D.L. Phillips, *A technique for the numerical solution of certain integral equations of the first kind*, *J. Assoc. Comput. Machinery* **9** (1962) 84 [INSPIRE].

JHEP05(2024)131

[118] A.N. Tikhonov, *On the solution of improperly posed problems and the method of regularization*, *Sov. Math.* **5** (1963) 1035.

[119] R.A. Willoughby, *Solutions of ill-posed problems (A.N. Tikhonov and V.Y. Arsenin)*, *SIAM Review* **21** (1979) 266.

[120] G. Cowan, *Statistical data analysis*, (1998).

[121] S. Schmitt, *Data unfolding methods in high energy physics*, *EPJ Web Conf.* **137** (2017) 11008 [arXiv:1611.01927] [INSPIRE].

[122] G. Cowan, K. Cranmer, E. Gross and O. Vitells, *Asymptotic formulae for likelihood-based tests of new physics*, *Eur. Phys. J. C* **71** (2011) 1554 [*Erratum ibid.* **73** (2013) 2501] [arXiv:1007.1727] [INSPIRE].

[123] ATLAS collaboration, *ATLAS computing acknowledgements*, ATL-SOFT-PUB-2023-001, CERN, Geneva, Switzerland (2023).

JHEP05(2024)131

The ATLAS collaboration

G. Aad[102], B. Abbott[120], K. Abeling[55], N.J. Abicht[49], S.H. Abidi[29], A. Aboulhorma[35e], H. Abramowicz[151], H. Abreu[150], Y. Abulaiti[117], A.C. Abusleme Hoffman[137a], B.S. Acharya[69a,69b,n], C. Adam Bourdarios[4], L. Adamczyk[86a], L. Adamek[155], S.V. Addepalli[26], M.J. Addison[101], J. Adelman[115], A. Adiguzel[21c], T. Adye[134], A.A. Affolder[136], Y. Afik[36], M.N. Agaras[13], J. Agarwala[73a,73b], A. Aggarwal[100], C. Agheorghiesei[27c], A. Ahmad[36], F. Ahmadov[38,z], W.S. Ahmed[104], S. Ahuja[95], X. Ai[62a], G. Aielli[76a,76b], M. Ait Tamlihat[35e], B. Aitbenchikh[35a], I. Aizenberg[169], M. Akbiyik[100], T.P.A. Åkesson[98], A.V. Akimov[37], D. Akiyama[168], N.N. Akolkar[24], K. Al Khoury[41], G.L. Alberghi[23b], J. Albert[165], P. Albicocco[53], G.L. Albouy[60], S. Alderweireldt[52], M. Aleksa[36], I.N. Aleksandrov[38], C. Alexa[27b], T. Alexopoulos[10], A. Alfonsi[114], F. Alfonsi[23b], M. Algren[56], M. Alhroob[120], B. Ali[132], H.M.J. Ali[91], S. Ali[148], S.W. Alibocus[92], M. Aliev[37], G. Alimonti[71a], W. Alkakhi[55], C. Allaire[66], B.M.M. Allbrooke[146], J.F. Allen[52], C.A. Allendes Flores[137f], P.P. Allport[20], A. Aloisio[72a,72b], F. Alonso[90], C. Alpigiani[138], M. Alvarez Estevez[99], A. Alvarez Fernandez[100], M.G. Alviggi[72a,72b], M. Aly[101], Y. Amaral Coutinho[83b], A. Ambler[104], C. Amelung[36], M. Amerl[101], C.G. Ames[109], D. Amidei[106], S.P. Amor Dos Santos[130a], K.R. Amos[163], V. Ananiev[125], C. Anastopoulos[139], T. Andeen[11], J.K. Anders[36], S.Y. Andrean[47a,47b], A. Andreazza[71a,71b], S. Angelidakis[9], A. Angerami[41,ac], A.V. Anisenkov[37], A. Annovi[74a], C. Antel[56], M.T. Anthony[139], E. Antipov[145], M. Antonelli[53], D.J.A. Antrim[17a], F. Anulli[75a], M. Aoki[84], T. Aoki[153], J.A. Aparisi Pozo[163], M.A. Aparo[146], L. Aperio Bella[48], C. Appelt[18], A. Apyan[26], N. Aranzabal[36], C. Arcangeletti[53], A.T.H. Arce[51], E. Arena[92], J-F. Arguin[108], S. Argyropoulos[54], J.-H. Arling[48], A.J. Armbruster[36], O. Arnaez[4], H. Arnold[114], Z.P. Arrubarrena Tame[109], G. Artoni[75a,75b], H. Asada[111], K. Asai[118], S. Asai[153], N.A. Asbah[61], K. Assamagan[29], R. Astalos[28a], S. Atashi[160], R.J. Atkin[33a], M. Atkinson[162], N.B. Atlay[18], H. Atmani[62b], P.A. Atmasiddha[106], K. Augsten[132], S. Auricchio[72a,72b], A.D. Auriol[20], V.A. Austrup[101], G. Avolio[36], K. Axiotis[56], G. Azuelos[108,ag], D. Babal[28b], H. Bachacou[135], K. Bachas[152,q], A. Bachiu[34], F. Backman[47a,47b], A. Badea[61], P. Bagnaia[75a,75b], M. Bahmani[18], A.J. Bailey[163], V.R. Bailey[162], J.T. Baines[134], L. Baines[94], C. Bakalis[10], O.K. Baker[172], E. Bakos[15], D. Bakshi Gupta[8], R. Balasubramanian[114], E.M. Baldin[37], P. Balek[86a], E. Ballabene[23b,23a], F. Balli[135], L.M. Baltes[63a], W.K. Balunas[32], J. Balz[100], E. Banas[87], M. Bandieramonte[129], A. Bandyopadhyay[24], S. Bansal[24], L. Barak[151], M. Barakat[48], E.L. Barberio[105], D. Barberis[57b,57a], M. Barbero[102], G. Barbour[96], K.N. Barends[33a], T. Barillari[110], M-S. Barisits[36], T. Barklow[143], P. Baron[122], D.A. Baron Moreno[101], A. Baroncelli[62a], G. Barone[29], A.J. Barr[126], J.D. Barr[96], L. Barranco Navarro[47a,47b], F. Barreiro[99], J. Barreiro Guimarães da Costa[14a], U. Barron[151], M.G. Barros Teixeira[130a], S. Barsov[37], F. Bartels[63a], R. Bartoldus[143], A.E. Barton[91], P. Bartos[28a], A. Basan[100], M. Baselga[49], A. Bassalat[66,b], M.J. Basso[156a], C.R. Basson[101], R.L. Bates[59], S. Batlamous[35e], J.R. Batley[32], B. Batool[141], M. Battaglia[136], D. Battulga[18], M. Bauce[75a,75b], M. Bauer[36], P. Bauer[24], L.T. Bazzano Hurrell[30], J.B. Beacham[51], T. Beau[127], P.H. Beauchemin[158], F. Becherer[54], P. Bechtle[24], H.P. Beck[19,p],

JHEP05(2024)131

K. Becker[167], A.J. Beddall[82], V.A. Bednyakov[38], C.P. Bee[145], L.J. Beemster[15], T.A. Beermann[36], M. Begalli[83d], M. Begel[29], A. Behera[145], J.K. Behr[48], J.F. Beirer[55], F. Beisiegel[24], M. Belfkir[159], G. Bella[151], L. Bellagamba[23b], A. Bellerive[34], P. Bellos[20], K. Beloborodov[37], N.L. Belyaev[37], D. Benchekroun[35a], F. Bendebba[35a], Y. Benhammou[151], M. Benoit[29], J.R. Bensinger[26], S. Bentvelsen[114], L. Beresford[48], M. Beretta[53], E. Bergeaas Kuutmann[161], N. Berger[4], B. Bergmann[132], J. Beringer[17a], G. Bernardi[5], C. Bernius[143], F.U. Bernlochner[24], F. Bernon[36,102], T. Berry[95], P. Berta[133], A. Berthold[50], I.A. Bertram[91], S. Bethke[110], A. Betti[75a,75b], A.J. Bevan[94], M. Bhamjee[33c], S. Bhatta[145], D.S. Bhattacharya[166], P. Bhattarai[26], V.S. Bhopatkar[121], R. Bi[29,ai], R.M. Bianchi[129], G. Bianco[23b,23a], O. Biebel[109], R. Bielski[123], M. Biglietti[77a], T.R.V. Billoud[132], M. Bindi[55], A. Bingul[21b], C. Bini[75a,75b], A. Biondini[92], C.J. Birch-sykes[101], G.A. Bird[20,134], M. Birman[169], M. Biros[133], T. Bisanz[49], E. Bisceglie[43b,43a], D. Biswas[141], A. Bitadze[101], K. Bjørke[125], I. Bloch[48], C. Blocker[26], A. Blue[59], U. Blumenschein[94], J. Blumenthal[100], G.J. Bobbink[114], V.S. Bobrovnikov[37], M. Boehler[54], B. Boehm[166], D. Bogavac[36], A.G. Bogdanchikov[37], C. Bohm[47a], V. Boisvert[95], P. Bokan[48], T. Bold[86a], M. Bomben[5], M. Bona[94], M. Boonekamp[135], C.D. Booth[95], A.G. Borbély[59], I.S. Bordulev[37], H.M. Borecka-Bielska[108], L.S. Borgna[96], G. Borissov[91], D. Bortoletto[126], D. Boscherini[23b], M. Bosman[13], J.D. Bossio Sola[36], K. Bouaouda[35a], N. Bouchhar[163], J. Boudreau[129], E.V. Bouhova-Thacker[91], D. Boumediene[40], R. Bouquet[5], A. Boveia[119], J. Boyd[36], D. Boye[29], I.R. Boyko[38], J. Bracinik[20], N. Brahimi[62d], G. Brandt[171], O. Brandt[32], F. Braren[48], B. Brau[103], J.E. Brau[123], R. Brener[169], L. Brenner[114], R. Brenner[161], S. Bressler[169], D. Britton[59], D. Britzger[110], I. Brock[24], G. Brooijmans[41], W.K. Brooks[137f], E. Brost[29], L.M. Brown[165], L.E. Bruce[61], T.L. Bruckler[126], P.A. Bruckman de Renstrom[87], B. Brüers[48], D. Bruncko[28b,*], A. Bruni[23b], G. Bruni[23b], M. Bruschi[23b], N. Bruscino[75a,75b], T. Buanes[16], Q. Buat[138], D. Buchin[110], A.G. Buckley[59], M.K. Bugge[125], O. Bulekov[37], B.A. Bullard[143], S. Burdin[92], C.D. Burgard[49], A.M. Burger[40], B. Burghgrave[8], O. Burlayenko[54], J.T.P. Burr[32], C.D. Burton[11], J.C. Burzynski[142], E.L. Busch[41], V. Büscher[100], P.J. Bussey[59], J.M. Butler[25], C.M. Buttar[59], J.M. Butterworth[96], W. Buttinger[134], C.J. Buxo Vazquez[107], A.R. Buzykaev[37], G. Cabras[23b], S. Cabrera Urbán[163], L. Cadamuro[66], D. Caforio[58], H. Cai[129], Y. Cai[14a,14e], V.M.M. Cairo[36], O. Cakir[3a], N. Calace[36], P. Calafiura[17a], G. Calderini[127], P. Calfayan[68], G. Callea[59], L.P. Caloba[83b], D. Calvet[40], S. Calvet[40], T.P. Calvet[102], M. Calvetti[74a,74b], R. Camacho Toro[127], S. Camarda[36], D. Camarero Munoz[26], P. Camarri[76a,76b], M.T. Camerlingo[72a,72b], D. Cameron[125], C. Camincher[165], M. Campanelli[96], A. Camplani[42], V. Canale[72a,72b], A. Canesse[104], M. Cano Bret[80], J. Cantero[163], Y. Cao[162], F. Capocasa[26], M. Capua[43b,43a], A. Carbone[71a,71b], R. Cardarelli[76a], J.C.J. Cardenas[8], F. Cardillo[163], T. Carli[36], G. Carlino[72a], J.I. Carlotto[13], B.T. Carlson[129,r], E.M. Carlson[165,156a], L. Carminati[71a,71b], A. Carnelli[135], M. Carnesale[75a,75b], S. Caron[113], E. Carquin[137f], S. Carrá[71a], G. Carratta[23b,23a], F. Carrio Argos[33g], J.W.S. Carter[155], T.M. Carter[52], M.P. Casado[13,i], M. Caspar[48], E.G. Castiglia[172], F.L. Castillo[4], L. Castillo Garcia[13], V. Castillo Gimenez[163], N.F. Castro[130a,130e], A. Catinaccio[36], J.R. Catmore[125],

JHEP05(2024)131

V. Cavaliere[29], N. Cavalli[23b,23a], V. Cavasinni[74a,74b], Y.C. Cekmecelioglu[48], E. Celebi[21a], F. Celli[126], M.S. Centonze[70a,70b], K. Cerny[122], A.S. Cerqueira[83a], A. Cerri[146], L. Cerrito[76a,76b], F. Cerutti[17a], B. Cervato[141], A. Cervelli[23b], G. Cesarini[53], S.A. Cetin[82], Z. Chadi[35a], D. Chakraborty[115], M. Chala[130f], J. Chan[170], W.Y. Chan[153], J.D. Chapman[32], E. Chapon[135], B. Chargeishvili[149b], D.G. Charlton[20], T.P. Charman[94], M. Chatterjee[19], C. Chauhan[133], S. Chekanov[6], S.V. Chekulaev[156a], G.A. Chelkov[38,a], A. Chen[106], B. Chen[151], B. Chen[165], H. Chen[14c], H. Chen[29], J. Chen[62c], J. Chen[142], M. Chen[126], S. Chen[153], S.J. Chen[14c], X. Chen[62c], X. Chen[14b,af], Y. Chen[62a], C.L. Cheng[170], H.C. Cheng[64a], S. Cheong[143], A. Cheplakov[38], E. Cheremushkina[48], E. Cherepanova[114], R. Cherkaoui El Moursli[35e], E. Cheu[7], K. Cheung[65], L. Chevalier[135], V. Chiarella[53], G. Chiarelli[74a], N. Chiedde[102], G. Chiodini[70a], A.S. Chisholm[20], A. Chitan[27b], M. Chitishvili[163], M.V. Chizhov[38], K. Choi[11], A.R. Chomont[75a,75b], Y. Chou[103], E.Y.S. Chow[114], T. Chowdhury[33g], K.L. Chu[169], M.C. Chu[64a], X. Chu[14a,14e], J. Chudoba[131], J.J. Chwastowski[87], D. Cieri[110], K.M. Ciesla[86a], V. Cindro[93], A. Ciocio[17a], F. Cirotto[72a,72b], Z.H. Citron[169,l], M. Citterio[71a], D.A. Ciubotaru[27b], B.M. Ciungu[155], A. Clark[56], P.J. Clark[52], J.M. Clavijo Columbie[48], S.E. Clawson[48], C. Clement[47a,47b], J. Clercx[48], Y. Coadou[102], M. Cobal[69a,69c], A. Coccaro[57b], R.F. Coelho Barrue[130a], R. Coelho Lopes De Sa[103], S. Coelli[71a], H. Cohen[151], A.E.C. Coimbra[71a,71b], B. Cole[41], J. Collot[60], P. Conde Muiño[130a,130g], M.P. Connell[33c], S.H. Connell[33c], I.A. Connelly[59], E.I. Conroy[126], F. Conventi[72a,ah], H.G. Cooke[20], A.M. Cooper-Sarkar[126], A. Cordeiro Oudot Choi[127], F. Cormier[164], L.D. Corpe[40], M. Corradi[75a,75b], F. Corriveau[104,x], A. Cortes-Gonzalez[18], M.J. Costa[163], F. Costanza[4], D. Costanzo[139], B.M. Cote[119], G. Cowan[95], K. Cranmer[170], D. Cremonini[23b,23a], S. Crépé-Renaudin[60], F. Crescioli[127], M. Cristinziani[141], M. Cristoforetti[78a,78b], V. Croft[114], J.E. Crosby[121], G. Crosetti[43b,43a], A. Cueto[99], T. Cuhadar Donszelmann[160], H. Cui[14a,14e], Z. Cui[7], W.R. Cunningham[59], F. Curcio[43b,43a], P. Czodrowski[36], M.M. Czurylo[63b], M.J. Da Cunha Sargedas De Sousa[62a], J.V. Da Fonseca Pinto[83b], C. Da Via[101], W. Dabrowski[86a], T. Dado[49], S. Dahbi[33g], T. Dai[106], C. Dallapiccola[103], M. Dam[42], G. D'amen[29], V. D'Amico[109], J. Damp[100], J.R. Dandoy[128], M.F. Daneri[30], M. Danninger[142], V. Dao[36], G. Darbo[57b], S. Darmora[6], S.J. Das[29,ai], S. D'Auria[71a,71b], C. David[156b], T. Davidek[133], B. Davis-Purcell[34], I. Dawson[94], H.A. Day-hall[132], K. De[8], R. De Asmundis[72a], N. De Biase[48], S. De Castro[23b,23a], N. De Groot[113], P. de Jong[114], H. De la Torre[107], A. De Maria[14c], A. De Salvo[75a], U. De Sanctis[76a,76b], A. De Santo[146], J.B. De Vivie De Regie[60], D.V. Dedovich[38], J. Degens[114], A.M. Deiana[44], F. Del Corso[23b,23a], J. Del Peso[99], F. Del Rio[63a], F. Deliot[135], C.M. Delitzsch[49], M. Della Pietra[72a,72b], D. Della Volpe[56], A. Dell'Acqua[36], L. Dell'Asta[71a,71b], M. Delmastro[4], P.A. Delsart[60], S. Demers[172], M. Demichev[38], S.P. Denisov[37], L. D'Eramo[40], D. Derendarz[87], F. Derue[127], P. Dervan[92], K. Desch[24], C. Deutsch[24], F.A. Di Bello[57b,57a], A. Di Ciaccio[76a,76b], L. Di Ciaccio[4], A. Di Domenico[75a,75b], C. Di Donato[72a,72b], A. Di Girolamo[36], G. Di Gregorio[5], A. Di Luca[78a,78b], B. Di Micco[77a,77b], R. Di Nardo[77a,77b], C. Diaconu[102], F.A. Dias[114], T. Dias Do Vale[142], M.A. Diaz[137a,137b], F.G. Diaz Capriles[24], M. Didenko[163], E.B. Diehl[106], L. Diehl[54], S. Díez Cornell[48], C. Diez Pardos[141], C. Dimitriadi[24,161],

JHEP05(2024)131

A. Dimitrievska[17a], J. Dingfelder[24], I-M. Dinu[27b], S.J. Dittmeier[63b], F. Dittus[36], F. Djama[102], T. Djobava[149b], J.I. Djuvsland[16], C. Doglioni[101,98], J. Dolejsi[133], Z. Dolezal[133], M. Donadelli[83c], B. Dong[107], J. Donini[40], A. D'Onofrio[77a,77b], M. D'Onofrio[92], J. Dopke[134], A. Doria[72a], N. Dos Santos Fernandes[130a], M.T. Dova[90], A.T. Doyle[59], M.A. Draguet[126], E. Dreyer[169], I. Drivas-koulouris[10], A.S. Drobac[158], M. Drozdova[56], D. Du[62a], T.A. du Pree[114], F. Dubinin[37], M. Dubovsky[28a], E. Duchovni[169], G. Duckeck[109], O.A. Ducu[27b], D. Duda[52], A. Dudarev[36], E.R. Duden[26], M. D'uffizi[101], L. Duflot[66], M. Dührssen[36], C. Dülsen[171], A.E. Dumitriu[27b], M. Dunford[63a], S. Dungs[49], K. Dunne[47a,47b], A. Duperrin[102], H. Duran Yildiz[3a], M. Düren[58], A. Durglishvili[149b], B.L. Dwyer[115], G.I. Dyckes[17a], M. Dyndal[86a], S. Dysch[101], B.S. Dziedzic[87], Z.O. Earnshaw[146], G.H. Eberwein[126], B. Eckerova[28a], S. Eggebrecht[55], M.G. Eggleston[51], E. Egidio Purcino De Souza[127], L.F. Ehrke[56], G. Eigen[16], K. Einsweiler[17a], T. Ekelof[161], P.A. Ekman[98], S. El Farkh[35b], Y. El Ghazali[35b], H. El Jarrari[35e,148], A. El Moussaouy[35a], V. Ellajosyula[161], M. Ellert[161], F. Ellinghaus[171], A.A. Elliot[94], N. Ellis[36], J. Elmsheuser[29], M. Elsing[36], D. Emeliyanov[134], Y. Enari[153], I. Ene[17a], S. Epari[13], J. Erdmann[49], P.A. Erland[87], M. Errenst[171], M. Escalier[66], C. Escobar[163], E. Etzion[151], G. Evans[130a], H. Evans[68], L.S. Evans[95], M.O. Evans[146], A. Ezhilov[37], S. Ezzarqtouni[35a], F. Fabbri[59], L. Fabbri[23b,23a], G. Facini[96], V. Fadeyev[136], R.M. Fakhrutdinov[37], S. Falciano[75a], L.F. Falda Ulhoa Coelho[36], P.J. Falke[24], J. Faltova[133], C. Fan[162], Y. Fan[14a], Y. Fang[14a,14e], M. Fanti[71a,71b], M. Faraj[69a,69b], Z. Farazpay[97], A. Farbin[8], A. Farilla[77a], T. Farooque[107], S.M. Farrington[52], F. Fassi[35e], D. Fassouliotis[9], M. Faucci Giannelli[76a,76b], W.J. Fawcett[32], L. Fayard[66], P. Federic[133], P. Federicova[131], O.L. Fedin[37,a], G. Fedotov[37], M. Feickert[170], L. Feligioni[102], D.E. Fellers[123], C. Feng[62b], M. Feng[14b], Z. Feng[114], M.J. Fenton[160], A.B. Fenyuk[37], L. Ferencz[48], R.A.M. Ferguson[91], S.I. Fernandez Luengo[137f], M.J.V. Fernoux[102], J. Ferrando[48], A. Ferrari[161], P. Ferrari[114,113], R. Ferrari[73a], D. Ferrere[56], C. Ferretti[106], F. Fiedler[100], A. Filipčič[93], E.K. Filmer[1], F. Filthaut[113], M.C.N. Fiolhais[130a,130c,c], L. Fiorini[163], W.C. Fisher[107], T. Fitschen[101], P.M. Fitzhugh[135], I. Fleck[141], P. Fleischmann[106], T. Flick[171], L. Flores[128], M. Flores[33d,ad], L.R. Flores Castillo[64a], L. Flores Sanz De Acedo[36], F.M. Follega[78a,78b], N. Fomin[16], J.H. Foo[155], B.C. Forland[68], A. Formica[135], A.C. Forti[101], E. Fortin[36], A.W. Fortman[61], M.G. Foti[17a], L. Fountas[9,j], D. Fournier[66], H. Fox[91], P. Francavilla[74a,74b], S. Francescato[61], S. Franchellucci[56], M. Franchini[23b,23a], S. Franchino[63a], D. Francis[36], L. Franco[113], L. Franconi[48], M. Franklin[61], G. Frattari[26], A.C. Freegard[94], W.S. Freund[83b], Y.Y. Frid[151], N. Fritzsche[50], A. Froch[54], D. Froidevaux[36], J.A. Frost[126], Y. Fu[62a], M. Fujimoto[118], E. Fullana Torregrosa[163,*], K.Y. Fung[64a], E. Furtado De Simas Filho[83b], M. Furukawa[153], J. Fuster[163], A. Gabrielli[23b,23a], A. Gabrielli[155], P. Gadow[48], G. Gagliardi[57b,57a], L.G. Gagnon[17a], E.J. Gallas[126], B.J. Gallop[134], K.K. Gan[119], S. Ganguly[153], J. Gao[62a], Y. Gao[52], F.M. Garay Walls[137a,137b], B. Garcia[29], C. García[163], A. Garcia Alonso[114], A.G. Garcia Caffaro[172], J.E. García Navarro[163], M. Garcia-Sciveres[17a], G.L. Gardner[128], R.W. Gardner[39], N. Garelli[158], D. Garg[80], R.B. Garg[143,o], J.M. Gargan[52], C.A. Garner[155], S.J. Gasiorowski[138], P. Gaspar[83b], G. Gaudio[73a], V. Gautam[13], P. Gauzzi[75a,75b], I.L. Gavrilenko[37], A. Gavrilyuk[37], C. Gay[164], G. Gaycken[48], E.N. Gazis[10],

JHEP05(2024)131

A.A. Geanta[27b], C.M. Gee[136], C. Gemme[57b], M.H. Genest[60], S. Gentile[75a,75b], S. George[95], W.F. George[20], T. Geralis[46], P. Gessinger-Befurt[36], M.E. Geyik[171], M. Ghneimat[141], K. Ghorbanian[94], A. Ghosal[141], A. Ghosh[160], A. Ghosh[7], B. Giacobbe[23b], S. Giagu[75a,75b], P. Giannetti[74a], A. Giannini[62a], S.M. Gibson[95], M. Gignac[136], D.T. Gil[86b], A.K. Gilbert[86a], B.J. Gilbert[41], D. Gillberg[34], G. Gilles[114], N.E.K. Gillwald[48], L. Ginabat[127], D.M. Gingrich[2,ag], M.P. Giordani[69a,69c], P.F. Giraud[135], G. Giugliarelli[69a,69c], D. Giugni[71a], F. Giuli[36], I. Gkialas[9,j], L.K. Gladilin[37], C. Glasman[99], G.R. Gledhill[123], M. Glisic[123], I. Gnesi[43b,f], Y. Go[29,ai], M. Goblirsch-Kolb[36], B. Gocke[49], D. Godin[108], B. Gokturk[21a], S. Goldfarb[105], T. Golling[56], M.G.D. Gololo[33g], D. Golubkov[37], J.P. Gombas[107], A. Gomes[130a,130b], G. Gomes Da Silva[141], A.J. Gomez Delegido[163], R. Gonçalo[130a,130c], G. Gonella[123], L. Gonella[20], A. Gongadze[38], F. Gonnella[20], J.L. Gonski[41], R.Y. González Andana[52], S. González de la Hoz[163], S. Gonzalez Fernandez[13], R. Gonzalez Lopez[92], C. Gonzalez Renteria[17a], R. Gonzalez Suarez[161], S. Gonzalez-Sevilla[56], G.R. Gonzalvo Rodriguez[163], L. Goossens[36], P.A. Gorbounov[37], B. Gorini[36], E. Gorini[70a,70b], A. Gorišek[93], T.C. Gosart[128], A.T. Goshaw[51], M.I. Gostkin[38], S. Goswami[121], C.A. Gottardo[36], M. Gouighri[35b], V. Goumarre[48], A.G. Goussiou[138], N. Govender[33c], I. Grabowska-Bold[86a], K. Graham[34], E. Gramstad[125], S. Grancagnolo[70a,70b], M. Grandi[146], P.M. Gravila[27f], F.G. Gravili[70a,70b], H.M. Gray[17a], M. Greco[70a,70b], C. Grefe[24], I.M. Gregor[48], P. Grenier[143], C. Grieco[13], A.A. Grillo[136], K. Grimm[31], S. Grinstein[13,t], J.-F. Grivaz[66], E. Gross[169], J. Grosse-Knetter[55], C. Grud[106], J.C. Grundy[126], L. Guan[106], W. Guan[29], C. Gubbels[164], J.G.R. Guerrero Rojas[163], G. Guerrieri[69a,69b], F. Guescini[110], R. Gugel[100], J.A.M. Guhit[106], A. Guida[18], T. Guillemin[4], E. Guilloton[167,134], S. Guindon[36], F. Guo[14a,14e], J. Guo[62c], L. Guo[48], Y. Guo[106], R. Gupta[48], S. Gurbuz[24], S.S. Gurdasani[54], G. Gustavino[36], M. Guth[56], P. Gutierrez[120], L.F. Gutierrez Zagazeta[128], C. Gutschow[96], C. Gwenlan[126], C.B. Gwilliam[92], E.S. Haaland[125], A. Haas[117], M. Habedank[48], C. Haber[17a], H.K. Hadavand[8], A. Hadef[100], S. Hadzic[110], J.J. Hahn[141], E.H. Haines[96], M. Haleem[166], J. Haley[121], J.J. Hall[139], G.D. Hallewell[102], L. Halser[19], K. Hamano[165], M. Hamer[24], G.N. Hamity[52], E.J. Hampshire[95], J. Han[62b], K. Han[62a], L. Han[14c], L. Han[62a], S. Han[17a], Y.F. Han[155], K. Hanagaki[84], M. Hance[136], D.A. Hangal[41,ac], H. Hanif[142], M.D. Hank[128], R. Hankache[101], J.B. Hansen[42], J.D. Hansen[42], P.H. Hansen[42], K. Hara[157], D. Harada[56], T. Harenberg[171], S. Harkusha[37], M.L. Harris[103], Y.T. Harris[126], J. Harrison[13], N.M. Harrison[119], P.F. Harrison[167], N.M. Hartman[110], N.M. Hartmann[109], Y. Hasegawa[140], A. Hasib[52], S. Haug[19], R. Hauser[107], C.M. Hawkes[20], R.J. Hawkings[36], Y. Hayashi[153], S. Hayashida[111], D. Hayden[107], C. Hayes[106], R.L. Hayes[114], C.P. Hays[126], J.M. Hays[94], H.S. Hayward[92], F. He[62a], M. He[14a,14e], Y. He[154], Y. He[127], N.B. Heatley[94], V. Hedberg[98], A.L. Heggelund[125], N.D. Hehir[94,*], C. Heidegger[54], K.K. Heidegger[54], W.D. Heidorn[81], J. Heilman[34], S. Heim[48], T. Heim[17a], J.G. Heinlein[128], J.J. Heinrich[123], L. Heinrich[110,ae], J. Hejbal[131], L. Helary[48], A. Held[170], S. Hellesund[16], C.M. Helling[164], S. Hellman[47a,47b], C. Helsens[36], R.C.W. Henderson[91], L. Henkelmann[32], A.M. Henriques Correia[36], H. Herde[98], Y. Hernández Jiménez[145], L.M. Herrmann[24], T. Herrmann[50], G. Herten[54],

JHEP05(2024)131

R. Hertenberger[109], L. Hervas[36], M.E. Hesping[100], N.P. Hessey[156a], H. Hibi[85], S.J. Hillier[20], J.R. Hinds[107], F. Hinterkeuser[24], M. Hirose[124], S. Hirose[157], D. Hirschbuehl[171], T.G. Hitchings[101], B. Hiti[93], J. Hobbs[145], R. Hobincu[27e], N. Hod[169], M.C. Hodgkinson[139], B.H. Hodkinson[32], A. Hoecker[36], J. Hofer[48], T. Holm[24], M. Holzbock[110], L.B.A.H. Hommels[32], B.P. Honan[101], J. Hong[62c], T.M. Hong[129], B.H. Hooberman[162], W.H. Hopkins[6], Y. Horii[111], S. Hou[148], A.S. Howard[93], J. Howarth[59], J. Hoya[6], M. Hrabovsky[122], A. Hrynevich[48], T. Hryn'ova[4], P.J. Hsu[65], S.-C. Hsu[138], Q. Hu[41], Y.F. Hu[14a,14e], S. Huang[64b], X. Huang[14c], Y. Huang[139], Y. Huang[14a], Z. Huang[101], Z. Hubacek[132], M. Huebner[24], F. Huegging[24], T.B. Huffman[126], C.A. Hugli[48], M. Huhtinen[36], S.K. Huiberts[16], R. Hulsken[104], N. Huseynov[12], J. Huston[107], J. Huth[61], R. Hyneman[143], G. Iacobucci[56], G. Iakovidis[29], I. Ibragimov[141], L. Iconomidou-Fayard[66], P. Iengo[72a,72b], R. Iguchi[153], T. Iizawa[84], Y. Ikegami[84], N. Ilic[155], H. Imam[35a], M. Ince Lezki[56], T. Ingebretsen Carlson[47a,47b], G. Introzzi[73a,73b], M. Iodice[77a], V. Ippolito[75a,75b], R.K. Irwin[92], M. Ishino[153], W. Islam[170], C. Issever[18,48], S. Istin[21a,ak], H. Ito[168], J.M. Iturbe Ponce[64a], R. Iuppa[78a,78b], A. Ivina[169], J.M. Izen[45], V. Izzo[72a], P. Jacka[131,132], P. Jackson[1], R.M. Jacobs[48], B.P. Jaeger[142], C.S. Jagfeld[109], P. Jain[54], G. Jäkel[171], K. Jakobs[54], T. Jakoubek[169], J. Jamieson[59], K.W. Janas[86a], A.E. Jaspan[92], M. Javurkova[103], F. Jeanneau[135], L. Jeanty[123], J. Jejelava[149a,aa], P. Jenni[54,g], C.E. Jessiman[34], S. Jézéquel[4], C. Jia[62b], J. Jia[145], X. Jia[61], X. Jia[14a,14e], Z. Jia[14c], Y. Jiang[62a], S. Jiggins[48], J. Jimenez Pena[13], S. Jin[14c], A. Jinaru[27b], O. Jinnouchi[154], P. Johansson[139], K.A. Johns[7], J.W. Johnson[136], D.M. Jones[32], E. Jones[48], P. Jones[32], R.W.L. Jones[91], T.J. Jones[92], R. Joshi[119], J. Jovicevic[15], X. Ju[17a], J.J. Junggeburth[36], T. Junkermann[63a], A. Juste Rozas[13,t], M.K. Juzek[87], S. Kabana[137e], A. Kaczmarska[87], M. Kado[110], H. Kagan[119], M. Kagan[143], A. Kahn[41], A. Kahn[128], C. Kahra[100], T. Kaji[168], E. Kajomovitz[150], N. Kakati[169], I. Kalaitzidou[54], C.W. Kalderon[29], A. Kamenshchikov[155], S. Kanayama[154], N.J. Kang[136], D. Kar[33g], K. Karava[126], M.J. Kareem[156b], E. Karentzos[54], I. Karkanias[152], O. Karkout[114], S.N. Karpov[38], Z.M. Karpova[38], V. Kartvelishvili[91], A.N. Karyukhin[37], E. Kasimi[152], J. Katzy[48], S. Kaur[34], K. Kawade[140], T. Kawamoto[135], E.F. Kay[36], F.I. Kaya[158], S. Kazakos[107], V.F. Kazanin[37], Y. Ke[145], J.M. Keaveney[33a], R. Keeler[165], G.V. Kehris[61], J.S. Keller[34], A.S. Kelly[96], J.J. Kempster[146], K.E. Kennedy[41], P.D. Kennedy[100], O. Kepka[131], B.P. Kerridge[167], S. Kersten[171], B.P. Kerševan[93], S. Keshri[66], L. Keszeghova[28a], S. Ketabchi Haghighat[155], M. Khandoga[127], A. Khanov[121], A.G. Kharlamov[37], T. Kharlamova[37], E.E. Khoda[138], T.J. Khoo[18], G. Khoriauli[166], J. Khubua[149b], Y.A.R. Khwaira[66], M. Kiehn[36], A. Kilgallon[123], D.W. Kim[47a,47b], Y.K. Kim[39], N. Kimura[96], A. Kirchhoff[55], C. Kirfel[24], F. Kirfel[24], J. Kirk[134], A.E. Kiryunin[110], C. Kitsaki[10], O. Kivernyk[24], M. Klassen[63a], C. Klein[34], L. Klein[166], M.H. Klein[106], M. Klein[92], S.B. Klein[56], U. Klein[92], P. Klimek[36], A. Klimentov[29], T. Klioutchnikova[36], P. Kluit[114], S. Kluth[110], E. Kneringer[79], T.M. Knight[155], A. Knue[54], R. Kobayashi[88], S.F. Koch[126], M. Kocian[143], P. Kodyš[133], D.M. Koeck[123], P.T. Koenig[24], T. Koffas[34], M. Kolb[135], I. Koletsou[4], T. Komarek[122], K. Köneke[54], A.X.Y. Kong[1], T. Kono[118], N. Konstantinidis[96], B. Konya[98], R. Kopeliansky[68], S. Koperny[86a], K. Korcyl[87],

JHEP05(2024)131

K. Kordas[152,e], G. Koren[151], A. Korn[96], S. Korn[55], I. Korolkov[13], N. Korotkova[37], B. Kortman[114], O. Kortner[110], S. Kortner[110], W.H. Kostecka[115], V.V. Kostyukhin[141], A. Kotsokechagia[135], A. Kotwal[51], A. Koulouris[36], A. Kourkoumeli-Charalampidi[73a,73b], C. Kourkoumelis[9], E. Kourlitis[6], O. Kovanda[146], R. Kowalewski[165], W. Kozanecki[135], A.S. Kozhin[37], V.A. Kramarenko[37], G. Kramberger[93], P. Kramer[100], M.W. Krasny[127], A. Krasznahorkay[36], J.W. Kraus[171], J.A. Kremer[100], T. Kresse[50], J. Kretzschmar[92], K. Kreul[18], P. Krieger[155], S. Krishnamurthy[103], M. Krivos[133], K. Krizka[20], K. Kroeninger[49], H. Kroha[110], J. Kroll[131], J. Kroll[128], K.S. Krowpman[107], U. Kruchonak[38], H. Krüger[24], N. Krumnack[81], M.C. Kruse[51], J.A. Krzysiak[87], O. Kuchinskaia[37], S. Kuday[3a], S. Kuehn[36], R. Kuesters[54], T. Kuhl[48], V. Kukhtin[38], Y. Kulchitsky[37,a], S. Kuleshov[137d,137b], M. Kumar[33g], N. Kumari[102], A. Kupco[131], T. Kupfer[49], A. Kupich[37], O. Kuprash[54], H. Kurashige[85], L.L. Kurchaninov[156a], O. Kurdysh[66], Y.A. Kurochkin[37], A. Kurova[37], M. Kuze[154], A.K. Kvam[103], J. Kvita[122], T. Kwan[104], N.G. Kyriacou[106], L.A.O. Laatu[102], C. Lacasta[163], F. Lacava[75a,75b], H. Lacker[18], D. Lacour[127], N.N. Lad[96], E. Ladygin[38], B. Laforge[127], T. Lagouri[137e], S. Lai[55], I.K. Lakomiec[86a], N. Lalloue[60], J.E. Lambert[165], S. Lammers[68], W. Lampl[7], C. Lampoudis[152,e], A.N. Lancaster[115], E. Lançon[29], U. Landgraf[54], M.P.J. Landon[94], V.S. Lang[54], R.J. Langenberg[103], O.K.B. Langrekken[125], A.J. Lankford[160], F. Lanni[36], K. Lantzsch[24], A. Lanza[73a], A. Lapertosa[57b,57a], J.F. Laporte[135], T. Lari[71a], F. Lasagni Manghi[23b], M. Lassnig[36], V. Latonova[131], A. Laudrain[100], A. Laurier[150], S.D. Lawlor[95], Z. Lawrence[101], M. Lazzaroni[71a,71b], B. Le[101], E.M. Le Boulicaut[51], B. Leban[93], A. Lebedev[81], M. LeBlanc[36], F. Ledroit-Guillon[60], A.C.A. Lee[96], S.C. Lee[148], S. Lee[47a,47b], T.F. Lee[92], L.L. Leeuw[33c], H.P. Lefebvre[95], M. Lefebvre[165], C. Leggett[17a], G. Lehmann Miotto[36], M. Leigh[56], W.A. Leight[103], W. Leinonen[113], A. Leisos[152,s], M.A.L. Leite[83c], C.E. Leitgeb[48], R. Leitner[133], K.J.C. Leney[44], T. Lenz[24], S. Leone[74a], C. Leonidopoulos[52], A. Leopold[144], C. Leroy[108], R. Les[107], C.G. Lester[32], M. Levchenko[37], J. Levêque[4], D. Levin[106], L.J. Levinson[169], M.P. Lewicki[87], D.J. Lewis[4], A. Li[5], B. Li[62b], C. Li[62a], C-Q. Li[62c], H. Li[62a], H. Li[62b], H. Li[14c], H. Li[62b], K. Li[138], L. Li[62c], M. Li[14a,14e], Q.Y. Li[62a], S. Li[14a,14e], S. Li[62d,62c,d], T. Li[5], X. Li[104], Z. Li[126], Z. Li[104], Z. Li[92], Z. Li[14a,14e], Z. Liang[14a], M. Liberatore[48], B. Liberti[76a], K. Lie[64c], J. Lieber Marin[83b], H. Lien[68], K. Lin[107], R.E. Lindley[7], J.H. Lindon[2], A. Linss[48], E. Lipeles[128], A. Lipniacka[16], A. Lister[164], J.D. Little[4], B. Liu[14a], B.X. Liu[142], D. Liu[62d,62c], J.B. Liu[62a], J.K.K. Liu[32], K. Liu[62d,62c], M. Liu[62a], M.Y. Liu[62a], P. Liu[14a], Q. Liu[62d,138,62c], X. Liu[62a], Y. Liu[14d,14e], Y.L. Liu[106], Y.W. Liu[62a], J. Llorente Merino[142], S.L. Lloyd[94], E.M. Lobodzinska[48], P. Loch[7], S. Loffredo[76a,76b], T. Lohse[18], K. Lohwasser[139], E. Loiacono[48], M. Lokajicek[131,*], J.D. Lomas[20], J.D. Long[162], I. Longarini[160], L. Longo[70a,70b], R. Longo[162], I. Lopez Paz[67], A. Lopez Solis[48], J. Lorenz[109], N. Lorenzo Martinez[4], A.M. Lory[109], G. Löschcke Centeno[146], O. Loseva[37], X. Lou[47a,47b], X. Lou[14a,14e], A. Lounis[66], J. Love[6], P.A. Love[91], G. Lu[14a,14e], M. Lu[80], S. Lu[128], Y.J. Lu[65], H.J. Lubatti[138], C. Luci[75a,75b], F.L. Lucio Alves[14c], A. Lucotte[60], F. Luehring[68], I. Luise[145], O. Lukianchuk[66], O. Lundberg[144], B. Lund-Jensen[144], N.A. Luongo[123], M.S. Lutz[151], D. Lynn[29], H. Lyons[92], R. Lysak[131], E. Lytken[98],

JHEP05(2024)131

V. Lyubushkin[38], T. Lyubushkina[38], M.M. Lyukova[145], H. Ma[29], K. Ma[62a], L.L. Ma[62b], Y. Ma[121], D.M. Mac Donell[165], G. Maccarrone[53], J.C. MacDonald[100], R. Madar[40], W.F. Mader[50], J. Maeda[85], T. Maeno[29], M. Maerker[50], H. Maguire[139], V. Maiboroda[135], A. Maio[130a,130b,130d], K. Maj[86a], O. Majersky[48], S. Majewski[123], N. Makovec[66], V. Maksimovic[15], B. Malaescu[127], Pa. Malecki[87], V.P. Maleev[37], F. Malek[60], M. Mali[93], D. Malito[95], U. Mallik[80], S. Maltezos[10], S. Malyukov[38], J. Mamuzic[13], G. Mancini[53], G. Manco[73a,73b], J.P. Mandalia[94], I. Mandić[93], L. Manhaes de Andrade Filho[83a], I.M. Maniatis[169], J. Manjarres Ramos[102,ab], D.C. Mankad[169], A. Mann[109], B. Mansoulie[135], S. Manzoni[36], A. Marantis[152,s], G. Marchiori[5], M. Marcisovsky[131], C. Marcon[71a], M. Marinescu[20], M. Marjanovic[120], E.J. Marshall[91], Z. Marshall[17a], S. Marti-Garcia[163], T.A. Martin[167], V.J. Martin[52], B. Martin dit Latour[16], L. Martinelli[75a,75b], M. Martinez[13,t], P. Martinez Agullo[163], V.I. Martinez Outschoorn[103], P. Martinez Suarez[13], S. Martin-Haugh[134], V.S. Martoiu[27b], A.C. Martyniuk[96], A. Marzin[36], D. Mascione[78a,78b], L. Masetti[100], T. Mashimo[153], J. Masik[101], A.L. Maslennikov[37], L. Massa[23b], P. Massarotti[72a,72b], P. Mastrandrea[74a,74b], A. Mastroberardino[43b,43a], T. Masubuchi[153], T. Mathisen[161], J. Matousek[133], N. Matsuzawa[153], J. Maurer[27b], B. Maček[93], D.A. Maximov[37], R. Mazini[148], I. Maznas[152], M. Mazza[107], S.M. Mazza[136], E. Mazzeo[71a,71b], C. Mc Ginn[29], J.P. Mc Gowan[104], S.P. Mc Kee[106], E.F. McDonald[105], A.E. McDougall[114], J.A. Mcfayden[146], R.P. McGovern[128], G. Mchedlidze[149b], R.P. Mckenzie[33g], T.C. Mclachlan[48], D.J. Mclaughlin[96], K.D. McLean[165], S.J. McMahon[134], P.C. McNamara[105], C.M. Mcpartland[92], R.A. McPherson[165,x], S. Mehlhase[109], A. Mehta[92], D. Melini[150], B.R. Mellado Garcia[33g], A.H. Melo[55], F. Meloni[48], A.M. Mendes Jacques Da Costa[101], H.Y. Meng[155], L. Meng[91], S. Menke[110], M. Mentink[36], E. Meoni[43b,43a], C. Merlassino[126], L. Merola[72a,72b], C. Meroni[71a,71b], G. Merz[106], O. Meshkov[37], J. Metcalfe[6], A.S. Mete[6], C. Meyer[68], J-P. Meyer[135], R.P. Middleton[134], L. Mijović[52], G. Mikenberg[169], M. Mikestikova[131], M. Mikuž[93], H. Mildner[100], A. Milic[36], C.D. Milke[44], D.W. Miller[39], L.S. Miller[34], A. Milov[169], D.A. Milstead[47a,47b], T. Min[14c], A.A. Minaenko[37], I.A. Minashvili[149b], L. Mince[59], A.I. Mincer[117], B. Mindur[86a], M. Mineev[38], Y. Mino[88], L.M. Mir[13], M. Miralles Lopez[163], M. Mironova[17a], A. Mishima[153], M.C. Missio[113], T. Mitani[168], A. Mitra[167], V.A. Mitsou[163], O. Miu[155], P.S. Miyagawa[94], Y. Miyazaki[89], A. Mizukami[84], T. Mkrtchyan[63a], M. Mlinarevic[96], T. Mlinarevic[96], M. Mlynarikova[36], S. Mobius[19], K. Mochizuki[108], P. Moder[48], P. Mogg[109], A.F. Mohammed[14a,14e], S. Mohapatra[41], G. Mokgatitswane[33g], L. Moleri[169], B. Mondal[141], S. Mondal[132], K. Mönig[48], E. Monnier[102], L. Monsonis Romero[163], J. Montejo Berlingen[13,84], M. Montella[119], F. Montereali[77a,77b], F. Monticelli[90], S. Monzani[69a,69c], N. Morange[66], A.L. Moreira De Carvalho[130a], M. Moreno Llácer[163], C. Moreno Martinez[56], P. Morettini[57b], S. Morgenstern[36], M. Morii[61], M. Morinaga[153], A.K. Morley[36], F. Morodei[75a,75b], L. Morvaj[36], P. Moschovakos[36], B. Moser[36], M. Mosidze[149b], T. Moskalets[54], P. Moskvitina[113], J. Moss[31,m], E.J.W. Moyse[103], O. Mtintsilana[33g], S. Muanza[102], J. Mueller[129], D. Muenstermann[91], R. Müller[19], G.A. Mullier[161], A.J. Mullin[32], J.J. Mullin[128], D.P. Mungo[155], D. Munoz Perez[163], F.J. Munoz Sanchez[101], M. Murin[101], W.J. Murray[167,134], A. Murrone[71a,71b],

JHEP05(2024)131

J.M. Muse[120], M. Muškinja[17a], C. Mwewa[29], A.G. Myagkov[37,a], A.J. Myers[8], A.A. Myers[129], G. Myers[68], M. Myska[132], B.P. Nachman[17a], O. Nackenhorst[49], A. Nag[50], K. Nagai[126], K. Nagano[84], J.L. Nagle[29,ai], E. Nagy[102], A.M. Nairz[36], Y. Nakahama[84], K. Nakamura[84], K. Nakkalil[5], H. Nanjo[124], R. Narayan[44], E.A. Narayanan[112], I. Naryshkin[37], M. Naseri[34], S. Nasri[159], C. Nass[24], G. Navarro[22a], J. Navarro-Gonzalez[163], R. Nayak[151], A. Nayaz[18], P.Y. Nechaeva[37], F. Nechansky[48], L. Nedic[126], T.J. Neep[20], A. Negri[73a,73b], M. Negrini[23b], C. Nellist[114], C. Nelson[104], K. Nelson[106], S. Nemecek[131], M. Nessi[36,h], M.S. Neubauer[162], F. Neuhaus[100], J. Neundorf[48], R. Newhouse[164], P.R. Newman[20], C.W. Ng[129], Y.W.Y. Ng[48], B. Ngair[35e], H.D.N. Nguyen[108], R.B. Nickerson[126], R. Nicolaidou[135], J. Nielsen[136], M. Niemeyer[55], J. Niermann[55,36], N. Nikiforou[36], V. Nikolaenko[37,a], I. Nikolic-Audit[127], K. Nikolopoulos[20], P. Nilsson[29], I. Ninca[48], H.R. Nindhito[56], G. Ninio[151], A. Nisati[75a], N. Nishu[2], R. Nisius[110], J-E. Nitschke[50], E.K. Nkadimeng[33g], S.J. Noacco Rosende[90], T. Nobe[153], D.L. Noel[32], T. Nommensen[147], M.B. Norfolk[139], R.R.B. Norisam[96], B.J. Norman[34], J. Novak[93], T. Novak[48], L. Novotny[132], R. Novotny[112], L. Nozka[122], K. Ntekas[160], N.M.J. Nunes De Moura Junior[83b], E. Nurse[96], J. Ocariz[127], A. Ochi[85], I. Ochoa[130a], S. Oerdek[161], J.T. Offermann[39], A. Ogrodnik[133], A. Oh[101], C.C. Ohm[144], H. Oide[84], R. Oishi[153], M.L. Ojeda[48], Y. Okazaki[88], M.W. O'Keefe[92], Y. Okumura[153], L.F. Oleiro Seabra[130a], S.A. Olivares Pino[137d], D. Oliveira Damazio[29], D. Oliveira Goncalves[83a], J.L. Oliver[160], A. Olszewski[87], Ö.O. Öncel[54], D.C. O'Neil[142], A.P. O'Neill[19], A. Onofre[130a,130e], P.U.E. Onyisi[11], M.J. Oreglia[39], G.E. Orellana[90], D. Orestano[77a,77b], N. Orlando[13], R.S. Orr[155], V. O'Shea[59], L.M. Osojnak[128], R. Ospanov[62a], G. Otero y Garzon[30], H. Otono[89], P.S. Ott[63a], G.J. Ottino[17a], M. Ouchrif[35d], J. Ouellette[29], F. Ould-Saada[125], M. Owen[59], R.E. Owen[134], K.Y. Oyulmaz[21a], V.E. Ozcan[21a], N. Ozturk[8], S. Ozturk[82], H.A. Pacey[32], A. Pacheco Pages[13], C. Padilla Aranda[13], G. Padovano[75a,75b], S. Pagan Griso[17a], G. Palacino[68], A. Palazzo[70a,70b], S. Palestini[36], J. Pan[172], T. Pan[64a], D.K. Panchal[11], C.E. Pandini[114], J.G. Panduro Vazquez[95], H. Pang[14b], P. Pani[48], G. Panizzo[69a,69c], L. Paolozzi[56], C. Papadatos[108], S. Parajuli[44], A. Paramonov[6], C. Paraskevopoulos[10], D. Paredes Hernandez[64b], T.H. Park[155], M.A. Parker[32], F. Parodi[57b,57a], E.W. Parrish[115], V.A. Parrish[52], J.A. Parsons[41], U. Parzefall[54], B. Pascual Dias[108], L. Pascual Dominguez[151], F. Pasquali[114], E. Pasqualucci[75a], S. Passaggio[57b], F. Pastore[95], P. Pasuwan[47a,47b], P. Patel[87], U.M. Patel[51], J.R. Pater[101], T. Pauly[36], J. Pearkes[143], M. Pedersen[125], R. Pedro[130a], S.V. Peleganchuk[37], O. Penc[36], E.A. Pender[52], H. Peng[62a], K.E. Penski[109], M. Penzin[37], B.S. Peralva[83d], A.P. Pereira Peixoto[60], L. Pereira Sanchez[47a,47b], D.V. Perepelitsa[29,ai], E. Perez Codina[156a], M. Perganti[10], L. Perini[71a,71b,*], H. Pernegger[36], A. Perrevoort[113], O. Perrin[40], K. Peters[48], R.F.Y. Peters[101], B.A. Petersen[36], T.C. Petersen[42], E. Petit[102], V. Petousis[132], C. Petridou[152,e], A. Petrukhin[141], M. Pettee[17a], N.E. Pettersson[36], A. Petukhov[37], K. Petukhova[133], A. Peyaud[135], R. Pezoa[137f], L. Pezzotti[36], G. Pezzullo[172], T.M. Pham[170], T. Pham[105], P.W. Phillips[134], G. Piacquadio[145], E. Pianori[17a], F. Piazza[71a,71b], R. Piegaia[30], D. Pietreanu[27b], A.D. Pilkington[101], M. Pinamonti[69a,69c], J.L. Pinfold[2], B.C. Pinheiro Pereira[130a], A.E. Pinto Pinoargote[135], K.M. Piper[146],

JHEP05(2024)131

A. Pirttikoski[56], C. Pitman Donaldson[96], D.A. Pizzi[34], L. Pizzimento[64b], A. Pizzini[114], M.-A. Pleier[29], V. Plesanovs[54], V. Pleskot[133], E. Plotnikova[38], G. Poddar[4], R. Poettgen[98], L. Poggioli[127], I. Pokharel[55], S. Polacek[133], G. Polesello[73a], A. Poley[142,156a], R. Polifka[132], A. Polini[23b], C.S. Pollard[167], Z.B. Pollock[119], V. Polychronakos[29], E. Pompa Pacchi[75a,75b], D. Ponomarenko[113], L. Pontecorvo[36], S. Popa[27a], G.A. Popeneciu[27d], A. Poreba[36], D.M. Portillo Quintero[156a], S. Pospisil[132], M.A. Postill[139], P. Postolache[27c], K. Potamianos[167], P.A. Potepa[86a], I.N. Potrap[38], C.J. Potter[32], H. Potti[1], T. Poulsen[48], J. Poveda[163], M.E. Pozo Astigarraga[36], A. Prades Ibanez[163], J. Pretel[54], D. Price[101], M. Primavera[70a], M.A. Principe Martin[99], R. Privara[122], T. Procter[59], M.L. Proffitt[138], N. Proklova[128], K. Prokofiev[64c], G. Proto[110], S. Protopopescu[29], J. Proudfoot[6], M. Przybycien[86a], W.W. Przygoda[86b], J.E. Puddefoot[139], D. Pudzha[37], D. Pyatiizbyantseva[37], J. Qian[106], D. Qichen[101], Y. Qin[101], T. Qiu[52], A. Quadt[55], M. Queitsch-Maitland[101], G. Quetant[56], G. Rabanal Bolanos[61], D. Rafanoharana[54], F. Ragusa[71a,71b], J.L. Rainbolt[39], J.A. Raine[56], S. Rajagopalan[29], E. Ramakoti[37], K. Ran[48,14e], N.P. Rapheeha[33g], H. Rasheed[27b], V. Raskina[127], D.F. Rassloff[63a], S. Rave[100], B. Ravina[55], I. Ravinovich[169], M. Raymond[36], A.L. Read[125], N.P. Readioff[139], D.M. Rebuzzi[73a,73b], G. Redlinger[29], A.S. Reed[110], K. Reeves[26], J.A. Reidelsturz[171], D. Reikher[151], A. Rej[141], C. Rembser[36], A. Renardi[48], M. Renda[27b], M.B. Rendel[110], F. Renner[48], A.G. Rennie[59], S. Resconi[71a], M. Ressegotti[57b,57a], S. Rettie[36], J.G. Reyes Rivera[107], B. Reynolds[119], E. Reynolds[17a], O.L. Rezanova[37], P. Reznicek[133], N. Ribaric[91], E. Ricci[78a,78b], R. Richter[110], S. Richter[47a,47b], E. Richter-Was[86b], M. Ridel[127], S. Ridouani[35d], P. Rieck[117], P. Riedler[36], M. Rijssenbeek[145], A. Rimoldi[73a,73b], M. Rimoldi[48], L. Rinaldi[23b,23a], T.T. Rinn[29], M.P. Rinnagel[109], G. Ripellino[161], I. Riu[13], P. Rivadeneira[48], J.C. Rivera Vergara[165], F. Rizatdinova[121], E. Rizvi[94], B.A. Roberts[167], B.R. Roberts[17a], S.H. Robertson[104,x], M. Robin[48], D. Robinson[32], C.M. Robles Gajardo[137f], M. Robles Manzano[100], A. Robson[59], A. Rocchi[76a,76b], C. Roda[74a,74b], S. Rodriguez Bosca[63a], Y. Rodriguez Garcia[22a], A. Rodriguez Rodriguez[54], A.M. Rodríguez Vera[156b], S. Roe[36], J.T. Roemer[160], A.R. Roepe-Gier[136], J. Roggel[171], O. Røhne[125], R.A. Rojas[103], C.P.A. Roland[68], J. Roloff[29], A. Romaniouk[37], E. Romano[73a,73b], M. Romano[23b], A.C. Romero Hernandez[162], N. Rompotis[92], L. Roos[127], S. Rosati[75a], B.J. Rosser[39], E. Rossi[126], E. Rossi[72a,72b], L.P. Rossi[57b], L. Rossini[48], R. Rosten[119], M. Rotaru[27b], B. Rottler[54], C. Rougier[102,ab], D. Rousseau[66], D. Rousso[32], A. Roy[162], S. Roy-Garand[155], A. Rozanov[102], Y. Rozen[150], X. Ruan[33g], A. Rubio Jimenez[163], A.J. Ruby[92], V.H. Ruelas Rivera[18], T.A. Ruggeri[1], A. Ruggiero[126], A. Ruiz-Martinez[163], A. Rummler[36], Z. Rurikova[54], N.A. Rusakovich[38], H.L. Russell[165], G. Russo[75a,75b], J.P. Rutherfoord[7], S. Rutherford Colmenares[32], K. Rybacki[91], M. Rybar[133], E.B. Rye[125], A. Ryzhov[44], J.A. Sabater Iglesias[56], P. Sabatini[163], L. Sabetta[75a,75b], H.F-W. Sadrozinski[136], F. Safai Tehrani[75a], B. Safarzadeh Samani[146], M. Safdari[143], S. Saha[165], M. Sahinsoy[110], M. Saimpert[135], M. Saito[153], T. Saito[153], D. Salamani[36], A. Salnikov[143], J. Salt[163], A. Salvador Salas[13], D. Salvatore[43b,43a], F. Salvatore[146], A. Salzburger[36], D. Sammel[54], D. Sampsonidis[152,e], D. Sampsonidou[123], J. Sánchez[163], A. Sanchez Pineda[4], V. Sanchez Sebastian[163], H. Sandaker[125], C.O. Sander[48],

JHEP05(2024)131

J.A. Sandesara[103], M. Sandhoff[171], C. Sandoval[22b], D.P.C. Sankey[134], T. Sano[88], A. Sansoni[53], L. Santi[75a,75b], C. Santoni[40], H. Santos[130a,130b], S.N. Santpur[17a], A. Santra[169], K.A. Saoucha[139], J.G. Saraiva[130a,130d], J. Sardain[7], O. Sasaki[84], K. Sato[157], C. Sauer[63b], F. Sauerburger[54], E. Sauvan[4], P. Savard[155,ag], R. Sawada[153], C. Sawyer[134], L. Sawyer[97], I. Sayago Galvan[163], C. Sbarra[23b], A. Sbrizzi[23b,23a], T. Scanlon[96], J. Schaarschmidt[138], P. Schacht[110], D. Schaefer[39], U. Schäfer[100], A.C. Schaffer[66,44], D. Schaile[109], R.D. Schamberger[145], C. Scharf[18], M.M. Schefer[19], V.A. Schegelsky[37], D. Scheirich[133], F. Schenck[18], M. Schernau[160], C. Scheulen[55], C. Schiavi[57b,57a], E.J. Schioppa[70a,70b], M. Schioppa[43b,43a], B. Schlag[143,o], K.E. Schleicher[54], S. Schlenker[36], J. Schmeing[171], M.A. Schmidt[171], K. Schmieden[100], C. Schmitt[100], S. Schmitt[48], L. Schoeffel[135], A. Schoening[63b], P.G. Scholer[54], E. Schopf[126], M. Schott[100], J. Schovancova[36], S. Schramm[56], F. Schroeder[171], T. Schroer[56], H-C. Schultz-Coulon[63a], M. Schumacher[54], B.A. Schumm[136], Ph. Schune[135], A.J. Schuy[138], H.R. Schwartz[136], A. Schwartzman[143], T.A. Schwarz[106], Ph. Schwemling[135], R. Schwienhorst[107], A. Sciandra[136], G. Sciolla[26], F. Scuri[74a], C.D. Sebastiani[92], K. Sedlaczek[115], P. Seema[18], S.C. Seidel[112], A. Seiden[136], B.D. Seidlitz[41], C. Seitz[48], J.M. Seixas[83b], G. Sekhniaidze[72a], S.J. Sekula[44], L. Selem[60], N. Semprini-Cesari[23b,23a], D. Sengupta[56], V. Senthilkumar[163], L. Serin[66], L. Serkin[69a,69b], M. Sessa[76a,76b], H. Severini[120], F. Sforza[57b,57a], A. Sfyrla[56], E. Shabalina[55], R. Shaheen[144], J.D. Shahinian[128], D. Shaked Renous[169], L.Y. Shan[14a], M. Shapiro[17a], A. Sharma[36], A.S. Sharma[164], P. Sharma[80], S. Sharma[48], P.B. Shatalov[37], K. Shaw[146], S.M. Shaw[101], A. Shcherbakova[37], Q. Shen[62c,5], P. Sherwood[96], L. Shi[96], X. Shi[14a], C.O. Shimmin[172], Y. Shimogama[168], J.D. Shinner[95], I.P.J. Shipsey[126], S. Shirabe[56,h], M. Shiyakova[38,v], J. Shlomi[169], M.J. Shochet[39], J. Shojaii[105], D.R. Shope[125], B. Shrestha[120], S. Shrestha[119,aj], E.M. Shrif[33g], M.J. Shroff[165], P. Sicho[131], A.M. Sickles[162], E. Sideras Haddad[33g], A. Sidoti[23b], F. Siegert[50], Dj. Sijacki[15], R. Sikora[86a], F. Sili[90], J.M. Silva[20], M.V. Silva Oliveira[29], S.B. Silverstein[47a], S. Simion[66], R. Simoniello[36], E.L. Simpson[59], H. Simpson[146], L.R. Simpson[106], N.D. Simpson[98], S. Simsek[82], S. Sindhu[55], P. Sinervo[155], S. Singh[155], S. Sinha[48], S. Sinha[101], M. Sioli[23b,23a], I. Siral[36], E. Sitnikova[48], S.Yu. Sivoklokov[37,*], J. Sjölin[47a,47b], A. Skaf[55], E. Skorda[98], P. Skubic[120], M. Slawinska[87], V. Smakhtin[169], B.H. Smart[134], J. Smiesko[36], S.Yu. Smirnov[37], Y. Smirnov[37], L.N. Smirnova[37,a], O. Smirnova[98], A.C. Smith[41], E.A. Smith[39], H.A. Smith[126], J.L. Smith[92], R. Smith[143], M. Smizanska[91], K. Smolek[132], A.A. Snesarev[37], S.R. Snider[155], H.L. Snoek[114], S. Snyder[29], R. Sobie[165,x], A. Soffer[151], C.A. Solans Sanchez[36], E.Yu. Soldatov[37], U. Soldevila[163], A.A. Solodkov[37], S. Solomon[26], A. Soloshenko[38], K. Solovieva[54], O.V. Solovyanov[40], V. Solovyev[37], P. Sommer[36], A. Sonay[13], W.Y. Song[156b], J.M. Sonneveld[114], A. Sopczak[132], A.L. Sopio[96], F. Sopkova[28b], V. Sothilingam[63a], S. Sottocornola[68], R. Soualah[116b], Z. Soumaimi[35e], D. South[48], S. Spagnolo[70a,70b], M. Spalla[110], D. Sperlich[54], G. Spigo[36], M. Spina[146], S. Spinali[91], D.P. Spiteri[59], M. Spousta[133], E.J. Staats[34], A. Stabile[71a,71b], R. Stamen[63a], M. Stamenkovic[114], A. Stampekis[20], M. Standke[24], E. Stanecka[87], M.V. Stange[50], B. Stanislaus[17a], M.M. Stanitzki[48], B. Stapf[48], E.A. Starchenko[37], G.H. Stark[136], J. Stark[102,ab], D.M. Starko[156b], P. Staroba[131], P. Starovoitov[63a],

JHEP05(2024)131

S. Stärz[104], R. Staszewski[87], G. Stavropoulos[46], J. Steentoft[161], P. Steinberg[29], B. Stelzer[142,156a], H.J. Stelzer[129], O. Stelzer-Chilton[156a], H. Stenzel[58], T.J. Stevenson[146], G.A. Stewart[36], J.R. Stewart[121], M.C. Stockton[36], G. Stoicea[27b], M. Stolarski[130a], S. Stonjek[110], A. Straessner[50], J. Strandberg[144], S. Strandberg[47a,47b], M. Strauss[120], T. Strebler[102], P. Strizenec[28b], R. Ströhmer[166], D.M. Strom[123], L.R. Strom[48], R. Stroynowski[44], A. Strubig[47a,47b], S.A. Stucci[29], B. Stugu[16], J. Stupak[120], N.A. Styles[48], D. Su[143], S. Su[62a], W. Su[62d], X. Su[62a,66], K. Sugizaki[153], V.V. Sulin[37], M.J. Sullivan[92], D.M.S. Sultan[78a,78b], L. Sultanaliyeva[37], S. Sultansoy[3b], T. Sumida[88], S. Sun[106], S. Sun[170], O. Sunneborn Gudnadottir[161], N. Sur[102], M.R. Sutton[146], H. Suzuki[157], M. Svatos[131], M. Swiatlowski[156a], T. Swirski[166], I. Sykora[28a], M. Sykora[133], T. Sykora[133], D. Ta[100], K. Tackmann[48,u], A. Taffard[160], R. Tafirout[156a], J.S. Tafoya Vargas[66], E.P. Takeva[52], Y. Takubo[84], M. Talby[102], A.A. Talyshev[37], K.C. Tam[64b], N.M. Tamir[151], A. Tanaka[153], J. Tanaka[153], R. Tanaka[66], M. Tanasini[57b,57a], Z. Tao[164], S. Tapia Araya[137f], S. Tapprogge[100], A. Tarek Abouelfadl Mohamed[107], S. Tarem[150], K. Tariq[14a], G. Tarna[102,27b], G.F. Tartarelli[71a], P. Tas[133], M. Tasevsky[131], E. Tassi[43b,43a], A.C. Tate[162], G. Tateno[153], Y. Tayalati[35e,w], G.N. Taylor[105], W. Taylor[156b], H. Teagle[92], A.S. Tee[170], R. Teixeira De Lima[143], P. Teixeira-Dias[95], J.J. Teoh[155], K. Terashi[153], J. Terron[99], S. Terzo[13], M. Testa[53], R.J. Teuscher[155,x], A. Thaler[79], O. Theiner[56], N. Themistokleous[52], T. Theveneaux-Pelzer[102], O. Thielmann[171], D.W. Thomas[95], J.P. Thomas[20], E.A. Thompson[17a], P.D. Thompson[20], E. Thomson[128], Y. Tian[55], V. Tikhomirov[37,a], Yu.A. Tikhonov[37], S. Timoshenko[37], D. Timoshyn[133], E.X.L. Ting[1], P. Tipton[172], S.H. Tlou[33g], A. Tnourji[40], K. Todome[23b,23a], S. Todorova-Nova[133], S. Todt[50], M. Togawa[84], J. Tojo[89], S. Tokár[28a], K. Tokushuku[84], O. Toldaiev[68], R. Tombs[32], M. Tomoto[84,111], L. Tompkins[143,o], K.W. Topolnicki[86b], E. Torrence[123], H. Torres[102,ab], E. Torró Pastor[163], M. Toscani[30], C. Tosciri[39], M. Tost[11], D.R. Tovey[139], A. Traeet[16], I.S. Trandafir[27b], T. Trefzger[166], A. Tricoli[29], I.M. Trigger[156a], S. Trincaz-Duvoid[127], D.A. Trischuk[26], B. Trocmé[60], C. Troncon[71a], L. Truong[33c], M. Trzebinski[87], A. Trzupek[87], F. Tsai[145], M. Tsai[106], A. Tsiamis[152,e], P.V. Tsiareshka[37], S. Tsigaridas[156a], A. Tsirigotis[152,s], V. Tsiskaridze[155], E.G. Tskhadadze[149a], M. Tsopoulou[152,e], Y. Tsujikawa[88], I.I. Tsukerman[37], V. Tsulaia[17a], S. Tsuno[84], O. Tsur[150], K. Tsuri[118], D. Tsybychev[145], Y. Tu[64b], A. Tudorache[27b], V. Tudorache[27b], A.N. Tuna[36], S. Turchikhin[38], I. Turk Cakir[3a], R. Turra[71a], T. Turtuvshin[38,y], P.M. Tuts[41], S. Tzamarias[152,e], P. Tzanis[10], E. Tzovara[100], K. Uchida[153], F. Ukegawa[157], P.A. Ulloa Poblete[137c,137b], E.N. Umaka[29], G. Unal[36], M. Unal[11], A. Undrus[29], G. Unel[160], J. Urban[28b], P. Urquijo[105], G. Usai[8], R. Ushioda[154], M. Usman[108], Z. Uysal[21b], L. Vacavant[102], V. Vacek[132], B. Vachon[104], K.O.H. Vadla[125], T. Vafeiadis[36], A. Vaitkus[96], C. Valderanis[109], E. Valdes Santurio[47a,47b], M. Valente[156a], S. Valentinetti[23b,23a], A. Valero[163], E. Valiente Moreno[163], A. Vallier[102,ab], J.A. Valls Ferrer[163], D.R. Van Arneman[114], T.R. Van Daalen[138], A. Van Der Graaf[49], P. Van Gemmeren[6], M. Van Rijnbach[125,36], S. Van Stroud[96], I. Van Vulpen[114], M. Vanadia[76a,76b], W. Vandelli[36], M. Vandenbroucke[135], E.R. Vandewall[121], D. Vannicola[151], L. Vannoli[57b,57a], R. Vari[75a], E.W. Varnes[7], C. Varni[17a], T. Varol[148], D. Varouchas[66], L. Varriale[163], K.E. Varvell[147], M.E. Vasile[27b], L. Vaslin[40],

JHEP05(2024)131

G.A. Vasquez[165], F. Vazeille[40], T. Vazquez Schroeder[36], J. Veatch[31], V. Vecchio[101], M.J. Veen[103], I. Veliscek[126], L.M. Veloce[155], F. Veloso[130a,130c], S. Veneziano[75a], A. Ventura[70a,70b], A. Verbytskyi[110], M. Verducci[74a,74b], C. Vergis[24], M. Verissimo De Araujo[83b], W. Verkerke[114], J.C. Vermeulen[114], C. Vernieri[143], P.J. Verschuuren[95], M. Vessella[103], M.C. Vetterli[142,ag], A. Vgenopoulos[152,e], N. Viaux Maira[137f], T. Vickey[139], O.E. Vickey Boeriu[139], G.H.A. Viehhauser[126], L. Vigani[63b], M. Villa[23b,23a], M. Villaplana Perez[163], E.M. Villhauer[52], E. Vilucchi[53], M.G. Vincter[34], G.S. Virdee[20], A. Vishwakarma[52], A. Visibile[114], C. Vittori[36], I. Vivarelli[146], V. Vladimirov[167], E. Voevodina[110], F. Vogel[109], P. Vokac[132], J. Von Ahnen[48], E. Von Toerne[24], B. Vormwald[36], V. Vorobel[133], K. Vorobev[37], M. Vos[163], K. Voss[141], J.H. Vossebeld[92], M. Vozak[114], L. Vozdecky[94], N. Vranjes[15], M. Vranjes Milosavljevic[15], M. Vreeswijk[114], R. Vuillermet[36], O. Vujinovic[100], I. Vukotic[39], S. Wada[157], C. Wagner[103], J.M. Wagner[17a], W. Wagner[171], S. Wahdan[171], H. Wahlberg[90], R. Wakasa[157], M. Wakida[111], J. Walder[134], R. Walker[109], W. Walkowiak[141], A. Wall[128], T. Wamorkar[6], A.Z. Wang[170], C. Wang[100], C. Wang[62c], H. Wang[17a], J. Wang[64a], R.-J. Wang[100], R. Wang[61], R. Wang[6], S.M. Wang[148], S. Wang[62b], T. Wang[62a], W.T. Wang[80], W. Wang[14a], X. Wang[14c], X. Wang[162], X. Wang[62c], Y. Wang[62d], Y. Wang[14c], Z. Wang[106], Z. Wang[62d,51,62c], Z. Wang[106], A. Warburton[104], R.J. Ward[20], N. Warrack[59], A.T. Watson[20], H. Watson[59], M.F. Watson[20], E. Watton[59,134], G. Watts[138], B.M. Waugh[96], C. Weber[29], H.A. Weber[18], M.S. Weber[19], S.M. Weber[63a], C. Wei[62a], Y. Wei[126], A.R. Weidberg[126], E.J. Weik[117], J. Weingarten[49], M. Weirich[100], C. Weiser[54], C.J. Wells[48], T. Wenaus[29], B. Wendland[49], T. Wengler[36], N.S. Wenke[110], N. Wermes[24], M. Wessels[63a], K. Whalen[123], A.M. Wharton[91], A.S. White[61], A. White[8], M.J. White[1], D. Whiteson[160], L. Wickremasinghe[124], W. Wiedenmann[170], C. Wiel[50], M. Wielers[134], C. Wiglesworth[42], D.J. Wilbern[120], H.G. Wilkens[36], D.M. Williams[41], H.H. Williams[128], S. Williams[32], S. Willocq[103], B.J. Wilson[101], P.J. Windischhofer[39], F.I. Winkel[30], F. Winklmeier[123], B.T. Winter[54], J.K. Winter[101], M. Wittgen[143], M. Wobisch[97], Z. Wolffs[114], R. Wölker[126], J. Wollrath[160], M.W. Wolter[87], H. Wolters[130a,130c], A.F. Wongel[48], S.D. Worm[48], B.K. Wosiek[87], K.W. Woźniak[87], S. Wozniewski[55], K. Wraight[59], C. Wu[20], J. Wu[14a,14e], M. Wu[64a], M. Wu[113], S.L. Wu[170], X. Wu[56], Y. Wu[62a], Z. Wu[135], J. Wuerzinger[110], T.R. Wyatt[101], B.M. Wynne[52], S. Xella[42], L. Xia[14c], M. Xia[14b], J. Xiang[64c], X. Xiao[106], M. Xie[62a], X. Xie[62a], S. Xin[14a,14e], J. Xiong[17a], D. Xu[14a], H. Xu[62a], L. Xu[62a], R. Xu[128], T. Xu[106], Y. Xu[14b], Z. Xu[52], Z. Xu[14a], B. Yabsley[147], S. Yacoob[33a], N. Yamaguchi[89], Y. Yamaguchi[154], E. Yamashita[153], H. Yamauchi[157], T. Yamazaki[17a], Y. Yamazaki[85], J. Yan[62c], S. Yan[126], Z. Yan[25], H.J. Yang[62c,62d], H.T. Yang[62a], S. Yang[62a], T. Yang[64c], X. Yang[62a], X. Yang[14a], Y. Yang[44], Y. Yang[62a], Z. Yang[62a], W-M. Yao[17a], Y.C. Yap[48], H. Ye[14c], H. Ye[55], J. Ye[44], S. Ye[29], X. Ye[62a], Y. Yeh[96], I. Yeletskikh[38], B.K. Yeo[17a], M.R. Yexley[96], P. Yin[41], K. Yorita[168], S. Younas[27b], C.J.S. Young[54], C. Young[143], Y. Yu[62a], M. Yuan[106], R. Yuan[62b,k], L. Yue[96], M. Zaazoua[62a], B. Zabinski[87], E. Zaid[52], T. Zakareishvili[149b], N. Zakharchuk[34], S. Zambito[56], J.A. Zamora Saa[137d,137b], J. Zang[153], D. Zanzi[54], O. Zaplatilek[132], C. Zeitnitz[171], H. Zeng[14a], J.C. Zeng[162], D.T. Zenger Jr[26], O. Zenin[37], T. Ženiš[28a], S. Zenz[94], S. Zerradi[35a], D. Zerwas[66], M. Zhai[14a,14e],

JHEP05(2024)131

B. Zhang[14c], D.F. Zhang[139], J. Zhang[62b], J. Zhang[6], K. Zhang[14a,14e], L. Zhang[14c], P. Zhang[14a,14e], R. Zhang[170], S. Zhang[106], T. Zhang[153], X. Zhang[62c], X. Zhang[62b], Y. Zhang[62c,5], Y. Zhang[96], Z. Zhang[17a], Z. Zhang[66], H. Zhao[138], P. Zhao[51], T. Zhao[62b], Y. Zhao[136], Z. Zhao[62a], A. Zhemchugov[38], K. Zheng[162], X. Zheng[62a], Z. Zheng[143], D. Zhong[162], B. Zhou[106], H. Zhou[7], N. Zhou[62c], Y. Zhou[7], C.G. Zhu[62b], J. Zhu[106], Y. Zhu[62c], Y. Zhu[62a], X. Zhuang[14a], K. Zhukov[37], V. Zhulanov[37], N.I. Zimine[38], J. Zinsser[63b], M. Ziolkowski[141], L. Živković[15], A. Zoccoli[23b,23a], K. Zoch[56], T.G. Zorbas[139], O. Zormpa[46], W. Zou[41], L. Zwalinski[36]

[1] *Department of Physics, University of Adelaide, Adelaide; Australia*
[2] *Department of Physics, University of Alberta, Edmonton AB; Canada*
[3] [(a)] *Department of Physics, Ankara University, Ankara;* [(b)] *Division of Physics, TOBB University of Economics and Technology, Ankara; Türkiye*
[4] *LAPP, Université Savoie Mont Blanc, CNRS/IN2P3, Annecy; France*
[5] *APC, Université Paris Cité, CNRS/IN2P3, Paris; France*
[6] *High Energy Physics Division, Argonne National Laboratory, Argonne IL; United States of America*
[7] *Department of Physics, University of Arizona, Tucson AZ; United States of America*
[8] *Department of Physics, University of Texas at Arlington, Arlington TX; United States of America*
[9] *Physics Department, National and Kapodistrian University of Athens, Athens; Greece*
[10] *Physics Department, National Technical University of Athens, Zografou; Greece*
[11] *Department of Physics, University of Texas at Austin, Austin TX; United States of America*
[12] *Institute of Physics, Azerbaijan Academy of Sciences, Baku; Azerbaijan*
[13] *Institut de Física d'Altes Energies (IFAE), Barcelona Institute of Science and Technology, Barcelona; Spain*
[14] [(a)] *Institute of High Energy Physics, Chinese Academy of Sciences, Beijing;* [(b)] *Physics Department, Tsinghua University, Beijing;* [(c)] *Department of Physics, Nanjing University, Nanjing;* [(d)] *School of Science, Shenzhen Campus of Sun Yat-sen University;* [(e)] *University of Chinese Academy of Science (UCAS), Beijing; China*
[15] *Institute of Physics, University of Belgrade, Belgrade; Serbia*
[16] *Department for Physics and Technology, University of Bergen, Bergen; Norway*
[17] [(a)] *Physics Division, Lawrence Berkeley National Laboratory, Berkeley CA;* [(b)] *University of California, Berkeley CA; United States of America*
[18] *Institut für Physik, Humboldt Universität zu Berlin, Berlin; Germany*
[19] *Albert Einstein Center for Fundamental Physics and Laboratory for High Energy Physics, University of Bern, Bern; Switzerland*
[20] *School of Physics and Astronomy, University of Birmingham, Birmingham; United Kingdom*
[21] [(a)] *Department of Physics, Bogazici University, Istanbul;* [(b)] *Department of Physics Engineering, Gaziantep University, Gaziantep;* [(c)] *Department of Physics, Istanbul University, Istanbul; Türkiye*
[22] [(a)] *Facultad de Ciencias y Centro de Investigaciónes, Universidad Antonio Nariño, Bogotá;* [(b)] *Departamento de Física, Universidad Nacional de Colombia, Bogotá; Colombia*
[23] [(a)] *Dipartimento di Fisica e Astronomia A. Righi, Università di Bologna, Bologna;* [(b)] *INFN Sezione di Bologna; Italy*
[24] *Physikalisches Institut, Universität Bonn, Bonn; Germany*
[25] *Department of Physics, Boston University, Boston MA; United States of America*
[26] *Department of Physics, Brandeis University, Waltham MA; United States of America*
[27] [(a)] *Transilvania University of Brasov, Brasov;* [(b)] *Horia Hulubei National Institute of Physics and Nuclear Engineering, Bucharest;* [(c)] *Department of Physics, Alexandru Ioan Cuza University of Iasi, Iasi;* [(d)] *National Institute for Research and Development of Isotopic and Molecular Technologies, Physics Department, Cluj-Napoca;* [(e)] *National University of Science and Technology Politechnica, Bucharest;* [(f)] *West University in Timisoara, Timisoara;* [(g)] *Faculty of Physics, University of Bucharest, Bucharest; Romania*
[28] [(a)] *Faculty of Mathematics, Physics and Informatics, Comenius University, Bratislava;* [(b)] *Department of Subnuclear Physics, Institute of Experimental Physics of the Slovak Academy of Sciences, Kosice; Slovak Republic*

JHEP05(2024)131

[29] Physics Department, Brookhaven National Laboratory, Upton NY; United States of America
[30] Universidad de Buenos Aires, Facultad de Ciencias Exactas y Naturales, Departamento de Física, y CONICET, Instituto de Física de Buenos Aires (IFIBA), Buenos Aires; Argentina
[31] California State University, CA; United States of America
[32] Cavendish Laboratory, University of Cambridge, Cambridge; United Kingdom
[33] [(a)] Department of Physics, University of Cape Town, Cape Town;[(b)] iThemba Labs, Western Cape;[(c)] Department of Mechanical Engineering Science, University of Johannesburg, Johannesburg;[(d)] National Institute of Physics, University of the Philippines Diliman (Philippines);[(e)] University of South Africa, Department of Physics, Pretoria;[(f)] University of Zululand, KwaDlangezwa;[(g)] School of Physics, University of the Witwatersrand, Johannesburg; South Africa
[34] Department of Physics, Carleton University, Ottawa ON; Canada
[35] [(a)] Faculté des Sciences Ain Chock, Réseau Universitaire de Physique des Hautes Energies - Université Hassan II, Casablanca;[(b)] Faculté des Sciences, Université Ibn-Tofail, Kénitra;[(c)] Faculté des Sciences Semlalia, Université Cadi Ayyad, LPHEA-Marrakech;[(d)] LPMR, Faculté des Sciences, Université Mohamed Premier, Oujda;[(e)] Faculté des sciences, Université Mohammed V, Rabat;[(f)] Institute of Applied Physics, Mohammed VI Polytechnic University, Ben Guerir; Morocco
[36] CERN, Geneva; Switzerland
[37] Affiliated with an institute covered by a cooperation agreement with CERN
[38] Affiliated with an international laboratory covered by a cooperation agreement with CERN
[39] Enrico Fermi Institute, University of Chicago, Chicago IL; United States of America
[40] LPC, Université Clermont Auvergne, CNRS/IN2P3, Clermont-Ferrand; France
[41] Nevis Laboratory, Columbia University, Irvington NY; United States of America
[42] Niels Bohr Institute, University of Copenhagen, Copenhagen; Denmark
[43] [(a)] Dipartimento di Fisica, Università della Calabria, Rende;[(b)] INFN Gruppo Collegato di Cosenza, Laboratori Nazionali di Frascati; Italy
[44] Physics Department, Southern Methodist University, Dallas TX; United States of America
[45] Physics Department, University of Texas at Dallas, Richardson TX; United States of America
[46] National Centre for Scientific Research "Demokritos", Agia Paraskevi; Greece
[47] [(a)] Department of Physics, Stockholm University;[(b)] Oskar Klein Centre, Stockholm; Sweden
[48] Deutsches Elektronen-Synchrotron DESY, Hamburg and Zeuthen; Germany
[49] Fakultät Physik, Technische Universität Dortmund, Dortmund; Germany
[50] Institut für Kern- und Teilchenphysik, Technische Universität Dresden, Dresden; Germany
[51] Department of Physics, Duke University, Durham NC; United States of America
[52] SUPA - School of Physics and Astronomy, University of Edinburgh, Edinburgh; United Kingdom
[53] INFN e Laboratori Nazionali di Frascati, Frascati; Italy
[54] Physikalisches Institut, Albert-Ludwigs-Universität Freiburg, Freiburg; Germany
[55] II. Physikalisches Institut, Georg-August-Universität Göttingen, Göttingen; Germany
[56] Département de Physique Nucléaire et Corpusculaire, Université de Genève, Genève; Switzerland
[57] [(a)] Dipartimento di Fisica, Università di Genova, Genova;[(b)] INFN Sezione di Genova; Italy
[58] II. Physikalisches Institut, Justus-Liebig-Universität Giessen, Giessen; Germany
[59] SUPA - School of Physics and Astronomy, University of Glasgow, Glasgow; United Kingdom
[60] LPSC, Université Grenoble Alpes, CNRS/IN2P3, Grenoble INP, Grenoble; France
[61] Laboratory for Particle Physics and Cosmology, Harvard University, Cambridge MA; United States of America
[62] [(a)] Department of Modern Physics and State Key Laboratory of Particle Detection and Electronics, University of Science and Technology of China, Hefei;[(b)] Institute of Frontier and Interdisciplinary Science and Key Laboratory of Particle Physics and Particle Irradiation (MOE), Shandong University, Qingdao;[(c)] School of Physics and Astronomy, Shanghai Jiao Tong University, Key Laboratory for Particle Astrophysics and Cosmology (MOE), SKLPPC, Shanghai;[(d)] Tsung-Dao Lee Institute, Shanghai; China
[63] [(a)] Kirchhoff-Institut für Physik, Ruprecht-Karls-Universität Heidelberg, Heidelberg;[(b)] Physikalisches Institut, Ruprecht-Karls-Universität Heidelberg, Heidelberg; Germany
[64] [(a)] Department of Physics, Chinese University of Hong Kong, Shatin, N.T., Hong Kong;[(b)] Department of Physics, University of Hong Kong, Hong Kong;[(c)] Department of Physics and Institute for Advanced Study, Hong Kong University of Science and Technology, Clear Water Bay, Kowloon, Hong Kong; China

JHEP05(2024)131

[65] Department of Physics, National Tsing Hua University, Hsinchu; Taiwan
[66] IJCLab, Université Paris-Saclay, CNRS/IN2P3, 91405, Orsay; France
[67] Centro Nacional de Microelectrónica (IMB-CNM-CSIC), Barcelona; Spain
[68] Department of Physics, Indiana University, Bloomington IN; United States of America
[69] [(a)] INFN Gruppo Collegato di Udine, Sezione di Trieste, Udine; [(b)] ICTP, Trieste; [(c)] Dipartimento Politecnico di Ingegneria e Architettura, Università di Udine, Udine; Italy
[70] [(a)] INFN Sezione di Lecce; [(b)] Dipartimento di Matematica e Fisica, Università del Salento, Lecce; Italy
[71] [(a)] INFN Sezione di Milano; [(b)] Dipartimento di Fisica, Università di Milano, Milano; Italy
[72] [(a)] INFN Sezione di Napoli; [(b)] Dipartimento di Fisica, Università di Napoli, Napoli; Italy
[73] [(a)] INFN Sezione di Pavia; [(b)] Dipartimento di Fisica, Università di Pavia, Pavia; Italy
[74] [(a)] INFN Sezione di Pisa; [(b)] Dipartimento di Fisica E. Fermi, Università di Pisa, Pisa; Italy
[75] [(a)] INFN Sezione di Roma; [(b)] Dipartimento di Fisica, Sapienza Università di Roma, Roma; Italy
[76] [(a)] INFN Sezione di Roma Tor Vergata; [(b)] Dipartimento di Fisica, Università di Roma Tor Vergata, Roma; Italy
[77] [(a)] INFN Sezione di Roma Tre; [(b)] Dipartimento di Matematica e Fisica, Università Roma Tre, Roma; Italy
[78] [(a)] INFN-TIFPA; [(b)] Università degli Studi di Trento, Trento; Italy
[79] Universität Innsbruck, Department of Astro and Particle Physics, Innsbruck; Austria
[80] University of Iowa, Iowa City IA; United States of America
[81] Department of Physics and Astronomy, Iowa State University, Ames IA; United States of America
[82] Istinye University, Sariyer, Istanbul; Türkiye
[83] [(a)] Departamento de Engenharia Elétrica, Universidade Federal de Juiz de Fora (UFJF), Juiz de Fora; [(b)] Universidade Federal do Rio De Janeiro COPPE/EE/IF, Rio de Janeiro; [(c)] Instituto de Física, Universidade de São Paulo, São Paulo; [(d)] Rio de Janeiro State University, Rio de Janeiro; Brazil
[84] KEK, High Energy Accelerator Research Organization, Tsukuba; Japan
[85] Graduate School of Science, Kobe University, Kobe; Japan
[86] [(a)] AGH University of Krakow, Faculty of Physics and Applied Computer Science, Krakow; [(b)] Marian Smoluchowski Institute of Physics, Jagiellonian University, Krakow; Poland
[87] Institute of Nuclear Physics Polish Academy of Sciences, Krakow; Poland
[88] Faculty of Science, Kyoto University, Kyoto; Japan
[89] Research Center for Advanced Particle Physics and Department of Physics, Kyushu University, Fukuoka; Japan
[90] Instituto de Física La Plata, Universidad Nacional de La Plata and CONICET, La Plata; Argentina
[91] Physics Department, Lancaster University, Lancaster; United Kingdom
[92] Oliver Lodge Laboratory, University of Liverpool, Liverpool; United Kingdom
[93] Department of Experimental Particle Physics, Jožef Stefan Institute and Department of Physics, University of Ljubljana, Ljubljana; Slovenia
[94] School of Physics and Astronomy, Queen Mary University of London, London; United Kingdom
[95] Department of Physics, Royal Holloway University of London, Egham; United Kingdom
[96] Department of Physics and Astronomy, University College London, London; United Kingdom
[97] Louisiana Tech University, Ruston LA; United States of America
[98] Fysiska institutionen, Lunds universitet, Lund; Sweden
[99] Departamento de Física Teorica C-15 and CIAFF, Universidad Autónoma de Madrid, Madrid; Spain
[100] Institut für Physik, Universität Mainz, Mainz; Germany
[101] School of Physics and Astronomy, University of Manchester, Manchester; United Kingdom
[102] CPPM, Aix-Marseille Université, CNRS/IN2P3, Marseille; France
[103] Department of Physics, University of Massachusetts, Amherst MA; United States of America
[104] Department of Physics, McGill University, Montreal QC; Canada
[105] School of Physics, University of Melbourne, Victoria; Australia
[106] Department of Physics, University of Michigan, Ann Arbor MI; United States of America
[107] Department of Physics and Astronomy, Michigan State University, East Lansing MI; United States of America
[108] Group of Particle Physics, University of Montreal, Montreal QC; Canada
[109] Fakultät für Physik, Ludwig-Maximilians-Universität München, München; Germany

JHEP05(2024)131

[110] Max-Planck-Institut für Physik (Werner-Heisenberg-Institut), München; Germany
[111] Graduate School of Science and Kobayashi-Maskawa Institute, Nagoya University, Nagoya; Japan
[112] Department of Physics and Astronomy, University of New Mexico, Albuquerque NM; United States of America
[113] Institute for Mathematics, Astrophysics and Particle Physics, Radboud University/Nikhef, Nijmegen; Netherlands
[114] Nikhef National Institute for Subatomic Physics and University of Amsterdam, Amsterdam; Netherlands
[115] Department of Physics, Northern Illinois University, DeKalb IL; United States of America
[116] [(a)] New York University Abu Dhabi, Abu Dhabi;[(b)] University of Sharjah, Sharjah; United Arab Emirates
[117] Department of Physics, New York University, New York NY; United States of America
[118] Ochanomizu University, Otsuka, Bunkyo-ku, Tokyo; Japan
[119] Ohio State University, Columbus OH; United States of America
[120] Homer L. Dodge Department of Physics and Astronomy, University of Oklahoma, Norman OK; United States of America
[121] Department of Physics, Oklahoma State University, Stillwater OK; United States of America
[122] Palacký University, Joint Laboratory of Optics, Olomouc; Czech Republic
[123] Institute for Fundamental Science, University of Oregon, Eugene, OR; United States of America
[124] Graduate School of Science, Osaka University, Osaka; Japan
[125] Department of Physics, University of Oslo, Oslo; Norway
[126] Department of Physics, Oxford University, Oxford; United Kingdom
[127] LPNHE, Sorbonne Université, Université Paris Cité, CNRS/IN2P3, Paris; France
[128] Department of Physics, University of Pennsylvania, Philadelphia PA; United States of America
[129] Department of Physics and Astronomy, University of Pittsburgh, Pittsburgh PA; United States of America
[130] [(a)] Laboratório de Instrumentação e Física Experimental de Partículas - LIP, Lisboa;[(b)] Departamento de Física, Faculdade de Ciências, Universidade de Lisboa, Lisboa;[(c)] Departamento de Física, Universidade de Coimbra, Coimbra;[(d)] Centro de Física Nuclear da Universidade de Lisboa, Lisboa;[(e)] Departamento de Física, Universidade do Minho, Braga;[(f)] Departamento de Física Teórica y del Cosmos, Universidad de Granada, Granada (Spain);[(g)] Departamento de Física, Instituto Superior Técnico, Universidade de Lisboa, Lisboa; Portugal
[131] Institute of Physics of the Czech Academy of Sciences, Prague; Czech Republic
[132] Czech Technical University in Prague, Prague; Czech Republic
[133] Charles University, Faculty of Mathematics and Physics, Prague; Czech Republic
[134] Particle Physics Department, Rutherford Appleton Laboratory, Didcot; United Kingdom
[135] IRFU, CEA, Université Paris-Saclay, Gif-sur-Yvette; France
[136] Santa Cruz Institute for Particle Physics, University of California Santa Cruz, Santa Cruz CA; United States of America
[137] [(a)] Departamento de Física, Pontificia Universidad Católica de Chile, Santiago;[(b)] Millennium Institute for Subatomic physics at high energy frontier (SAPHIR), Santiago;[(c)] Instituto de Investigación Multidisciplinario en Ciencia y Tecnología, y Departamento de Física, Universidad de La Serena;[(d)] Universidad Andres Bello, Department of Physics, Santiago;[(e)] Instituto de Alta Investigación, Universidad de Tarapacá, Arica;[(f)] Departamento de Física, Universidad Técnica Federico Santa María, Valparaíso; Chile
[138] Department of Physics, University of Washington, Seattle WA; United States of America
[139] Department of Physics and Astronomy, University of Sheffield, Sheffield; United Kingdom
[140] Department of Physics, Shinshu University, Nagano; Japan
[141] Department Physik, Universität Siegen, Siegen; Germany
[142] Department of Physics, Simon Fraser University, Burnaby BC; Canada
[143] SLAC National Accelerator Laboratory, Stanford CA; United States of America
[144] Department of Physics, Royal Institute of Technology, Stockholm; Sweden
[145] Departments of Physics and Astronomy, Stony Brook University, Stony Brook NY; United States of America
[146] Department of Physics and Astronomy, University of Sussex, Brighton; United Kingdom
[147] School of Physics, University of Sydney, Sydney; Australia

JHEP05(2024)131

[148] Institute of Physics, Academia Sinica, Taipei; Taiwan
[149] [(a)] E. Andronikashvili Institute of Physics, Iv. Javakhishvili Tbilisi State University, Tbilisi;[(b)] High Energy Physics Institute, Tbilisi State University, Tbilisi;[(c)] University of Georgia, Tbilisi; Georgia
[150] Department of Physics, Technion, Israel Institute of Technology, Haifa; Israel
[151] Raymond and Beverly Sackler School of Physics and Astronomy, Tel Aviv University, Tel Aviv; Israel
[152] Department of Physics, Aristotle University of Thessaloniki, Thessaloniki; Greece
[153] International Center for Elementary Particle Physics and Department of Physics, University of Tokyo, Tokyo; Japan
[154] Department of Physics, Tokyo Institute of Technology, Tokyo; Japan
[155] Department of Physics, University of Toronto, Toronto ON; Canada
[156] [(a)] TRIUMF, Vancouver BC;[(b)] Department of Physics and Astronomy, York University, Toronto ON; Canada
[157] Division of Physics and Tomonaga Center for the History of the Universe, Faculty of Pure and Applied Sciences, University of Tsukuba, Tsukuba; Japan
[158] Department of Physics and Astronomy, Tufts University, Medford MA; United States of America
[159] United Arab Emirates University, Al Ain; United Arab Emirates
[160] Department of Physics and Astronomy, University of California Irvine, Irvine CA; United States of America
[161] Department of Physics and Astronomy, University of Uppsala, Uppsala; Sweden
[162] Department of Physics, University of Illinois, Urbana IL; United States of America
[163] Instituto de Física Corpuscular (IFIC), Centro Mixto Universidad de Valencia - CSIC, Valencia; Spain
[164] Department of Physics, University of British Columbia, Vancouver BC; Canada
[165] Department of Physics and Astronomy, University of Victoria, Victoria BC; Canada
[166] Fakultät für Physik und Astronomie, Julius-Maximilians-Universität Würzburg, Würzburg; Germany
[167] Department of Physics, University of Warwick, Coventry; United Kingdom
[168] Waseda University, Tokyo; Japan
[169] Department of Particle Physics and Astrophysics, Weizmann Institute of Science, Rehovot; Israel
[170] Department of Physics, University of Wisconsin, Madison WI; United States of America
[171] Fakultät für Mathematik und Naturwissenschaften, Fachgruppe Physik, Bergische Universität Wuppertal, Wuppertal; Germany
[172] Department of Physics, Yale University, New Haven CT; United States of America

[a] Also Affiliated with an institute covered by a cooperation agreement with CERN
[b] Also at Physics Department, An-Najah National University, Nablus, Palestine
[c] Also at Borough of Manhattan Community College, City University of New York, New York NY; United States of America
[d] Also at Center for High Energy Physics, Peking University; China
[e] Also at Center for Interdisciplinary Research and Innovation (CIRI-AUTH), Thessaloniki; Greece
[f] Also at Centro Studi e Ricerche Enrico Fermi; Italy
[g] Also at CERN, Geneva; Switzerland
[h] Also at Département de Physique Nucléaire et Corpusculaire, Université de Genève, Genève; Switzerland
[i] Also at Departament de Fisica de la Universitat Autonoma de Barcelona, Barcelona; Spain
[j] Also at Department of Financial and Management Engineering, University of the Aegean, Chios; Greece
[k] Also at Department of Physics and Astronomy, Michigan State University, East Lansing MI; United States of America
[l] Also at Department of Physics, Ben Gurion University of the Negev, Beer Sheva; Israel
[m] Also at Department of Physics, California State University, Sacramento; United States of America
[n] Also at Department of Physics, King's College London, London; United Kingdom
[o] Also at Department of Physics, Stanford University, Stanford CA; United States of America
[p] Also at Department of Physics, University of Fribourg, Fribourg; Switzerland
[q] Also at Department of Physics, University of Thessaly; Greece
[r] Also at Department of Physics, Westmont College, Santa Barbara; United States of America
[s] Also at Hellenic Open University, Patras; Greece
[t] Also at Institucio Catalana de Recerca i Estudis Avancats, ICREA, Barcelona; Spain

JHEP05(2024)131

[u] Also at Institut für Experimentalphysik, Universität Hamburg, Hamburg; Germany
[v] Also at Institute for Nuclear Research and Nuclear Energy (INRNE) of the Bulgarian Academy of Sciences, Sofia; Bulgaria
[w] Also at Institute of Applied Physics, Mohammed VI Polytechnic University, Ben Guerir; Morocco
[x] Also at Institute of Particle Physics (IPP); Canada
[y] Also at Institute of Physics and Technology, Mongolian Academy of Sciences, Ulaanbaatar; Mongolia
[z] Also at Institute of Physics, Azerbaijan Academy of Sciences, Baku; Azerbaijan
[aa] Also at Institute of Theoretical Physics, Ilia State University, Tbilisi; Georgia
[ab] Also at L2IT, Université de Toulouse, CNRS/IN2P3, UPS, Toulouse; France
[ac] Also at Lawrence Livermore National Laboratory, Livermore; United States of America
[ad] Also at National Institute of Physics, University of the Philippines Diliman (Philippines); Philippines
[ae] Also at Technical University of Munich, Munich; Germany
[af] Also at The Collaborative Innovation Center of Quantum Matter (CICQM), Beijing; China
[ag] Also at TRIUMF, Vancouver BC; Canada
[ah] Also at Università di Napoli Parthenope, Napoli; Italy
[ai] Also at University of Colorado Boulder, Department of Physics, Colorado; United States of America
[aj] Also at Washington College, Chestertown, MD; United States of America
[ak] Also at Yeditepe University, Physics Department, Istanbul; Türkiye
[*] Deceased

JHEP05(2024)131